Université du Québec

Institut National de la Recherche Scientifique

Centre Énergie Matériaux Télécommunications

A Broadband Direct-Demodulator Based on Nolen Matrix for 5G Wireless Communication Systems

Par

Esam Abdusalam Shafah

Mémoire présentée pour l'obtention du grade de

Maître ès sciences (M.Sc.)

En Télécommunications

Jury d'évaluation

Président du jury et examinateur interne	Professeur Tayeb A. Denidni INRS-EMT
Examinateur externe	Professeur Halim Boutayeb Huawei Technologies Canada Co., Ltd.
Directeur de recherche	Professeur Tarek Djerafi INRS-EMT

Abstract

The development of low cost, low power receiver (low power signal demodulation) is indispensable for the next generation of wireless communication, which is defined as a green communication system. The multiport reflectometer is a measurement device that mainly used in high-frequency bands. This technique allows the measurement of the amplitude ratio and the phase difference of two electromagnetic waves. Besides, it can be used as a direct demodulator. The framework of the conventional six-port is not adapted to millimeter-wave applications. In fact, the input and output ports arrangement are not suitable for the integrated system where both inputs and output are not separated.

A new multi-port reflectometer based on Nolen matrix with a centre frequency of 28 GHz is proposed and analyzed. The Input and output ports are rearranged separately. The two inputs represent the local oscillator (LO) and the radio frequency (RF) signals, where RF and LO signals are fed to the inputs (port 6 and port 1), respectively. In addition, I and Q signals are retrieved after the detection stage at the four output ports (ports 2 - 5). The obtained structure represents the aimed arrangement in terms of suitability of use when inputs and outputs are separated each in one side, and good performance is fulfilled.

The designed 2x4 Nolen matrix consists of five hybrid couplers (two 3dB, two 4.7 dB, and one 6 dB) and the proposed double T-shape phase shifter. The circuit is simulated and fabricated to validate the introduced scheme. Advanced Design System (ADS) software is used to design the different components. Both processes, the simulation and the fabrication, have shown a good agreement in terms of retrieving the original signal and implying the aimed arrangement. The obtained results of isolation are better than 20 dB for the frequency range from 26 GHz to 30.4 GHz. Good power equality is achieved of less than 1.5 dB around 7.5 dB of supplemental insertion loss and phase unbalance of ± 8 degree.

The proposed circuit is low cost, small size simple structure with good performance and suitable configuration arrangement with separate inputs and outputs. This study has been made to show that the proposed multi-port based on Nolen matrix can be more adequate for the next generation millimeter wave communications compared to the conventional millimeter wave receivers.

Keywords: Advanced Design System (ADS), Multi-port receiver, local oscillator (LO), radio frequency (RF), and Nolen matrix.

DEDICATION

Praise be to Allah and prayer and peace be upon the Messenger of Allah. Then, I dedicate this work to my mother, may Allah prolong her life in his obedience and my father may Allah have mercy on him. Since this is a little of what I have been given. I also pay tribute to my wife who sacrificed and still sacrificing for me. I thank my dear sons and daughters for their inspiration. Thanks to my siblings for their continued support.

ACKNOWLEDGEMENT

In the name of Allah, I thank Allah for his mercy, which made my able to go through this challenge up to the end.

I would like to express my gratitude to my research supervisor Prof. Tarek Djerafi for his unlimited support, guidance, and continuous advice during my research activities. In addition, I would like to thank the jury members for their time and efforts in reviewing my thesis and providing me valuable comments. Thanks to all my colleagues at INRS-EMT whom have helped me directly or indirectly in the completion of my thesis. In additional to all INRS staff.

TABLE OF CONTENTS

LIST OF TABLES

TABLE OF FIGURES

LIST OF ABBREVIATIONS

ADS	Advanced design System
AR	Augmented Reality
BER	Bit Error Rate
BFN	Beamforming Network
DC	Direct current
FCC	Federal Communications Commission
FDD	Frequency Division Duplex
FFT	Fast Fourier Transform
FSS	Fixed - Satellite Service
IF	Intermediate Frequency
IoT	Internet of Things
ISED	Innovation Science and Economic Development Canada
LE	Licence-Exempt
LTE	Long-Term Evolution
LNA	Low-Noise Amplifier
LO	Local Oscillator
MIMO	Multiple Input Multiple Output
mm Wave	Millimetre Wave
NR	New Radio Access
QPSK	Quadrature Phase Shift Keying

RF	Radio Frequency
TDD	Time Division Duplex
UMFUS	Upper Microwave Flexible Use Service
WB	Wide Bandwidth
5G	Fifth-Generation

CHAPTER ONE: INTRODUCTION

This chapter introduces the fifth-generation (5G) in terms of the conception, and the associated operation frequencies. Furthermore, an overview of the receiving system architecture and the millimeter wave (mm Wave) demodulator is given. Moreover, the main two types of the reception system (heterodyne, and homodyne) are described. However, for introducing the main topic for this work "A Broadband Direct Demodulator Based on Nolen Matrix for 5G Communication System", the theory of multi-port demodulator is explained and discussed.

1.1 5G Technology

The main upcoming advancement in mobile telecommunication standards is defined as the 5G technology [1][2][3]. Table 1.1 summarizes the main specifications about the current 4G and the

Table 1.1 table of the current and next technology (5G)

	Current generation	Next generation 5G
Technology	Multi-standard network Cat-M1/NB-IoT Cloud-optimized functions VNF orchestration	Gigabit LTE (TDD, FDD, LAA) Massive MIMO Network slicing Dynamic service orchestration Predictive analytics
Enhanced Mobile Broadband	Screens everywhere	New tools
Automotive	On-demand Information	Real-time information vehicle to vehicle
Manufacturing	Process automation	Flow management and remote supervision
Energy and utilities	Metering and smart grid	Resource management and automation

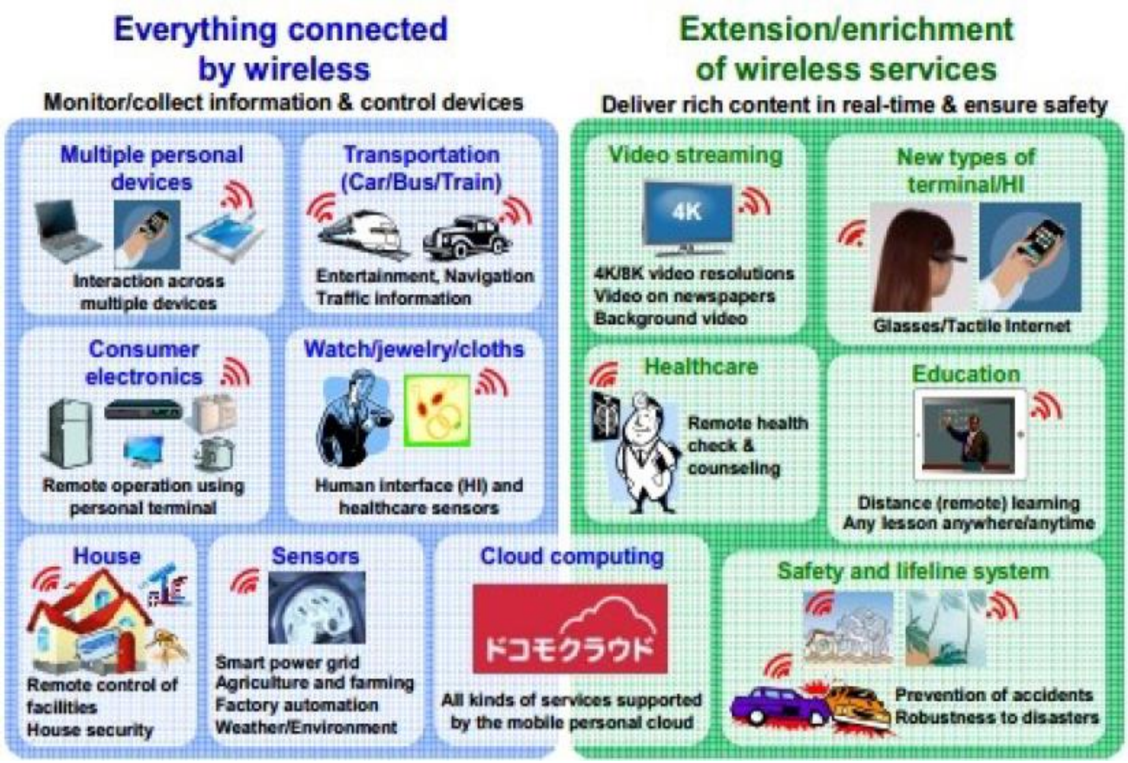

Figure 1.1 5G service trends [7].

next generation. The 5G technology is expected to offer super-broadband mobile services that featured with low latency and low power operation [3]. Dynamic orchestration of service with network slicing and management of energy and resource represent the key point of the 5G. The massive MIMO is expected to be among 5G foundational components due to its ability to serve multiple devices and maintaining fast data rates and consistent performance [4]. The car industry will also be transformed by 5G technology. The accomplishment of network slicing will enhance self-driving vehicles, the safety, and the efficiency in the transportation sector.

Because of the massive growth in the use of the Internet, 5G technology demands more effectively and flexibility use of mm Wave spectrum. The 5G as new technology promises to consumers, the offer of advanced products and applications such as mobile systems, sensing equipment, video transmission, vehicle-radar applications, short range high capacity wireless communication devices for the delivery of multimedia applications [5] [6].

Figure 1.1 shows clearly that 5G is not only a shift from the fourth generation (4G) to the fifth generation (5G). In addition, it gives an idea about the increased demand in terms of what is already under the use such as smart houses, smart transportation, etc. and the expected extension of wireless services like healthcare. Massive use of sensor and sensor network combined with localization system and decisional algorithms will allow the implementation of these services. Another example is distance education. The whole world is going to be connected; this is the promise and one of the challenges that is facing the 5G technology.

1.2 5G spectrum availability

In Canada, according to the consultation released in June 2017 by Innovation Science and Economic Development Canada (ISED), the high demand on the wireless connection is acquiring a new frequency spectrum, services, and technologies. This consultation is aiming to release a millimeter wave (mm Wave) spectrum in the 28 GHz, 37-40 GHz, and 64-71 GHz frequency bands.

In global scale, other countries are looking to develop and adapt to 5G requirements promptly. Especially, in terms of providing higher frequencies. United States (U.S.) established a new rule to facilitate the innovations in terms of supporting the development of 5G wireless networks according to the Federal Communications Commission (FCC) [5][6]. The U.S. has new rules that give the flexibility to use 28 GHz bandwidth (27.5-28.35 GHz), 37 GHz bandwidth (37-38.6 GHz) and 38 GHz bandwidth (38.6-40 GHz); and the frequency band 64-71 GHz as unlicensed frequencies. The “International Telecommunication Union” (ITU) is studying a range of eleven frequency bands between 24.25 and 86 GHz. These frequencies are expected to be required by broadband mobile services in the future. ITU is not focusing on studying 28 GHz in particular. Furthermore, Japan, and South Korea are concerning to pursue authorizing mobile operations in this frequency band locally. Presently, In Canada, ISED is continuing to allow the innovators from testing the equipment for "a short-term access" [3].

1.2.1 28 GHz frequency band (27.5-28.35 GHz)

For implementing fixed-satellite service (FSS) and fixed services on 27.5-28.35 GHz frequency band, the applications are sharing the spectrum from 3 GHz to 30 GHz with respect to the soft partitioning concept; this partition allows certain services to enter the spectrum by considering that one service could be prioritized on the others, as is shown by Figure 1.2 [5].

Figure 1.2 Canadian frequency allocations in the 28 GHz band [5].

The next Figure shows frequency blocks representing the division of existing Canadian band plan. This division cover the frequency division duplex (FDD) point-to-point systems.

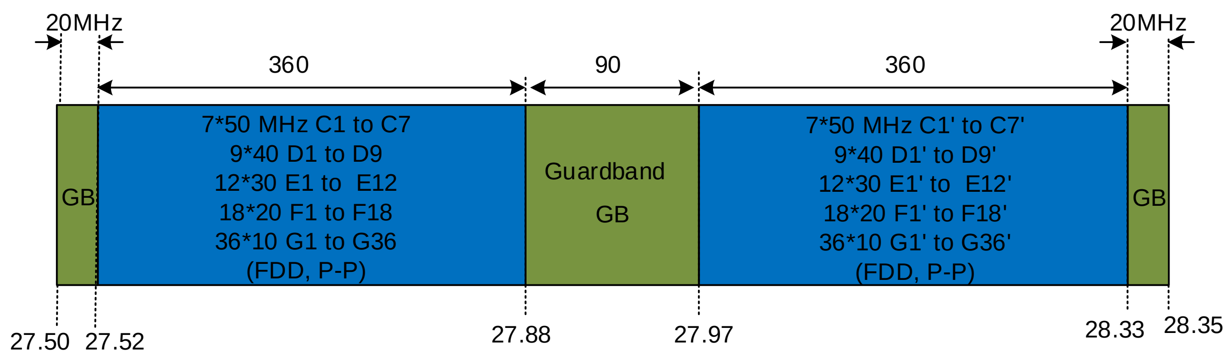

Figure 1.3 Current Canadian band plan in the frequency band 27.5-28.35 GHz [5].

Figure 1.4 shows the band plan proposed by ISED that can be aligned to FCC band plan. In fact, as FCC, this band plan consists of two unpaired 425 MHz blocks (2 x 425 MHz) [5].

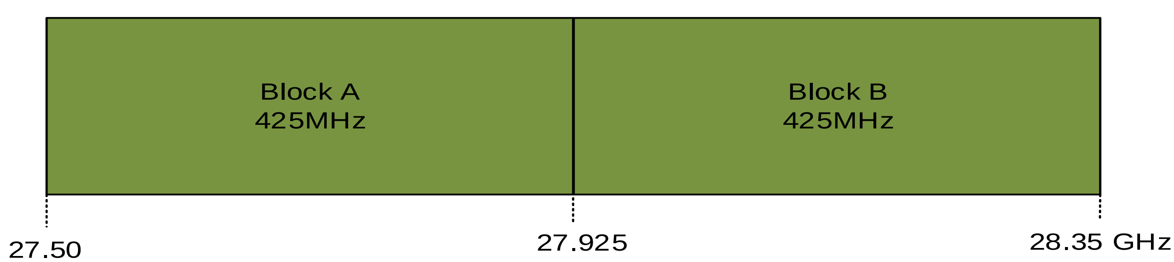

Figure 1.4 Proposed new Canadian band plan in the 28 GHz band [5].

1.2.2 Frequency band 37-40 GHz

Even if there are no allocated FSS services in this band, there is an interest for commercial use due to the probable congestion in Ku and Ka bands.

According to ISED the division of fixed and mobile services within 37-40 GHz frequency band is as a co-prime basis:

- 37.5 - 40.0 GHz band for fixed-satellite service
- 37 - 38 GHz band for space research service
- 39.5 - 40 GHz band for mobile-satellite service
- Earth exploration-satellite service

The 37.5 - 40 GHz band for earth exploration-satellite service is allocated on a secondary basis. Figure 1.5 demonstrates the seven regions used by the fixed services of 37 - 40 GHz frequency band.

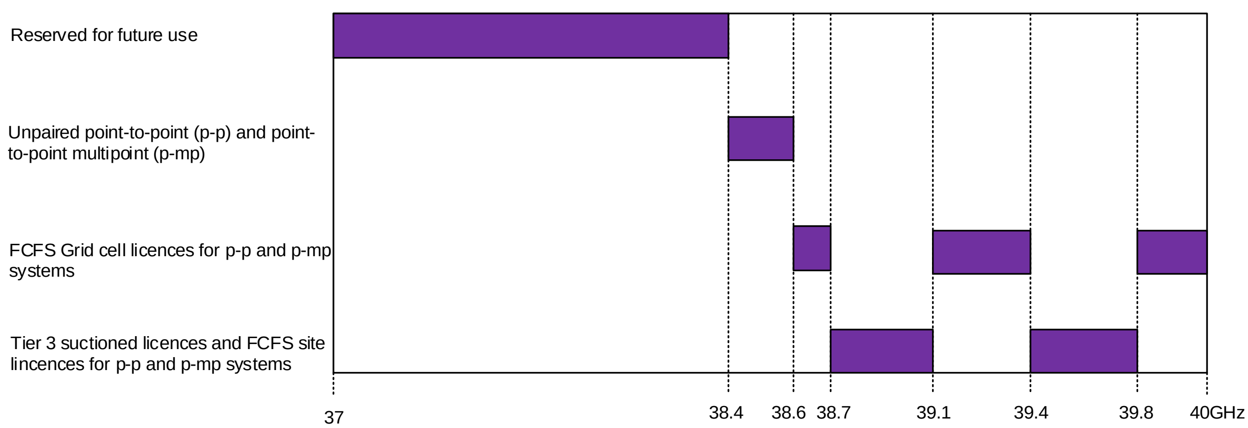

Figure 1.5 Current use of the frequency band 37-40 GHz by fixed service [5].

Figure 1.6 shows the band plan for frequency band 37-40 GHz proposed by ISED to cooperate with U.S. side in terms of fixed and mobile services along the Canada-U.S. border.

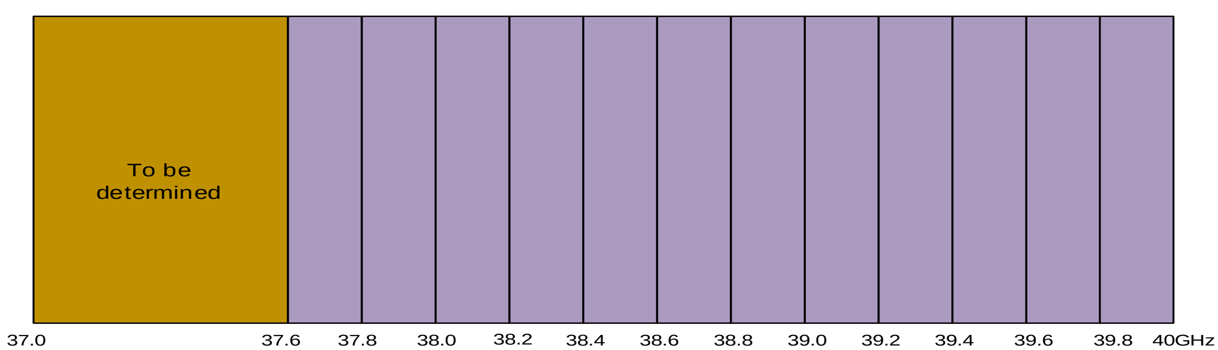

Figure 1.6 Proposed Canadian 37-40 GHz frequency band plan [5].

1.2.3 Frequency band 64-71 GHz for license-exempt use

The Licence-Exempt (LE) being used by communication carrier networks to improve the spectrum suffered from congestion by relying on Wi-Fi networks when data off-loading been enabled. In these band frequencies, ISED recognizes the high demand for license-exempt (LE) for a range of applications.

The 64-65 GHz frequency band in Canada Table of Frequency Allocations (CTFA) is allocated to three-frequency clusters co-primary basis:

- fixed
- mobile (exclude aircraft mobile)
- inter-satellite services

The frequency band 64 - 66 GHz assigned by CTFA for high-density applications in the fixed service. Figure 1.7 illustrates the Canadian frequency allocations in the band 64–71 GHz.

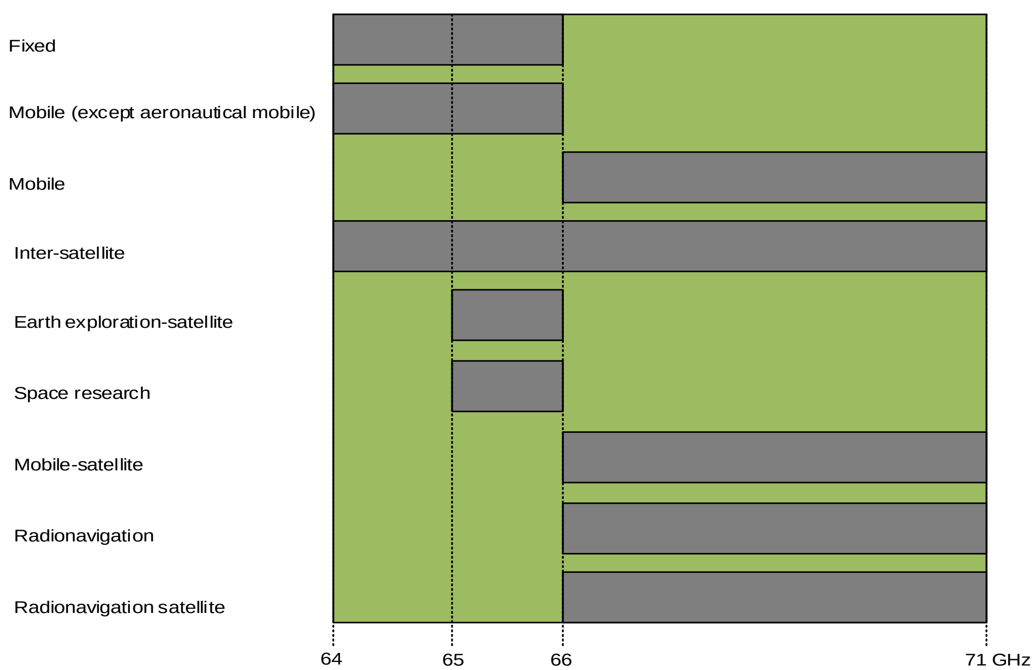

Figure 1.7 Canadian frequency allocations in the band 64–71 GHz [5].

Figure 1.8 presents the radio access vision up to 2020. This vision introducing the Long-Term Evolution (LTE) and New Radio Access (NR) Technologies for 1 GHz to 100 GHz band [8].

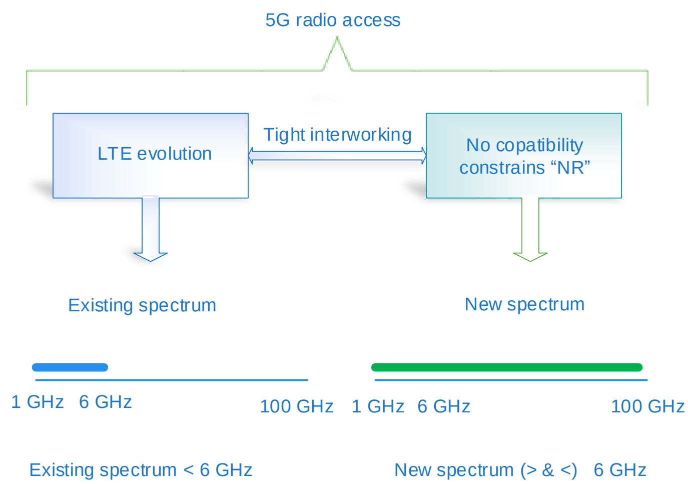

Figure 1.8 Radio Access Vision for 2020 and past: 5G Radio Access contains a New Radio Access Technology (NR) and LTE Evolution that is not in reverse good with LTE and is operable from sub-1 GHz to 100 GHz [8].

1.3 Architectures of reception systems

Figure 1.9 illustrates the most commonly used architecture at the reception level. Usually, the signal that the antenna detects does not contain only the information, it is often associated with noise and other unnecessary signals. Hence, a low-noise amplifier (LNA) and a band pass filter at the input of the receiver are used to reduce the noise level [9] [10]. After isolating the signal, it brought back to the same frequency allowing its treatment using a demodulator as shown in Figure 1.9. All the receivers are built around the same essential elements with different degree of complexity [10].

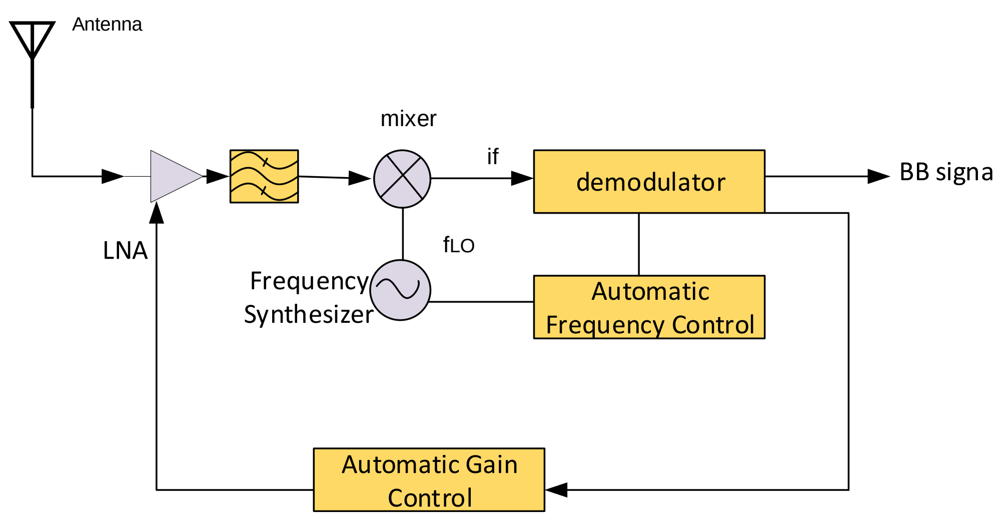

Figure 1.9 Architectures of reception systems [10].

The received signal is demodulated, processed and transmitted to the destination. There are two main categories of receivers. The first type is homodynes receiver whose passes from the RF frequencies towards the low frequencies directly. The second type is the heterodyne receiver whose passes from the RF frequencies towards the lower frequencies in several stages.

1.3.1 Homodyne receivers (direct conversion or ZERO-IF)

The architecture of homodyne receivers is illustrated in Figure 1.10. The received RF signal is transposed directly into the baseband. The local oscillator (LO) signal is used to perform the transposition. The LO signal must be identical to the central frequency of the RF carrier signal, which will cancel the intermediate frequency IF. Then, the image signal is superimposed on the RF signal [9] [10].

The major disadvantage of this architecture is the presence of a DC offset voltage at the output of the mixers caused mainly by insulation faults at the mixer between the RF and LO channels. Moreover, the degradation of the sensitivity of the receiver to very low-frequency signals, because of the high level of noise that expressed in 1/f and non-thermal that will be superimposed on the wanted signal [10].

Despite these negative points, this type of receiver is increasingly popular because of the simplicity of RF processing which is associated with a much-improved level of integration compared to heterodyne receivers.

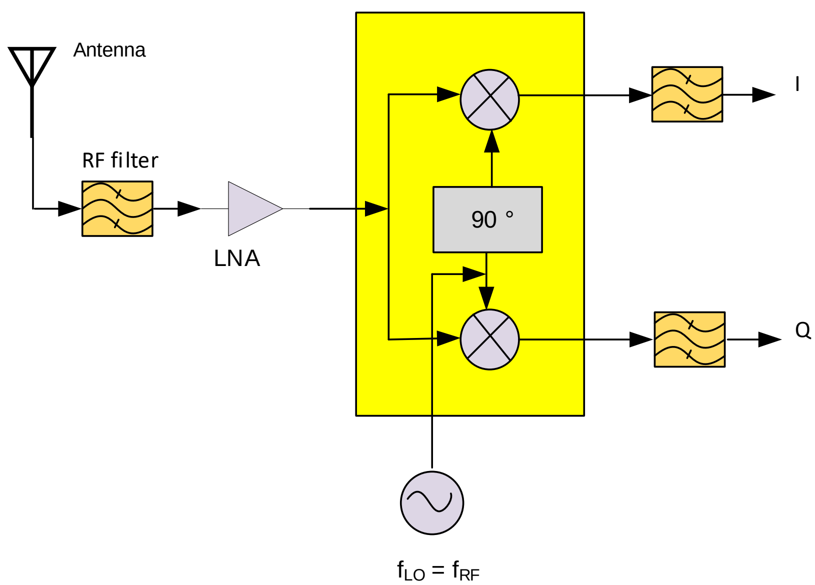

Figure 1.10 Architectures of homodyne receivers [10].

1.3.2 Heterodyne receivers

This architecture consists of antenna, RF filter, low-noise amplifier, mixer, and the local isolator as shown in Figure 1.11. The principle work of the heterodyne receiver can be described as following, the transposition happening to the received RF signal around a fixed IF frequency. If this transposition is done in one-step, the receiver is called heterodyne. However, if it requires several steps, the receiver is called super heterodyne.

In the case of a super heterodyne structure, a first transposition of the spectrum can be achieved by multiplying the RF signal with the signal from a local oscillator f_{LO1}. The second transposition is performed by an I/Q demodulator consisting of a pair of mixers mounted in quadrature with a local oscillator f_{LO2}. Because of its remarkable performance in terms of selectivity, this architecture is the most used in second and third generation mobiles.

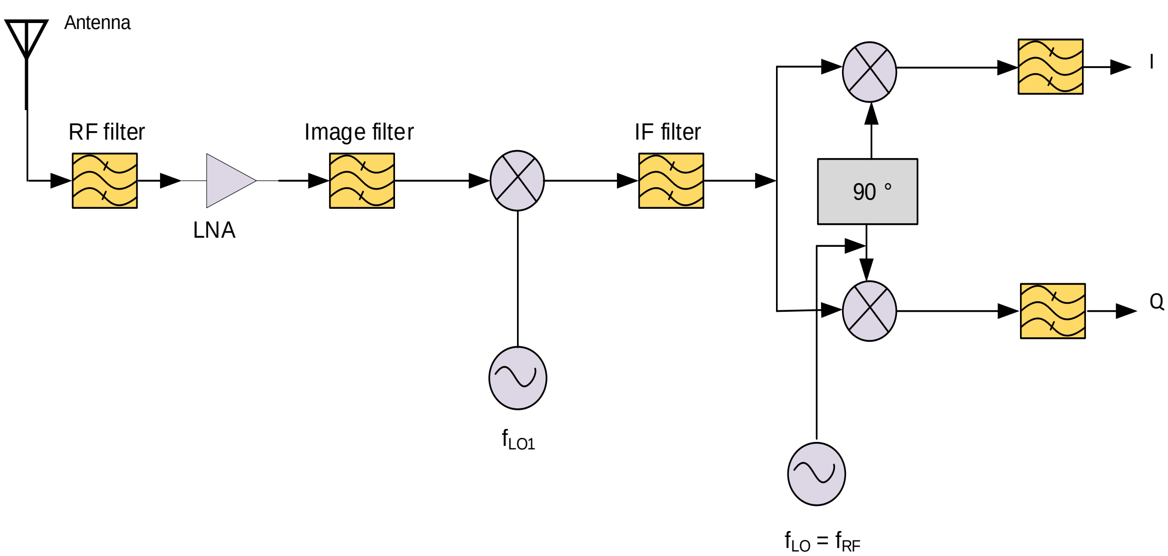

Figure 1.11 Architectures of heterodyne receivers [10].

The major disadvantage of this receiver is related to the problem of image frequency rejection due to the several attempts have been made to integrate this structure. However, the RF and IF filters are difficult to integrate, which makes this architecture very cumbersome in terms of complexity. Effectively, the realization of these filters requires the integration of inductances to reach important quality factors, which is practically difficult, because of the quality factors that we can obtain are insufficient to ensure a good selectivity of the receiver [10].

1.3.3 Direct receiver (Demodulator)

The present of using the six-port to determine the phase of a high-frequency signal was early as 1964 [11]. The date of creation of the six-port as a measurement technique was reported in [12], and [13]. Although the authors have published partial ideas and used the term previously, these publications offer complete theoretical information as well as the approach for designing and optimize the six-port. The studies have continued to give more ideas that were fundamental as of the nineties of the last century [14]. Nowadays, researchers are more attracted to improve the multi-port performance due to the demands of the next generation technology. Besides, it has multiple usages as an analyzer [15] [16].

The general structure of the six-port shown in Figure 1.12 consists mainly of two inputs and four outputs. Each two of the four outputs are connected to a power detector. More details about six-port structure can be found in [9] [15] [16]. A set of characteristic equations can be used to find out the four unknowns. The six-port has a passive circuit comprised of couplers that are connected through transmission lines and phase shifters to produce linear signal outputs, combinations of phase shifted input signals, at I and Q the terminals. The six-port can be used as

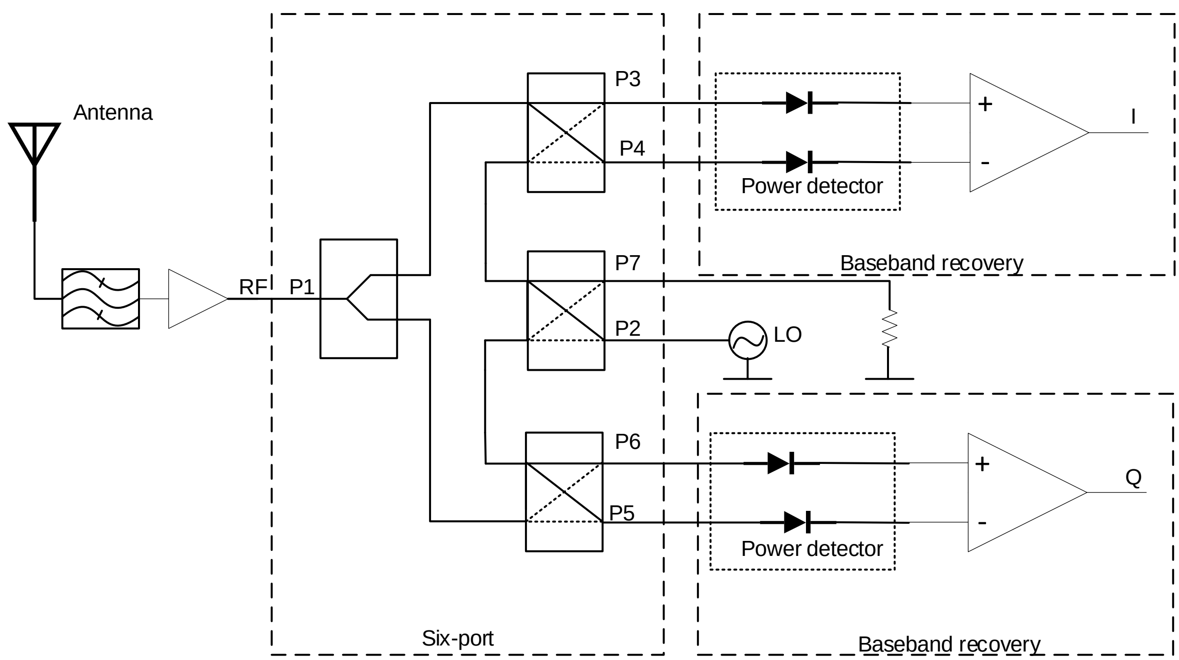

Figure1.12 Block diagram of Six-Port Demodulator [9].

a reflectometer to measure only the reflection coefficient and as network analyzer to measure the transmission and reflection coefficients [10] [16]. The six-port junction was used successfully in the design of network analyzers [9], down-conversion, direct modulation, and more [10] [16].

The multi-port demodulator can be considered as homodyne type due to the direct conversion characterization. The block diagram of the multi-port demodulator shown in Figure 1.12. This multi-port demodulator described by three main blocks: six-port, power detection, and baseband recovery.

Multi-port correlator

At this step, a Local oscillator (LO) signal is combined with the modulated RF signal. As it shown by the six-port block diagram Figure 1.2, a shifted phase occurs between the combined signals RF (after the modulation) and LO in the six-port correlator. This phase shift depends on the S-parameters of the six-port correlator [9].

Power detection

In most cases, a Schottky diode power detector can be used for Power detection. The nonlinear characteristic of the Schottky diode is in a range of frequencies. In the Ideal power detector, a square law transfer function described in the equation below is used to model the power detector current as a function of the voltage [9].

$$I_{PD}(v) = kv^2$$

where *k* is a constant. (1.1)

Baseband Retrieving

Each output of the two diodes is connected to a differential baseband amplifier. In the amplifier stage, the output of each amplifier will be the difference between its inputs. Eventually, I / Q signals are retrieved in the last step.

Theory of Multi-Port Demodulator

The mathematical representation of demodulation as given in next formulas:

$$Z = A_{RF} (X_I + j X_Q) e^{j\omega t} \quad (1.2)$$

$$g = A_{LO} e^{j\varphi} e^{j\omega t} \quad (1.3)$$

where,

Z and g are the modulated RF and LO signals respectively.

ω: is the angular frequency.

φ: is the relative phase between RF and LO.

A_{LO}: LO amplitude.

A_{RF}: RF amplitude.

X_I and X_Q: are the transmitted baseband I and Q data.

RF and LO are combined as:

$$y = S_{x2g} + S_{x1z} \tag{1.4}$$

Where x coincides to one of the four output ports P1 – P4, x э {1, 2, 3, 4}. S_{nm} is the S-parameter transmitted from port m to port n of the multi-port correlator [9]. Since, a1 = z is the RF wave on port P6 and a2 = g on port P5. An ideal power detector modulation with a square law transfer function considered as:

$$Y_x = R\{y_x\} = \frac{y_x + \overline{y_x}}{2} \tag{1.5}$$

The above formula used to calculate real part (time-domain) signal. Then, by squaring the result the real part (time-domain) output voltage V_x is as shown next:

$$V_x = LPF\{kY_x^2\} = k\frac{y_x\,\overline{y_x}}{2} = k\,\frac{|y_x|^2}{2} \tag{1.6}$$

Solving (1.2) and (1.6) by using Euler's formula where (k=1) V_x becomes:

$$V_x = |S_{x2}|^2 A_{LO}^2/2 + |S_{x1}|^2 A_{RF}^2 \left(X_I^2 + X_Q^2\right)/2 + \tag{1.7}$$

$$A_{LO}\,A_{RF}\,|S_x|\,X_I\,\cos(\phi + \angle S_i) +$$

$$A_{LO}\,A_{RF}\,|S_x|\,X_Q\,\sin(\phi + \angle S_i)$$

where,
$$|S_x| = |S_{x1}||S_{x2}| \tag{1.8}$$

$$\angle S_x = \angle S_{x2} - \angle S_{x1} \tag{1.9}$$

From (1.7), the presence of X_I and X_Q in the output signal V_x is a different phase ϕ of RF and LO as well as how the phase and the gain are correlating in the multi-port.

Introducing the multi-port matrix model:

$$S = \frac{1}{2}\begin{bmatrix} 0 & 0 & -1 & j & -1 & j \\ 0 & 0 & 1 & j & j & -1 \\ -1 & 1 & 0 & 0 & 0 & 0 \\ j & j & 0 & 0 & 0 & 0 \\ -1 & j & 0 & 0 & 0 & 0 \\ j & -1 & 0 & 0 & 0 & 0 \end{bmatrix} \qquad (1.10)$$

The following formula is the mathematical representation of the detection of Q (Q_d), and I (I_d) signals - For the derivation of these equations refer to [9] - as:

$$I_d = \frac{2}{A_{LO}\, A_{RF}} (V_4 - V_3) \qquad (1.11)$$

$$Q_d = \frac{2}{A_{LO}\, A_{RF}} (V_6 - V_5)$$

In the ideal case of detection, the received I_d and Q_d signal should be same as the transmitted I and Q signal ($I_d = k\, X_I$ and $Q_d = k\, X_Q$) since k is a scaling factor. In the real case of the multi-port correlator there might be a phase and/or amplitude imbalance, thus, unwanted transfer between the two channels (I and Q).

The differences between the multi-port receiver and the conventional receiver could be concluded in terms of advantages and disadvantages. The multi-port receiver has higher bandwidth and higher data rate. Also, higher linearity and low loss because of its passive circuit. Moreover, it has lower power detection and better correlation due to its distributed circuit. On the other hand, it has low sensitivity and the limitation in the dynamic range due to the use of the diode detectors. Second is the size concern, this because of the multi-port correlator is a distributed circuit [9].

1.4 Millimeter wave demodulator

Nowadays, studies and measurements demonstrate that 5G mm Wave could be a significant member of 5G technology [5] [6]. However, in the past mm Wave bands mostly used for cell phone services because of the concerning short-range and non-line of sight coverage matters.

The advanced technology is promising to solve the preventions of using mm Wave bands for mobile. The short transmission paths and high propagation losses can be improved by the reuse of the spectrum in microcellular propagation and by the reduction in interference between the close cells. Besides, the tiny antennas -because of mm Waves signals- for concentrating signals with a significant gain can compensate for propagation losses. Moreover, the characteristic of the short wavelength for mm Wave gives a possibility to build up what so called multi-element

Table 1.2 Performance comparison of heterodyne, homodyne and multiport techniques (with reference to diode-based receiver architectures)

Performance Indicator/Parameter	Heterodyne Scheme	Homodyne Scheme	Multiport Scheme
Dynamic range	Excellent	Good	Average
LO requirement (power and frequency-stability)	Average	High	Low
Signal sensitivity	Excellent	Good	Good
Harmonic control	Difficult	Average	Easy
IP3	Average	Good	Excellent
Port-to-port isolation	Difficult-to-achieve	Average	Easy-to-achieve
Conversion loss	Good	Good	Excellent
Noise figure	Excellent	Good	Average
Structure complexity	High	Low	Average
Wideband/multiband flexibility*	Average	Good	Excellent

*This is a special design consideration for certain special applications such as software-defined radio, UWB etc. [11].

dynamic beam-forming antennas. These will be a small enough in size to install into handsets where cannot be done in the wavelength frequencies less than 6 GHz which is nowadays the operation frequencies for phones [6]. Also, mm Wave frequency bands are useful in areas that require such capacity by supporting very high capacity networks. In addition, the use for the backhaul and the machine-to-machine communication. Meanwhile, the 5G technology latency promising to allow variation of the Internet of Things (IoT) applications such as fitness and healthcare devices, autonomous driving cars, wearables, home, and office automation, etc. [6]. Table 1.2 is showing the performance Indicator/Parameter for different types of mm Wave receivers as well as a comparison between them.

Although heterodyne receiver can reach the 100 dB of dynamic range, it requires a mixer for bring the RF and IF modulated signals together. Homodyne receiver is using quadrature down-conversion resulting in obtaining the maximum information from modulated I/Q signal. However, the multi-port is limited in this term because of the limit of the quadrature region of the used diodes.

The LO used in the Homodyne and heterodyne receivers should satisfy some requirement in term of power (5 to 10 dB). At mm Wave, it is complicated to add an amplifier to reach the required power. The multi-port does not require high LO power, which the advantage here thus reduces the consumption of the DC at the level of the receiver. Hence, this can be one way to solve the DC problem.

1.5 Proposed work

In most cases, the multiport demodulator offers low complexity and low-cost measurements [12] [13] [14]. However, from the block diagram Figure 1.12, the two inputs are located into both sides of the multiport. Nevertheless, the proposed arrangement of the multi-port aiming to arrange the inputs in one side and the outputs in one side separately with considering the size reduction.

The Beamforming Networks as Butler and Nolen have been presented and discussed in many of works recently and before more details can be found in [15] [16]. Considering them as a useful tool and suitable configuration to have the required arrangement where the input ports are on one side and the output port on the other side. Moreover, the amplitude and phase arrangement should be modified to follow the rules that defined by the six-port.

Momentum technology development has a significant impact on mm Wave bands and 5G technology services. Some providers decided to make a forward step by making strategy and started tackling the challenges to develop 5G services. As this work, focus on the design of mm Wave demodulator based on Nolen Matrix for the 5G Application.

Frequency selection

The academic researchers have more interest in the 28 GHz band where ensuring to apply the high data-rate applications, with suitable bandwidth, in this band [6]. However, In Canada ISED allowed equipment experiments by innovators to study the new services such as sensing equipment, video transmission utilizing non-conventional frequencies, and mobile systems within mm Wave spectrum bands. Moreover, ISED will continue to allow flexible studies at 28 GHz band; however, it will remain to support an ongoing development for 5G technology [5]. Noticeably, the 5G technology has an interest in different frequencies. Hence, this work is concerning mm Wave band around the 28 GHz frequency.

CHAPTER TWO: Design of Nolen Matrix

2.1 Multi-port beamforming

Beamforming network (BFN) is playing the main role in building intelligent antenna systems. In BFN, *N* antenna elements connected to *M* beam ports to form the multiple beams. Conventional beam orientation can be achieved by adjusting only the phase signals of the different elements. A phase distribution should be accomplished to direct the beam in the desired direction. BFNs are ingenious devices comprising circuits formed of directional couplers and phase shifters. By connecting a BFN to the antenna array and RF switches, a set of beams can be realized by exciting one or more ports simultaneously by RF signals. A signal presented at an input port will produce equal excitations at all ports with a gradual phase shift between them, resulting in a beam that radiates in a specific direction of space. A signal at another input port will form a beam in another direction [23]. Several beamforming techniques can provide fixed beams: matrices as Butler, Blass, and Nolen and lenses as Rotman or Luneberg. The Butler matrix is the most widely used because of its ease of design [24].

The BFN, for example, is one of the key components in multiple input multiple output (MIMO) system. MIMO technique is one of the most attractive candidates for increasing spectrum efficiency since it significantly increases the throughput and reliability without additional bandwidth when applied to the radio frequency path.

2.2 BFN matrices

In this section, we are going to review BFN matrices to explain the work principle of each.

2.2.1 Butler matrix

The most cited matrix for the formation of a beam supply network is probably the Butler matrix. A reciprocal and symmetrical passive circuit with *N* input ports and *N* output ports drives where *N* radiating elements producing *N* different beams. Figure 2.1 shows a diagram of a 4x4 Butler matrix.

The standard form of the matrix when *N* must be an integer power of 2 ($N = 2^n$ where n is a positive integer). For forming the conventional network, couplers (3 dB, 90°) with 0 dB couplers (which can be realized by the combination of two 3 dB couplers) are used. The non-binary form is recognized using a combination of prime numbers of ports: 3x3, 5x5, 7x7, and so on. Note, for non-binary structures that the couplers are no longer limited to hybrids (3 dB, 90°). The formation

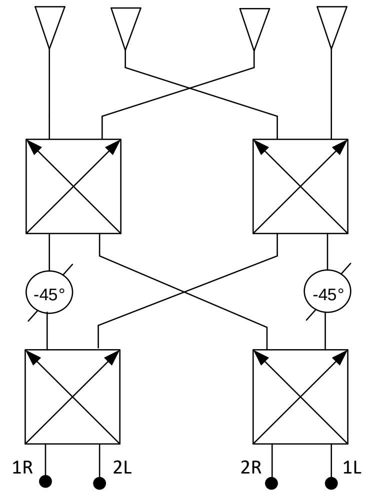

Figure 2.1 A standard topology of N X N Butler matrix.

of multiple beams is possible, with some limitations. Two adjacent beams cannot be formed simultaneously because they add up and produce a single beam. Moreover, Butler matrix is considered the most interesting option because of its ability to form orthogonal lobes and the simplicity of its design. Compared with its counterparts Blass and Nolen, the Butler matrix requires fewer couplers (for a 4x4 matrix as shown in Figure 2.1, four couplers are needed for the Butler matrix, 6 couplers for Nolen and 16 for Blass). The Butler matrix is a parallel system, unlike the Blass matrix (serial system).

The design of large matrices is quite easy since the phase shifters can be placed symmetrically with respect to the phase line and subsequently the diagram of Butler matrix is identical to that of an FFT (Fast Fourier Transform). Where Butler matrix consists of three basic elements:

H: hybrid couplers or junctions:

$$\mathrm{H} = \frac{\mathrm{N}}{2}\log(\mathrm{N}) \tag{2.1}$$

P: fixed phase shifters generally delay lines:

$$\mathrm{P} = \frac{\mathrm{N}}{2}\left(\log(\mathrm{N}) - 1\right) \tag{2.2}$$

C: crossing:

$$\mathrm{C} = \sum_{\mathrm{k}-}^{\log_2(\mathrm{N})}\left[\frac{\mathrm{N}}{2}\left(2^{\mathrm{k}-1} - 1\right)\right] \tag{2.3}$$

For a large matrix (many crossings, for example, 16 crossings are necessary for an 8x8 matrix, for a matrix with 32 ports, one will need 416 crossings). This could introduce higher levels of transmission loss [23].

2.2.2 Blass matrix

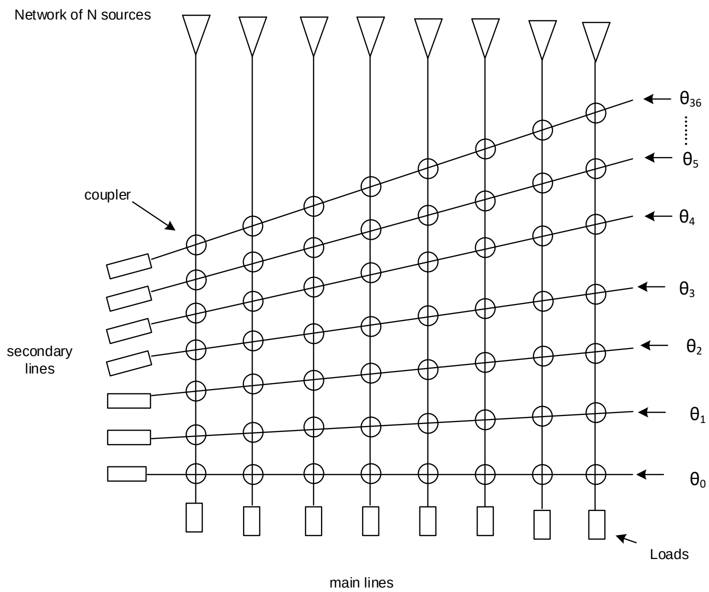

Figure 2.2 Topology of Bless matrix.

The Blass matrix is a serial power network with a lattice structure like that shown in Figure 2.2 [25] [26]. The matrix has several transverse lines (through lines) that carry the energy and several branch lines that intersect the first and lead to the network. Couplers are placed at each crossing so that a fraction of the energy incident on the main line directed at a second line in a definite direction. The other end of the second line provided with an absorbent charge. Between two directional couplers, a phase shifter or line-length adjuster generates the phase change required to create the phase gradient between each output port. The coupling coefficients of the different couplers and the phase shift values of the different constant or variable phase shifters are calculated to obtain the diagrams of desired energy that are different depending on whether power is coming in or being taken by one or the other of the main lines.

The Blass matrix widely used despite it is expensive and complicated because of the particular directional couplers that must be provided at each crossing. The Blass matrix can be designed regarding use with any number of elements. However, there are significant losses because of the loads at the terminals [23].

2.2.3 Nolen Matrix

Nolen matrix can be considered as a special case of the Blass matrix where *N* antennas are coupled to *M* beam ports. Thus, Nolen matrix can feed a number of antennas different from the number of beam orientations. This matrix consists of two types of components (coupler and phase shifter) and does not show any crossover [23]. Each node in the matrix consists of a directional coupler of parameter θ_{ij} and a phase shifter of parameter φ_{ij}. Mosca algorithm used to calculate these parameters from *N* and *M* and the direction of the beams [27]. Figure 2.3 shows 2 x *N* Nolen matrix, the coupler/phase shifter with specific θ_{ij}, φij placed in two rows with specific arraignment between the two inputs and the four outputs to assure the multi-port theory of working.

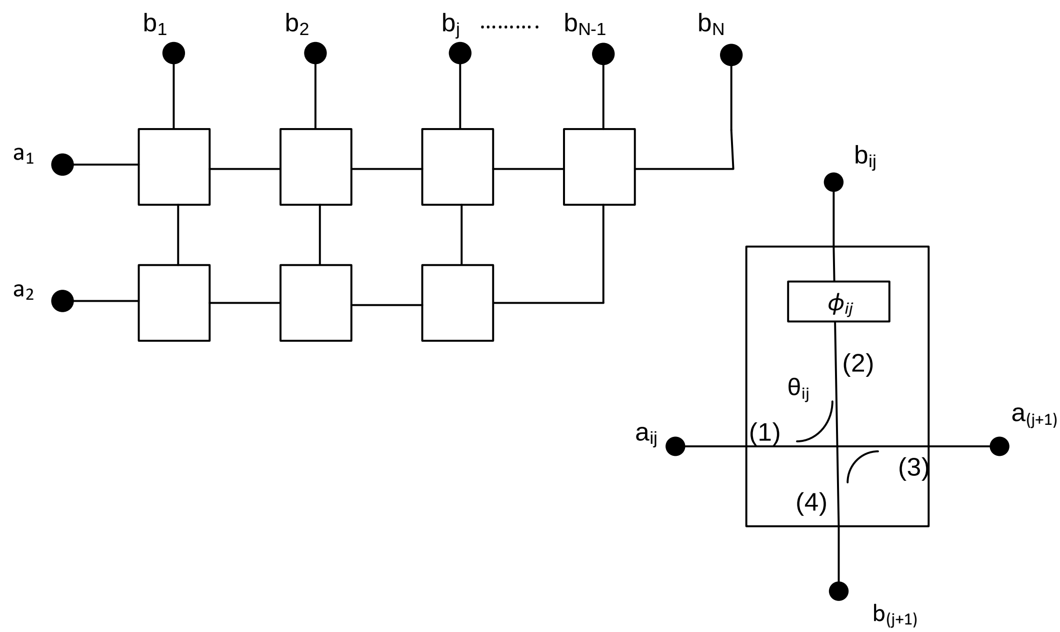

Figure 2.3 The general form of the Nolen matrix. [16]

2.3 Nolen matrix as demodulator

Nolen matrix is more adapted to build a structure like six-port with two inputs and four outputs matrix. Unlike Butler matrix, which gives 4 x 4 (since two ports are unusable at this case) and Blass matrix, which require, load with less efficiency because of the losses at the loads as it described previously in Blass matrix section. Moreover, the advantage of no crossover exist in this technique unlike to Blass matrix technique.

2.3.1 Six port demodulator

The demodulation chain was implemented by Agilent's ADS software. Figure 2.4 provides an overall scheme diagram done by ADS software simulation of direct conversion six-port using the ideal components.

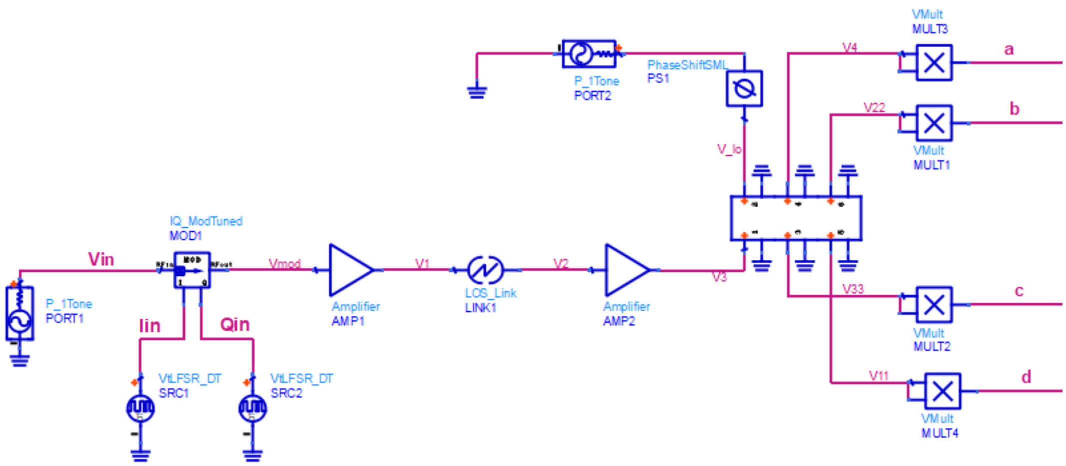

Figure 2.4 A diagram showing the ADS simulation of the multi-port direct conversion with ideal six-port.

The modulated input signal QPSK passes into a block containing the multi-port dispersions S-parameter behavior. At the multi-port outputs, power detectors are placed using ideal components. I/Q information of the QPSK demodulated with differential amplifiers for baseband recovery (see Figure 2.5). This subtraction assembly makes it possible to perform the subtraction of the signals in addition to minimize the undesired DC component.

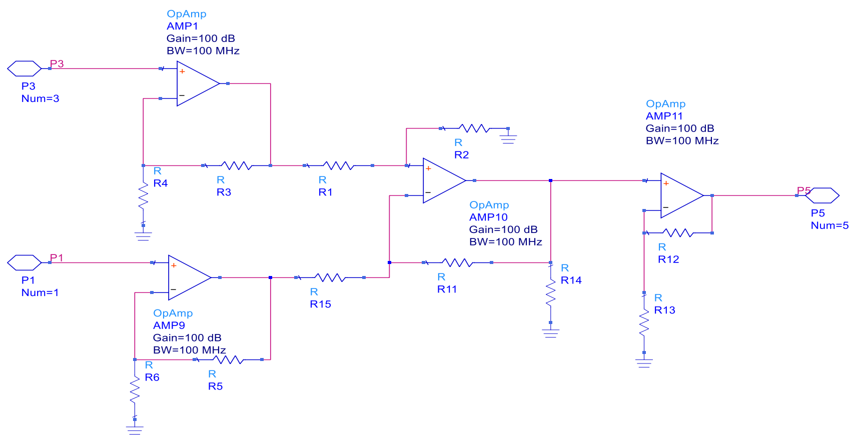

Figure 2.5 Subtraction and amplification circuit using operational amplifiers.

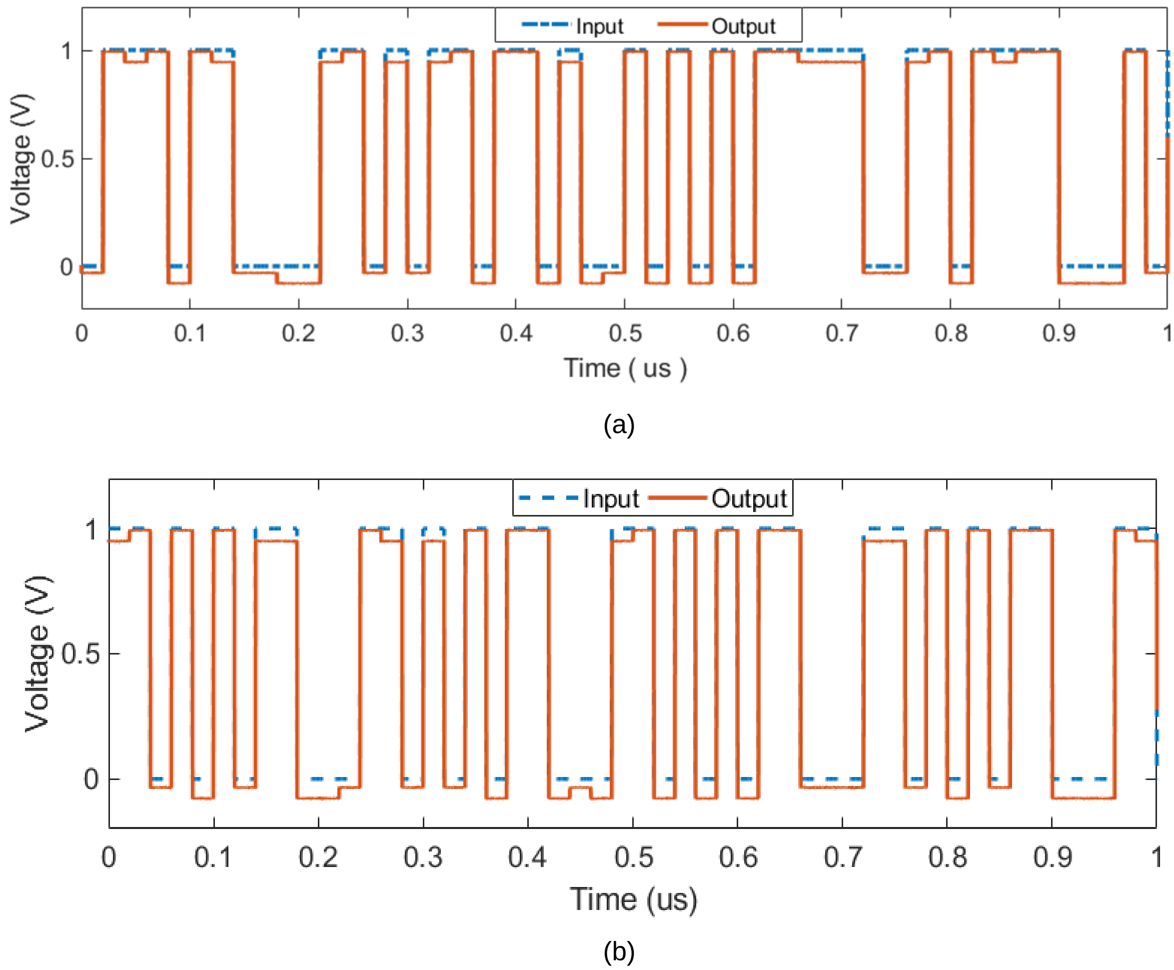

Figure 2.6 Input and output signals (a) I_{input}/I_{output} in volt vs. time and (b) Q_{input}/Q_{output} in volt vs. time.

Figure 2.6 shows the input and output signals in the range of 0 to 1 μs. From the same figure, it is clear that the output signals I_{out} / Q_{out} are containing the same information of the input signals I_{in} / Q_{in} respectively. It is noticeable that the multi-port brings little distortion in the recovered signals. A slight variation in voltage amplitude can be noticed.

Figure 2.7 illustrates the spectrum of the QPSK modulated input signal. It is noticeable that the width of the spectrum which corresponds to a signal of 100 Mb/s. The Figure 2.8 shows, in addition to the LO input signal, the spectrum of output signals Iout/Qout where both are having the same width of the spectrum which corresponds to a signal of 100 Mb / s.

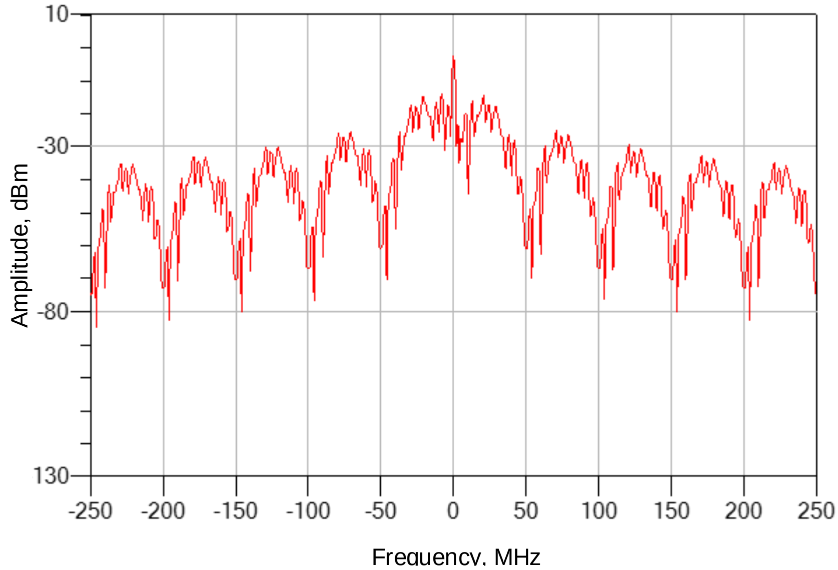

Figure 2.7 Spectrum of the input QPSK modulated signal.

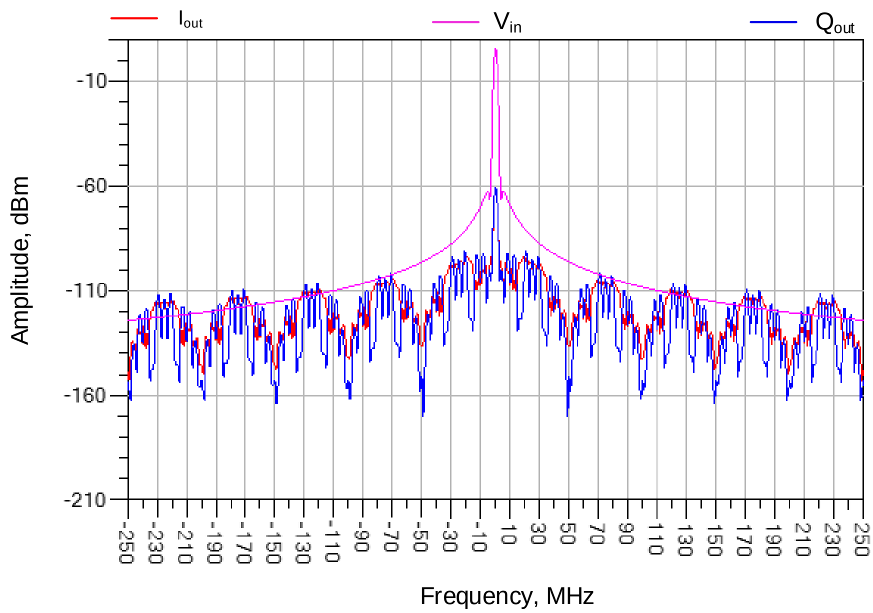

Figure 2.8 Spectrum of the QPSK demodulated signals (I_{out} and Q_{out}) at the output and the input LO signal (V_{in}).

2.4 Design of Nolen matrix (using ideal components)

The theoretical parameters of the directional couplers and phase shifters associated to the Nolen matrix obtained for the matrix described above are reported in Table 2.1. These values indicate that three different directional couplers and different phase shifters are necessary to build the equivalent six-port Nolen matrix.

Table 2.1 Parameters of the Nolen 2X4 Matrix Retained (θ_{ij} and ϕ_{ij}) [23]

	1	2	3	4
1	0.500 0^0	0.500 0^0	0.707 0^0	1.000 0^0
2	0.577 0^0	0.500 180^0	1.000 0^0	

Building the receiver system, starting from building the Nolen matrix system using ADS software. Nolen matrix built up with ideal components as shown in Figure 2.9. The coupler within

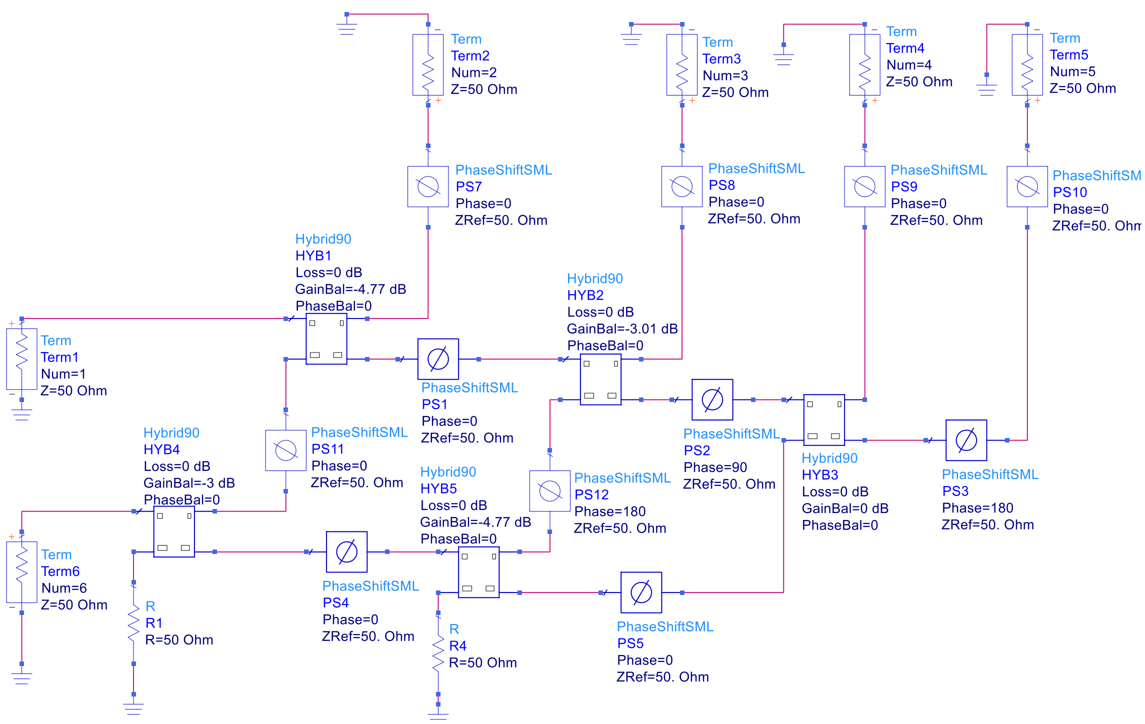

Figure 2.9 Building Nolen matrix using on ADS (ideal case).

gain balance (showing as “GainBal” in Figure 2.9) of 0 dB corresponds to the 3 dB one, the coupler within gain balance of 3.01 dB corresponds to the 4.7 dB one, and the coupler within gain balance of 4.77 dB corresponds to the 6 dB one. Figure 2.10 evaluates the results of Nolen matrix (using ideal components) and illustrates the simulated relative phase differences between adjacent output ports for port1 and adjacent output ports for port6. The input ports are defined as port 1 and 6 to conserve the same nomination used for the six-port as well as in equation 1.10

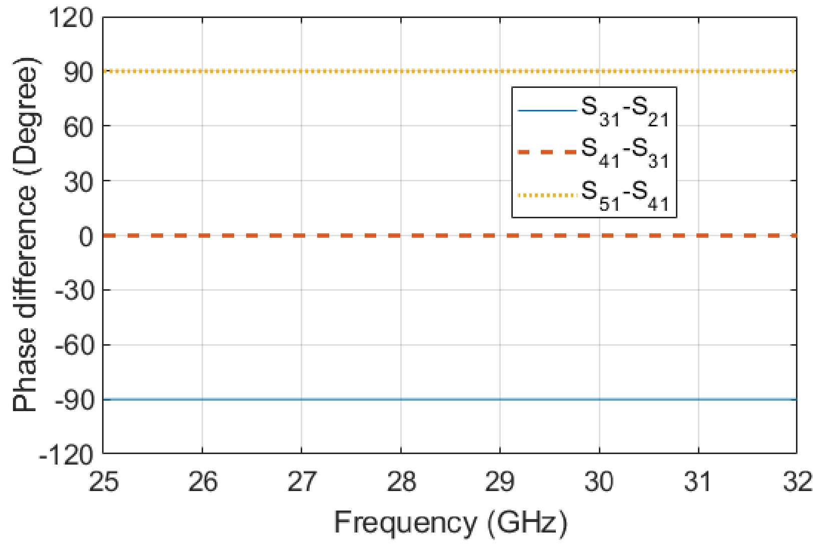

(a)

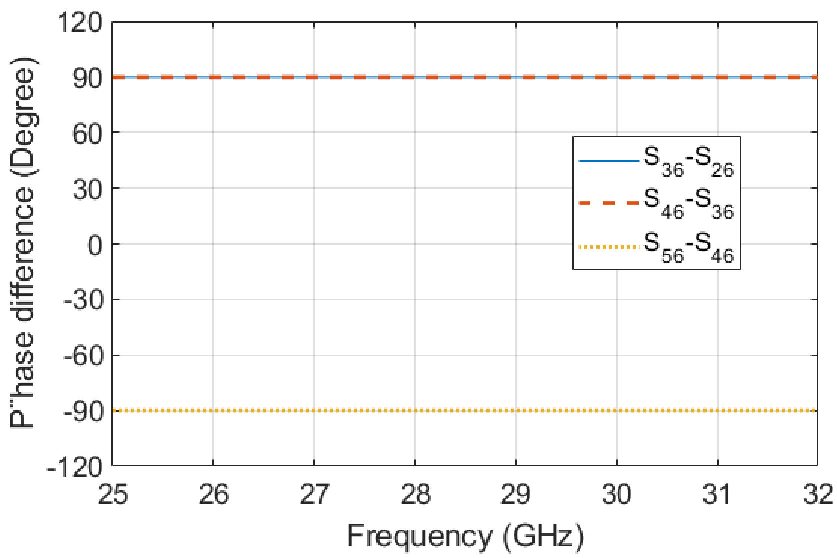

(b)

Figure 2.10 Simulated relative phase differences between (a) adjacent output ports for port1, and (b) adjacent output ports for port 6.

and port 2 to 5 are the output ports. Two loads were added to the 3 dB and 4.7 dB couplers respectively.

The potential to use the Nolen matrix as a demodulator is showing in Figure 2.10. This figure shows the phase difference between two adjacent output ports when port 1 is used as an input Figure 2.10 (a) and when the port 6 is used as an input Figure 2.10 (b). The phase distribution fellow the same distribution as the six-port defined by matrix in the equation 1.10.

2.5 Six port based on Nolen matrix with ideal components

To verify the feasibility to use the proposed Nolen Matrix as a demodulator, a building block diagram replaces the six-port (in Figure 2.4) in Figure 2.11. An ADS simulation showing the direct conversion receiver based on Nolen matrix with ideal components.

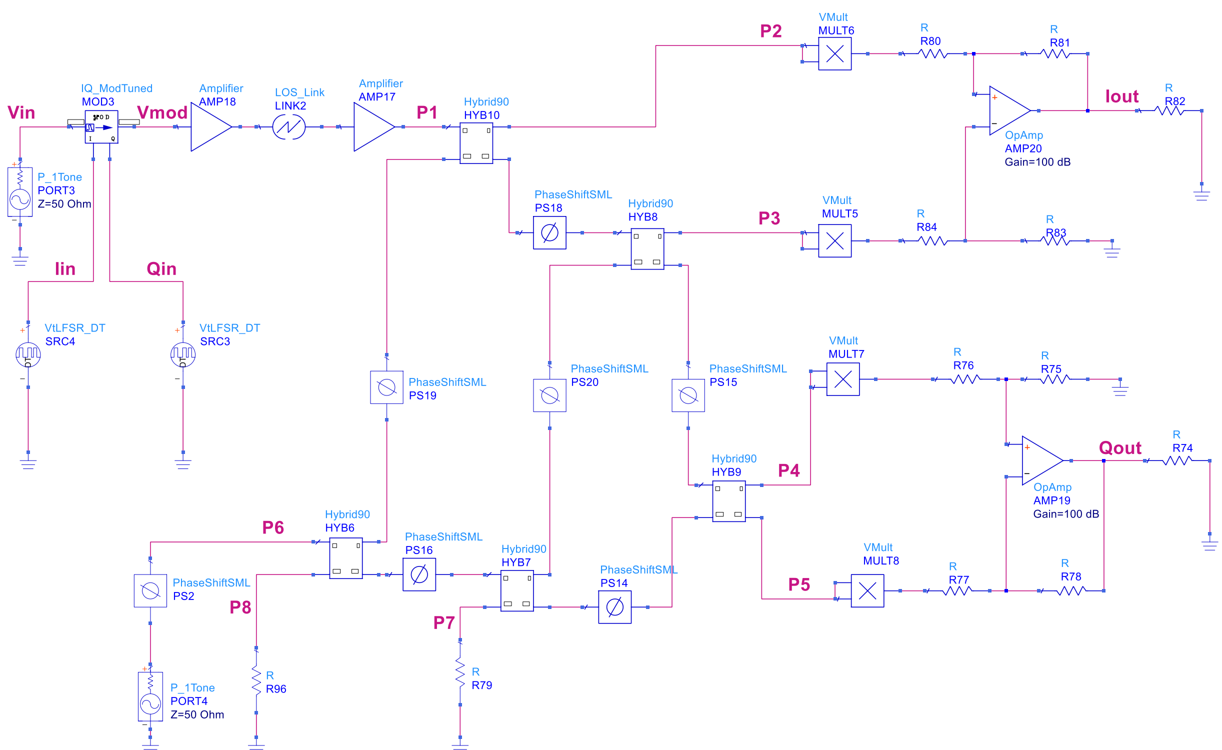

Figure 2.11 Six port based on Nolen matrix using ideal components.

Figure 2.12 shows the input and output signals in the range of 0 to 1 μs. From this figure, it is clear that the signals of the input QPSK modulation I_{input} / Q_{input} are in phase with the output signals I_{out} / Q_{out} respectively. It is noticeable the distortion in the recovered signals, a slight variation in voltage amplitude can be noticed.

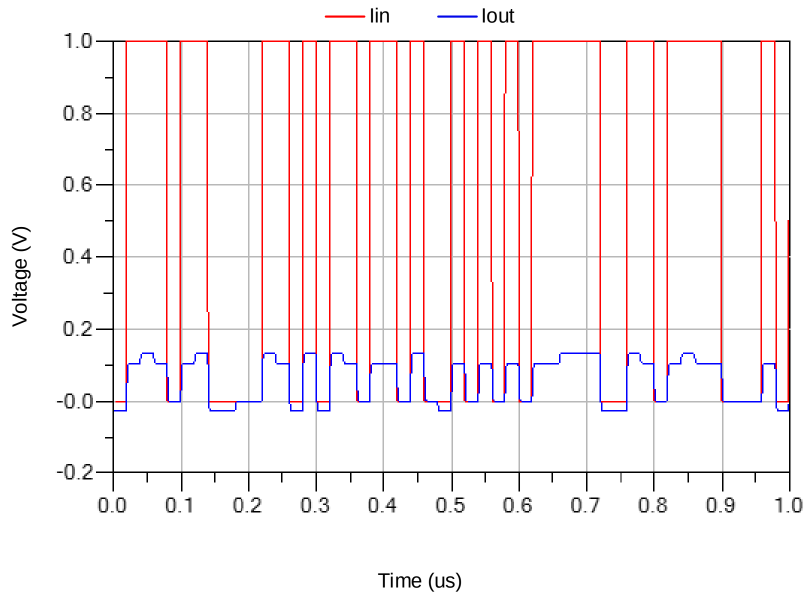

(a)

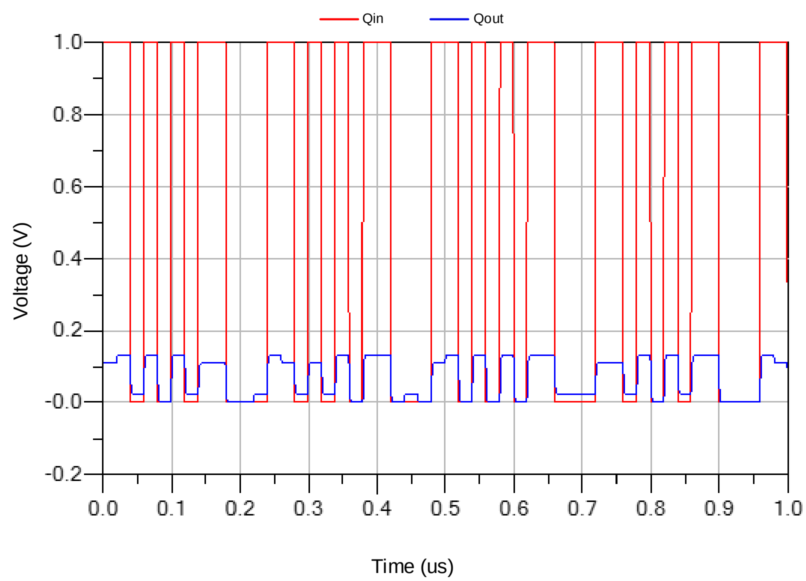

(b)

Figure 2.12 Input and output signals (a) Iinput/Ioutput in volt vs. time and (b) Qinput/Qoutput in volt vs. time.

Figures 2.13 and 2.14 are showing the spectrum of the input/output QPSK modulated/demodulated signals respectively. A good agreement has been shown between both signals input modulated and output demodulated QPSK, having an almost same specification, with the previous Figures 2.7 and 2.8 before applying the Nolen matrix.

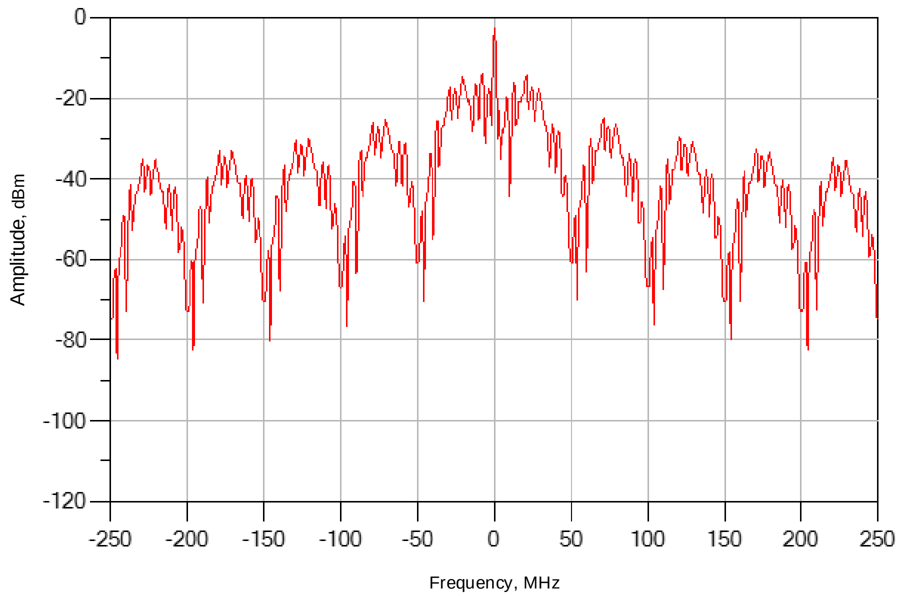

Figure 2.13 Spectrum of the input QPSK modulated signal.

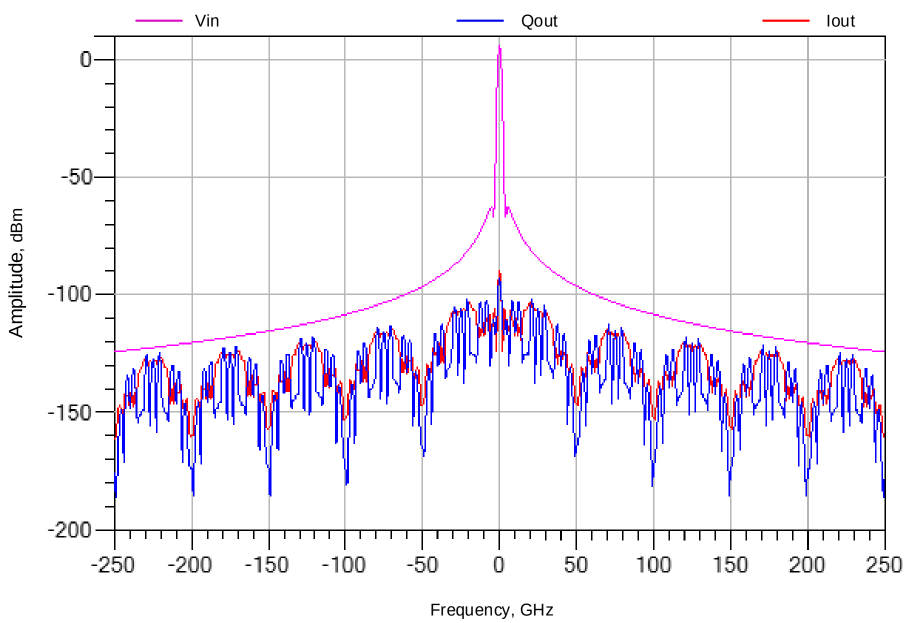

Figure 2.14 Spectrum of the output QPSK demodulated signals (I_{out} and Q_{out}) and the input signal (V_{in}).

CHAPTER THREE: Building Multi-Port System

In this chapter, three design steps are presented: couplers, phase shifter, and the multi-port. Three different hybrid couplers 3, 4.7, and 6 dB were discussed and designed. Moreover, a review is given about state of the art of phase shifter to introduce the proposed double T-shape phase shifter. The new proposed double T-shape phase shifter is discussed and designed using ADS software. Lastly, the multi-port based on Nolen matrix was designed.

3.1 Directional coupler

Hybrid couplers (or Branch line) are passive devices widely used in the microwave and RF circuits. What coupler is doing is coupling a portion of signal in the transmission line to the port enabling this signal to be used in different circuits.

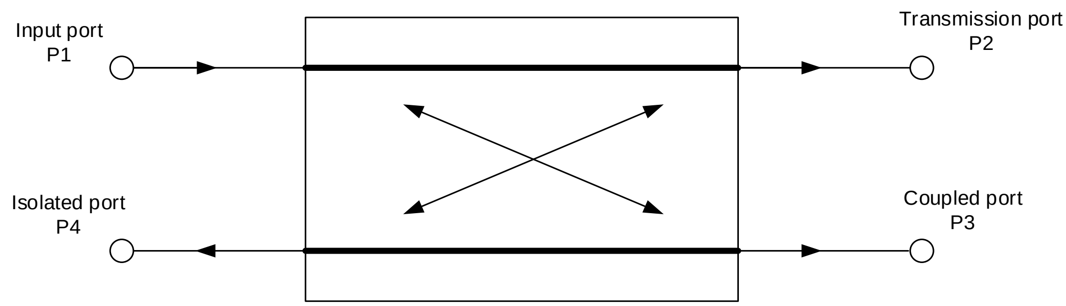

Figure 3.1 Single section 3 dB Hybrid couplers 90 °.

The branch line is the simplest type of quadrature coupler since the circuitry is entirely planar. An ideal single-box branch line coupler is shown in Figure 3.1 where each transmission line is a quarter wavelength. Branch line couplers are very easy to design and sufficient to use for some applications due to their ideal performance at the central frequency desired.

3.2 Double-box branchlines

The S parameter matrix of the symmetric coupler given by [28]:

$$[\boldsymbol{S}] = \frac{1}{\sqrt{2}} \begin{vmatrix} 0 & 1 & j & 0 \\ 1 & 0 & 0 & j \\ j & 0 & 0 & 1 \\ 0 & j & 1 & 0 \end{vmatrix} \tag{3.1}$$

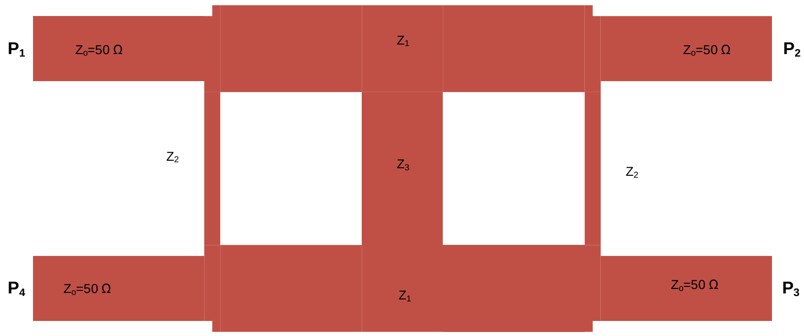

Figure 3.2 Layout of designed hybrid couplers 90 °.

The configuration of the designed hybrid coupler shown in Figure 3.2 is branch line version proposed in [29]. This version offers improved performance in terms of bandwidth and isolation and coupling ratio compared to the standard branchline coupler. The coupler has been optimized by modifying the dimensions and the coupling gape. All the three section lines used to define the coupler are a quarter wave. This is due to the quarter wavelength line (λ / 4) between the output ports. The impedance distribution defines the coupling ratio.

All the three coming hybrid couplers (3dB, 4.7dB, and 6dB) are following the same design procedure.

3.2.1 Hybrid coupler (3dB, 90 °)

The overall size of the coupler is (7.278×3.268 mm^2), and the used substrate is (Rogers_RT_Duroid6002) with a permittivity of 2.93 and a thickness of 0.254 mm. The coupler has been designed to operate in "broadband" mode (25 - 32 GHz).

Figure 3.4 show two sectors of the quarter-wavelength line, which form the structure of the coupler between ports 1 and 4, and between ports 2 and 3. We have a quarter wave line of characteristic impedance Z_o equivalent to that of the input and output ports of the coupler. On the other hand, between ports 1 and 2 and between ports 3 and 4, we have us quarter-wavelength line with a characteristic impedance of $Zo/\sqrt{2}$ to obtain a coupling of 3dB.

Figure 3.5 shows the simulated S-parameter results. A very good isolation and matching were obtained with S_{11} values of under -24 dB for the bandwidth. Moreover, the transmission coefficient is 3 dB at port 2 (S_{21}) and port 3 (S_{31}), which indicates that very low unbalance between the two output port.

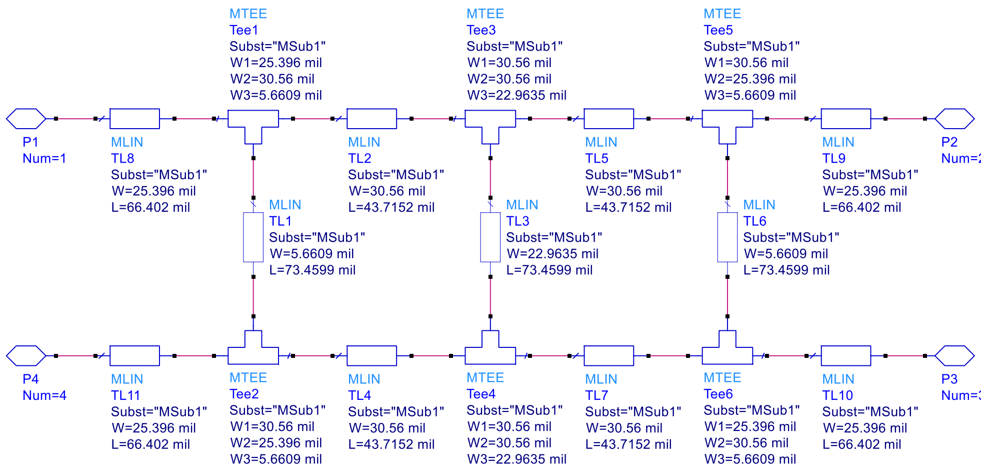

Figure 3.3 Simulation of Hybrid coupler (3dB, 90 °) in ADS.

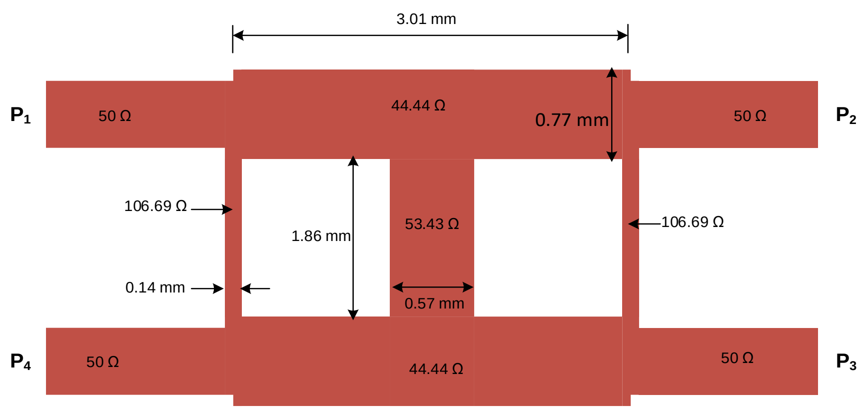

Figure 3.4 The Layout of the Hybrid coupler 3dB showing details about dimensions in (mm) and impedance in (Ohm).

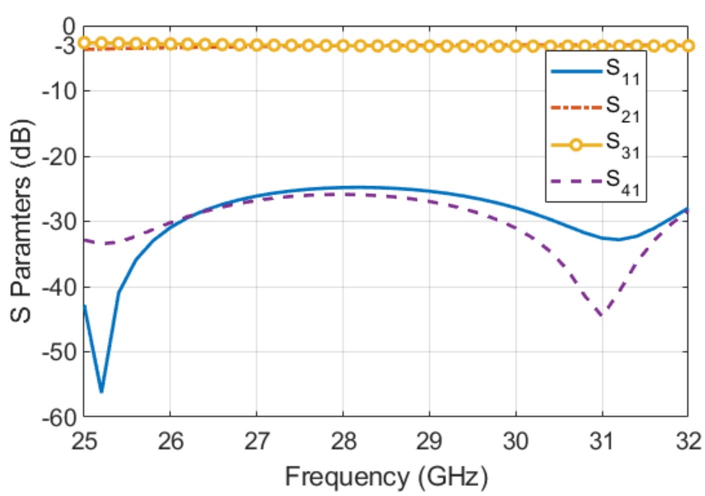

Figure 3.5 The simulated results showing S parameter of coupler 3 dB.

3.2.2 Hybrid coupler (4.7dB, 90 °)

The overall size of the designed 4.7 dB coupler is (6.696 × 3.5093 mm^2) with the used substrate (Rogers_RT_Duroid6002). Figure 3.7 is giving more details about the designed, dimensions (millimeter), and the impedance (Ohm) of the optimized 4.7dB coupler.

Figure 3.8 is a plot of the simulated S-parameters (Amplitude). The results for both isolation and matching are showing better than 20 dB for the band from 25.8 GHz to 32 GHz. In this bandwidth, the coupling is changing from to 4.6 dB to 5.2 dB delivering un unbalance of ±0.3dB.

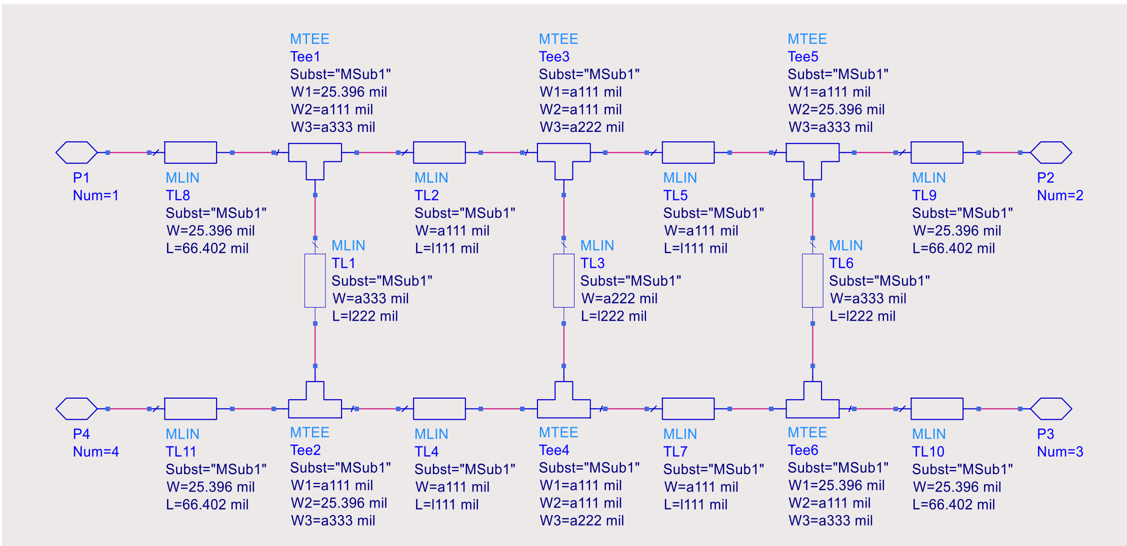

Figure 3.6 Simulation circuit of Hybrid coupler (4.7dB, 90 °) in ADS.

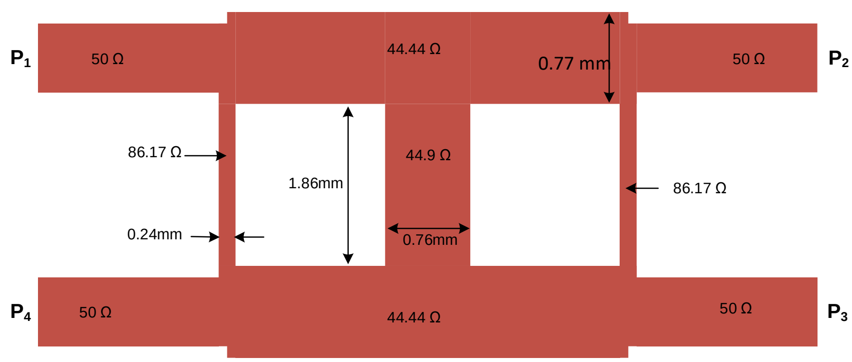

Figure 3.7 The Layout of the Hybrid coupler 4.7 dB showing details about dimensions in (mm) and impedance in (Ohm).

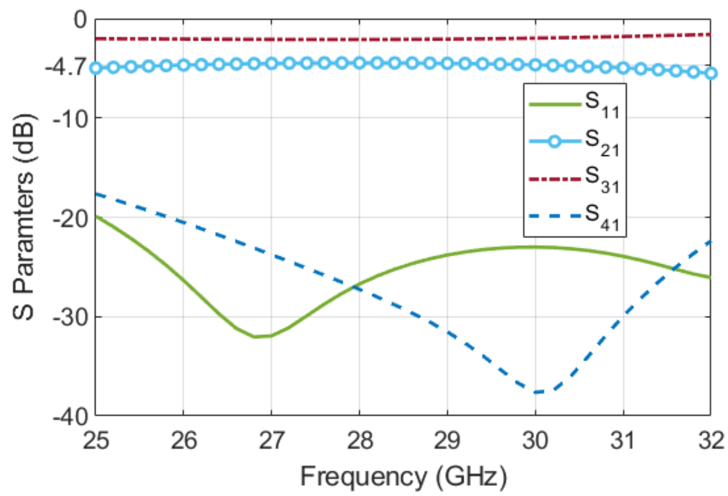

Figure 3.8 The simulated results showing S parameter of coupler 4.7 dB.

3.2.3 Hybrid coupler (6 dB, 90 °)

The overall size of the coupler is (6.74926 × 3.438 mm^2) with the same substrate (Rogers_RT_Duroid6002). The layout of the hybrid coupler is shown in Figure 3.10 with more details about the dimensions (in millimeter), and the impedance (in Ohm) of the 6dB coupler.

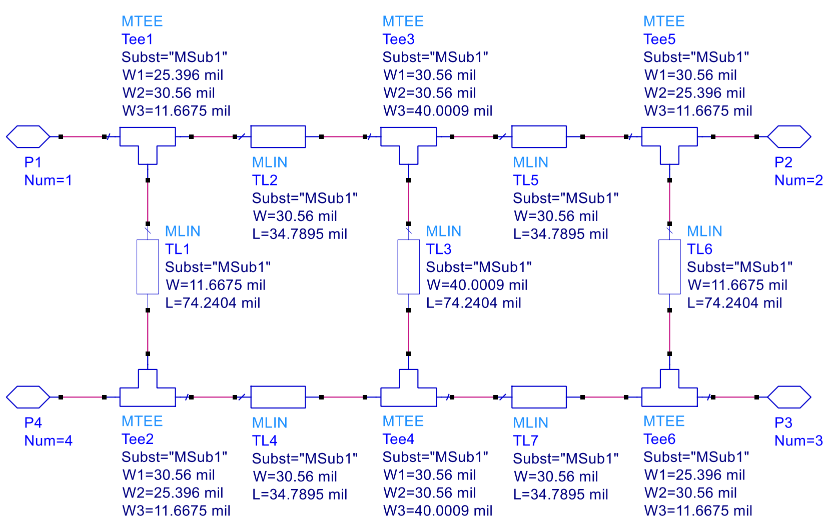

Figure 3.9 Simulation circuit of Hybrid coupler (6 dB, 90 °) in ADS

Figure 3.11 is a plot of the simulated S-parameters (Amplitude). The results for both isolation and matching are showing better than 20 dB for the band from 26.5 GHz to 31.5 GHz. Moreover, the transmission coefficient is of 6 dB for S_{21} at port 2 (S_{21}) and about 2 dB for S_{31} port 3 (S_{31}).

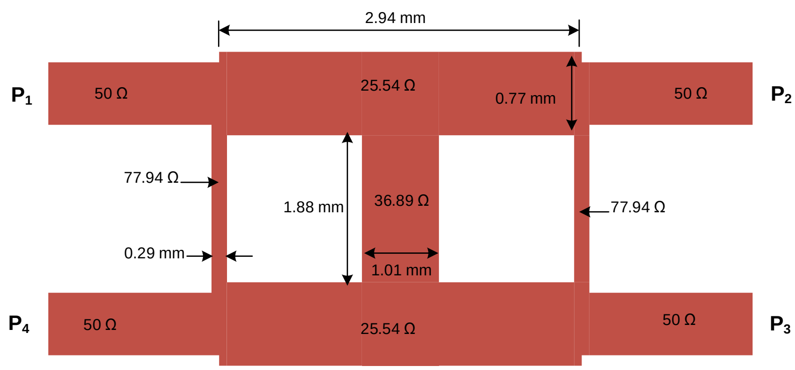

Figure 3.10 The layout of 6 dB hybrid coupler showing details about dimensions in (mm) and impedance in (Ohm).

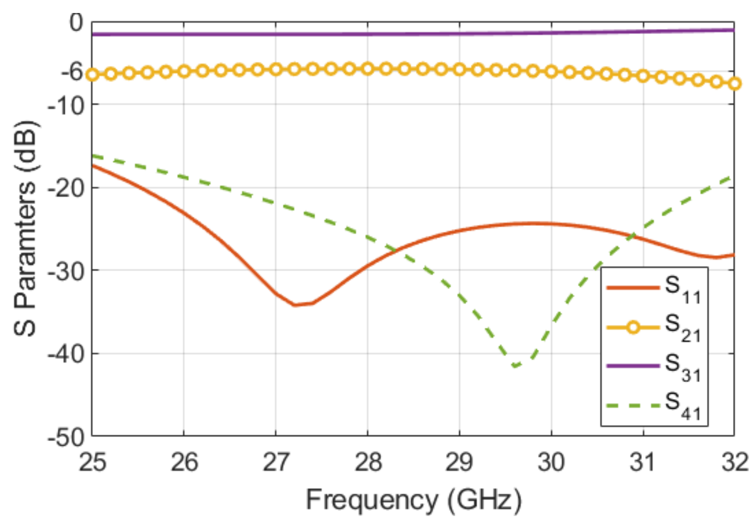

Figure 3.11 The simulated results showing S parameter of coupler 6 dB.

3.3 Phase shifter

Phase shifters are used for changing the phase angle of the two-port transmission line (S_{21}). The phase shifter should show a low insertion loss in all phase states, the equal amplitude for all providing a flat phase versus frequency within the desired bandwidth. Besides, the designed circuit should also satisfy the requirement of limited area.

3.3.1 Schiffman phase shifter

A constant input resistance 90° type phase shifter for larger bandwidths was described in [30] by Schiffman. An amplitude balance and broadband phase can be fulfilled by using several arrangements [31]. Figure 3.11 shows the general configuration of Schiffman Phase shifter [30] that has been used for a wide verity of applications playing the main role component in beamforming [31][32]. Schiffman phase shifter consists of two transmission lines. One line is bent over (coupled line) for dispersivation with of quarter wavelength and one line as a reference of three-quarters wavelength as is shown in Figure 3.12. A near constant phase difference can be achieved when considering a certain line length and coupling degree along broadbandwidth frequency. Schiffman demonstrated that the phase difference between quarter wavelength line and three-quarters wavelength is 90 ^{0}. The two equations (3.2) and (3.3) given below are describing the image impedance Z_I, and phase constant Φ respectively for Schiffman phase shifter [30]. Figure 3.13 is showing the connection of the coupled lines and their even and odd modes characteristic impedances of the lines and their length.

$$Z_I = \sqrt{Z_{0o} Z_{0e}}\ , \tag{3.2}$$

Z_I: Image impedance.

$$\cos \Phi = \frac{\frac{Z_{0e}}{Z_{0o}} - \tan^2 \theta}{\frac{Z_{0e}}{Z_{0o}} + \tan^2 \theta}\ , \tag{3.3}$$

Φ: Phase constant.

θ: is the electrical length of a uniform line length *L* and phase constant P.

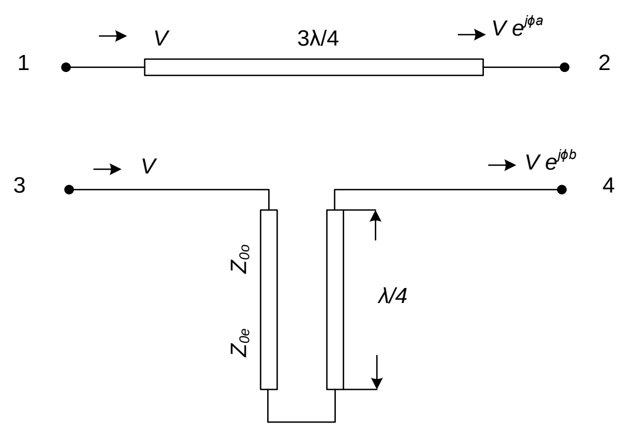

Figure 3.12 The Standard structure of 90^0 Schiffman phase shifter.

Figure 3.12 illustrates the basic Schiffman phase shifter principle work according to equations 3.2 and 3.3.

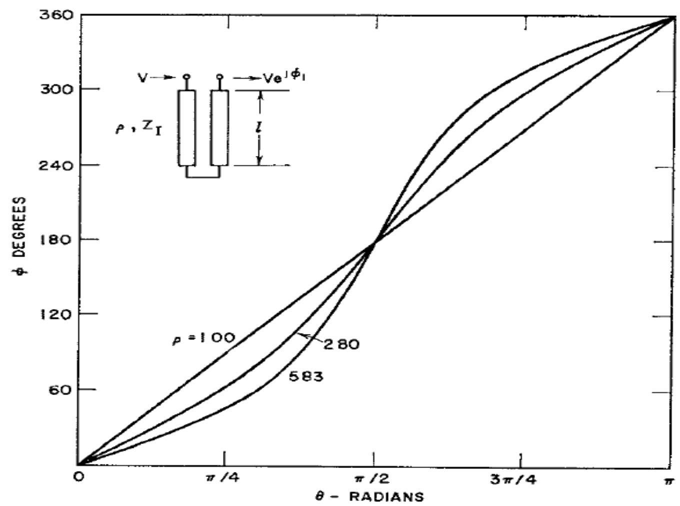

Figure 3.13 Coupled-transmission-line element with ends connected and curves of its phase response for three values of (ρ =Z_{0e}/Z_{0o}) [30].

3.3.2 Modified Schiffman phase shifter

Figure 3.14, designs worked on Schiffman Phase shifter toward larger bandwidth and accuracy [29]. This work use different configurations of transmission lines (Figures b, c, and d) to have more flexibility in term of the dimension (coupling space) defined by the coupling degree (ρ =Z_{0e}/Z_{0o}).

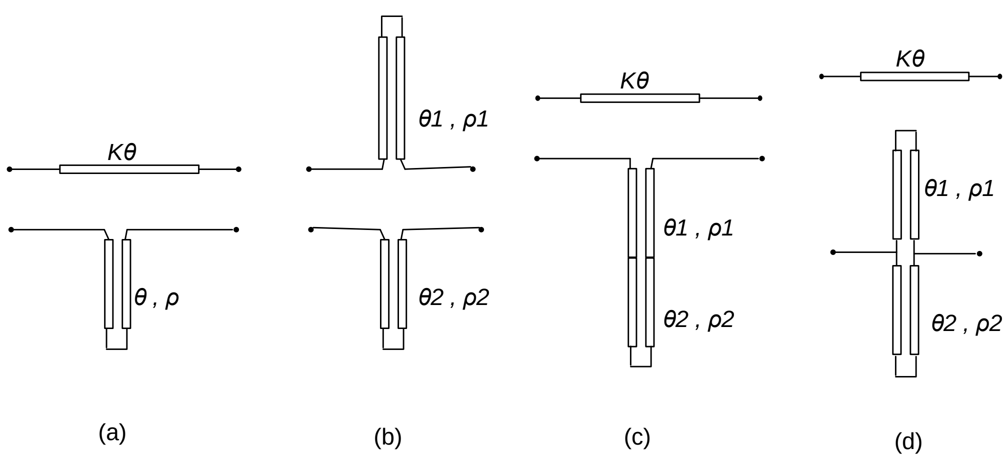

Figure 3.14 Some alternatives to obtain a differential phase shifter: (a) Standard Schiffman phase shifter, (b) Double Schiffman phase shifter, (c) Schiffman phase shifter with cascaded sections, and (d) Parallel Schiffman phase shifter [33].

Others modified Schiffman phase shifter based on improving the wide-band by increasing the even mode when the ground plane under the coupled lines removed. Vice Versa, reducing the odd mode when an additional rectangular conductor is applied [32].

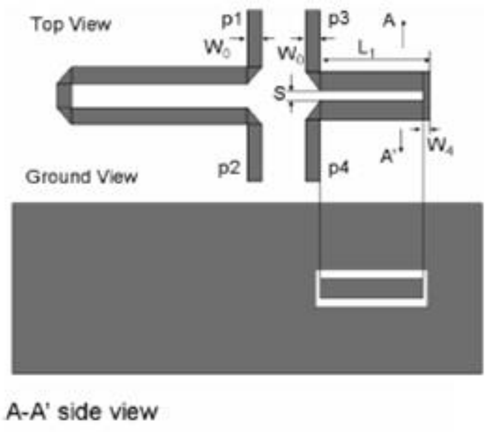

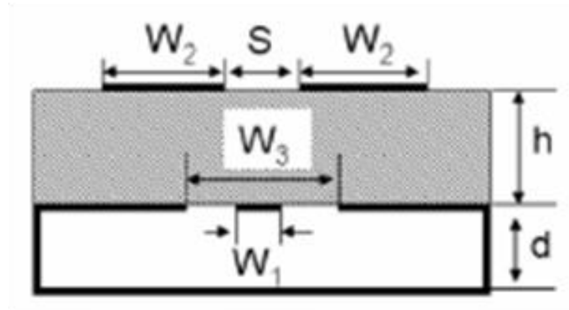

Figure 3.15 A 90^0 Schiffman phase shifter layout using a patterned ground plane [32].

Based on the above details, the previous shapes of phase shifter cannot be compatible with the proposed circuit of this thesis both bandwidth and spacing problem. The distance between the two lines of the phase shifter is defined by the distance between the two input ports of the coupler. In this section, we propose miniaturized phase shifter (see Figure 3.16) that works well in terms of the desired bandwidth and the limited space of the circuit.

3.3.3 Double T - shape phase shifter

In the review of Schiffman's phase shifter and to the modifications that were added to it. The phase shifter that proposed here is designed to reduce the area used and to maintain the quality as of phase shifting with high performance. A substrate form simulated, designed and fabricated for the proposed design double T-shape phase shifter. This newly proposed structure tackles the limited spacing problem and is integerable with designed couplers in the desired circuit. Where here, a study has been made to bend the two sides of modified Schiffman shifter.

3.3.4 Double T-shape phase shifter 90 ^{0}

This technique employs the proposed double T-shape, which is different of the conventional designs as is shown by the general shape in Figure 3.16. Because this method mainly aimed for reducing the size, it can be useful for many applications when the limitation of the area is the concern, especially when working in mm Wave bands where circuits are very small. It is worth mentioning that, both top and bottom T-Shapes are symmetrical for each element of the phase shifter (see Figure 3.16). The top one T-Shape element dimensions: the width of coupled lines set at 0.08 mm for entire the element, and the coupled lines gape set at 0.20 mm in the horizontal

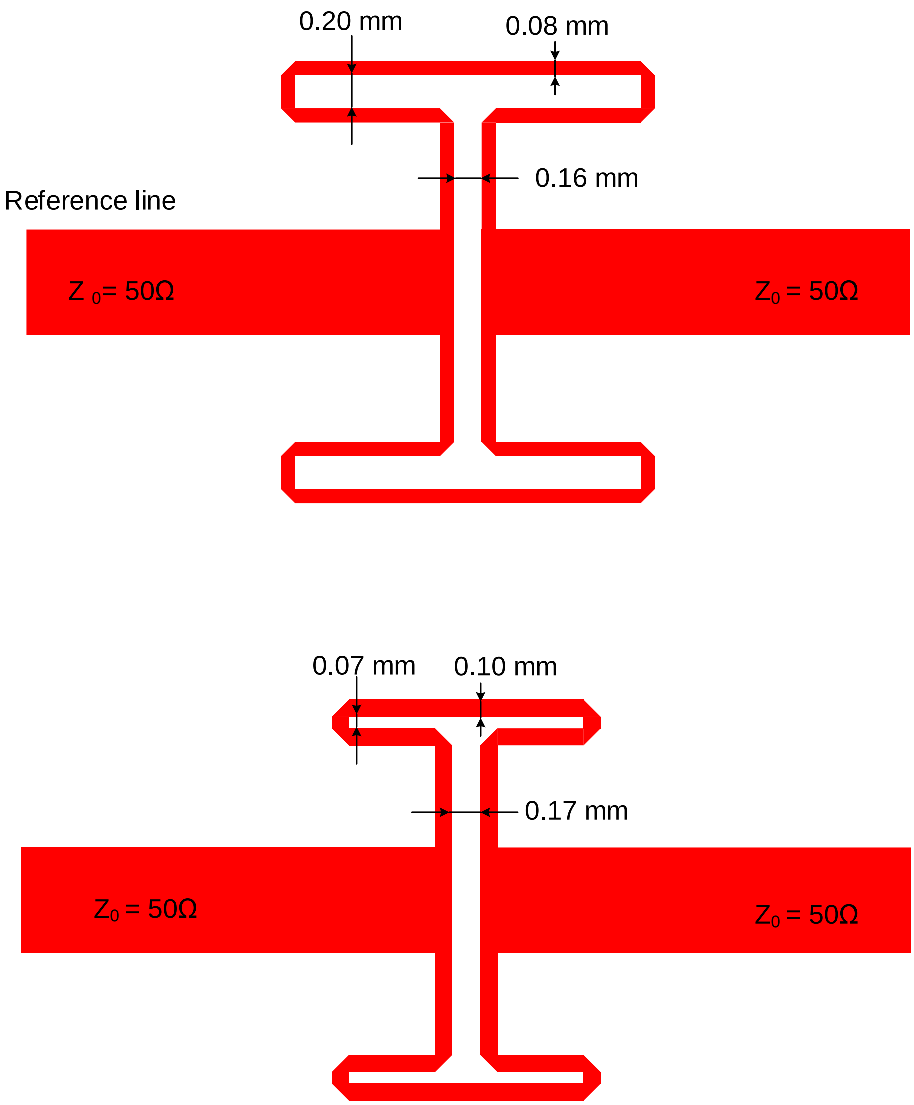

Figure 3.16 The layout of the proposed 90° double parallel double T-shape phase shifter with considering the symmetry for each element.

plane and 0.16 mm in the vertical plane (with considering the symmetry for each element). For the bottom element the dimensions: the width of coupled lines set at 0.10 mm for entire the element, and the coupled lines gape set at 0.07 mm in the horizontal plane and 0.17 mm in the vertical plane (with considering the symmetry for each element).

The results plotted in figures show a very good phase shifting over the proposed broadband width frequencies of roughly ($90^0 \pm 2^0$) around the desired frequency (28 GHz). Showing significant results for a bandwidth (7.75 GHz) from 26.25 GHz to 34 GHz. Moreover, the achievement of acceptable results in terms of the reflection coefficient ($S_{11} \approx$ -13 dB) for the entire bandwidth.

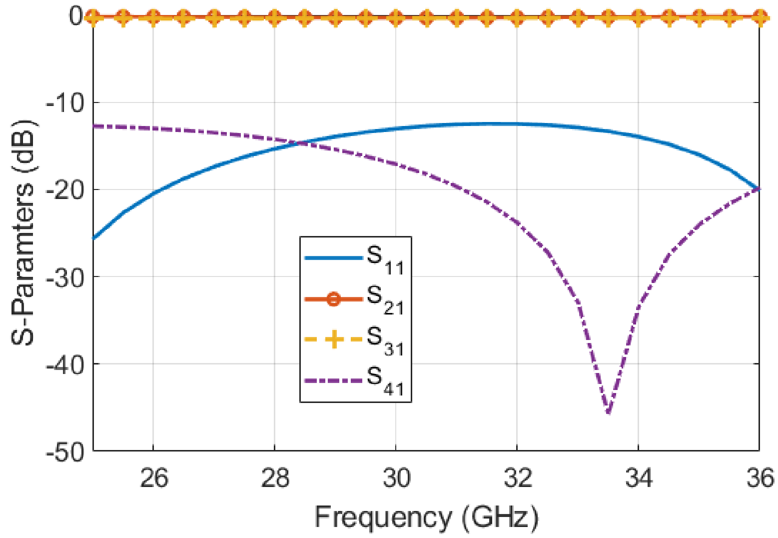

(a)

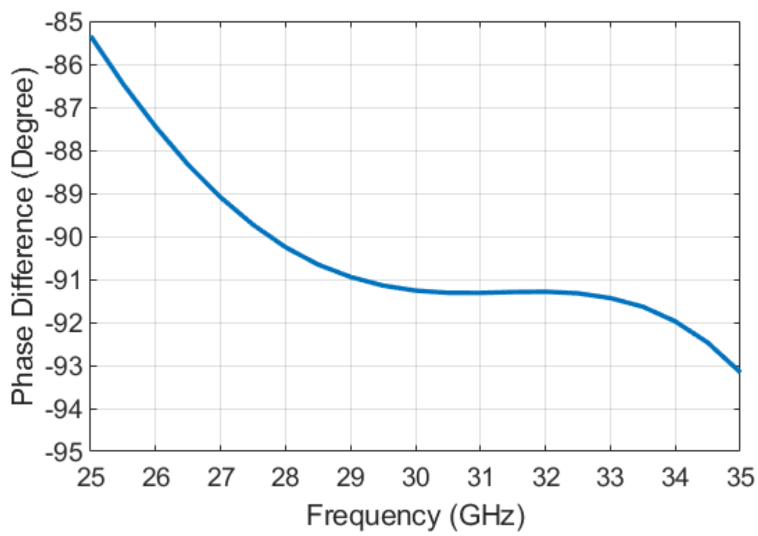

(b)

Figure 3.17 Simulated results of the proposed 90 T-phase shifter. (a) Amplitude response. (b) Phase response.

3.4 Designed Nolen matrix using ADS

Nolen matrix based on a conventional network topology is designed at the center frequency of 28 GHz with roughly 5 GHz bandwidth. The designed branch line couplers have a phase shift of 90°, so this point must be taken into the consideration. An optimization step was done. As it is expected theoretically, a phase deferent can be a problem due to a deferent transmission lines length.

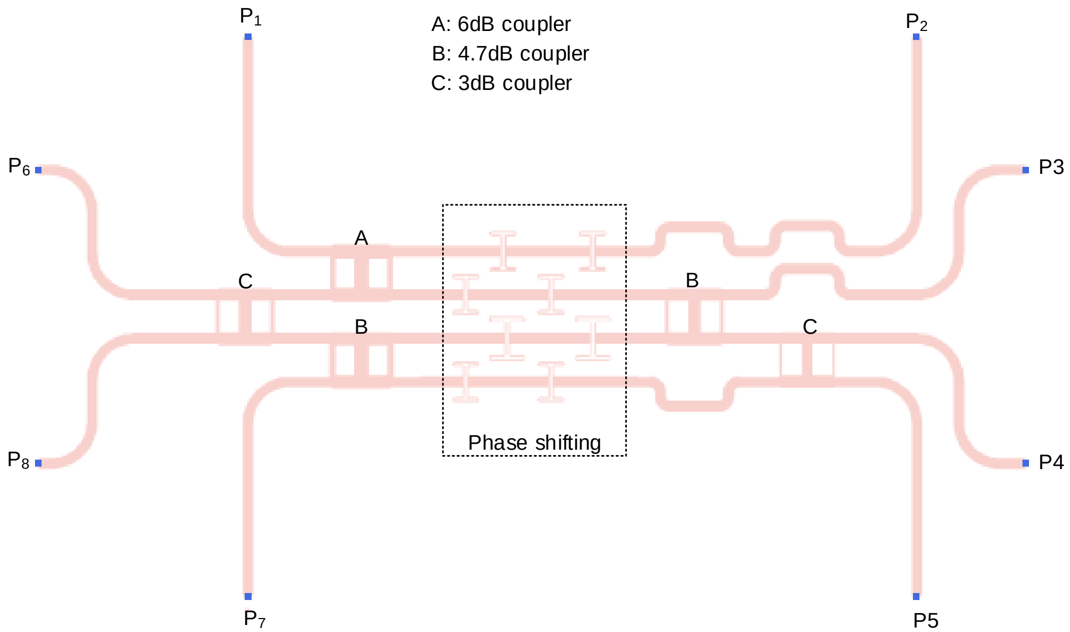

Figure 3.18 The layout of the six-port demodulator based on Nolen matrix.

The proposed solution is a Nolen matrix where the different paths must be aligned as much as possible to increase the bandwidth. An almost parallel architecture is used in this matrix. Compensation of the delay generated by the couplers will ensure broadband behavior. This matrix has an advantage in terms of its performance that can be comparable to Butler matrix with the possibility of designing matrices with any *N* x *M* combination besides to the main advantage of separating the inputs and output.

Figure 3.18 shows the simulated layout from Momentum (ADS). Equal transmission lines are added to the initial design to discrete the input access as well as the output to facilitate the characterization and to compensate the phase difference.

Figure 3.29 is showing the energy distribution and the isolation when the excitation applied to the input ports (P1 and P6) one each time. First, P1 is excited to show the energy distribution in the four output ports (P2, P3, P4, and P5) where the other input ports P6, P7, and P8 (P7 and P8 are unused ports) were isolated. The last step was repeated for the other input port P6 to show the energy distribution in the four output ports (P2, P3, P4, and P5) where the other input port P1

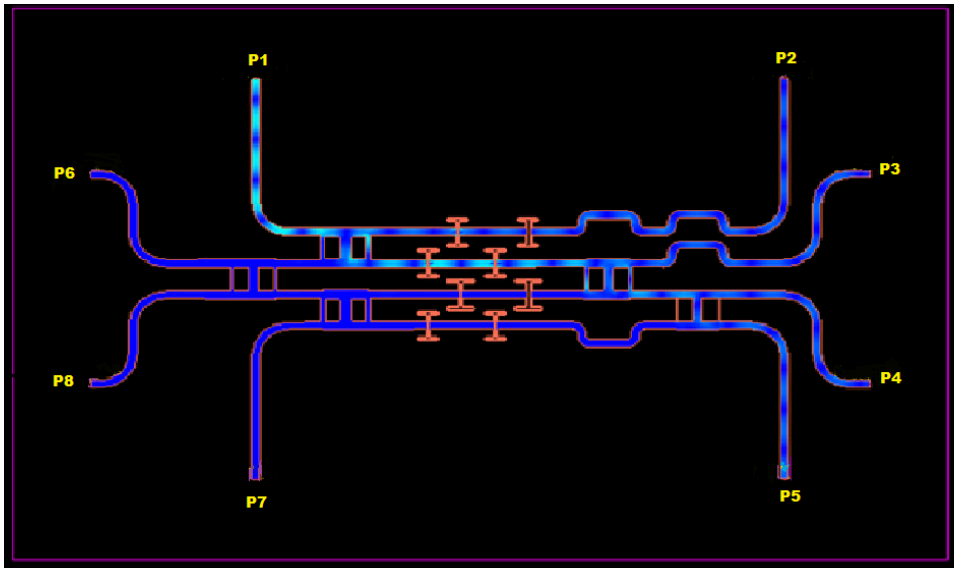

(a)

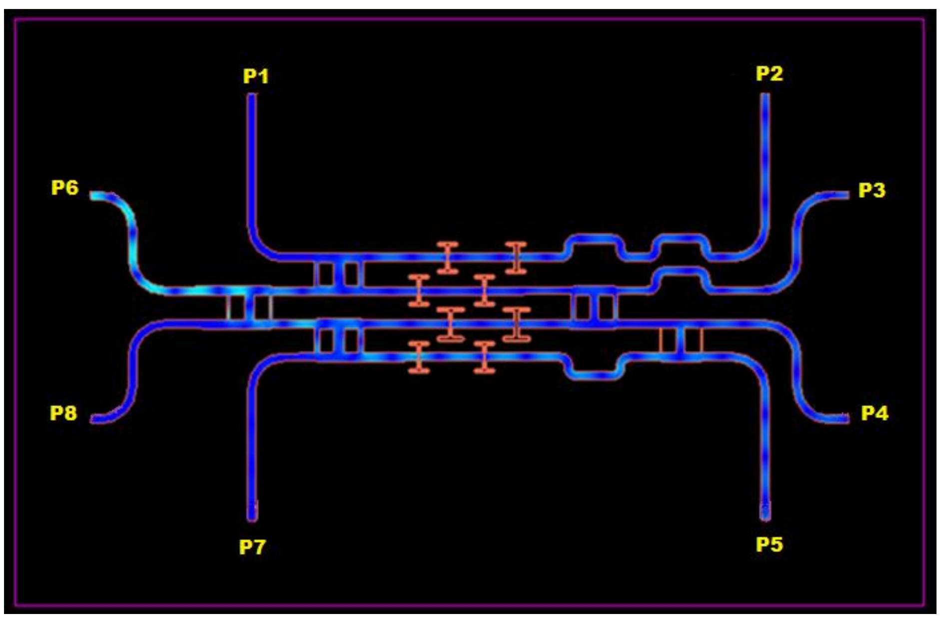

(b)

Figure 3.19 The electric field distribution (a) when port 1 excited (b) when port 6 excited

was isolated and the unused two ports P7, and P8 were isolated as well. A good isolation can be noticed and normal distribution by applying this technique.

CHAPTER FOUR: Experimental Validation

In this chapter, the simulated and measured results are presented and discussed. The results are showing an excellent correlation between simulated and measured performances and highlighting the potential of the proposed multi-port based on Nolen matrix. In order to validate the proposed broadband direct demodulator based on Nolen matrix for the 5G communication system, a circuit was fabricated and measured for characterization.

4.1 Fabricated circuit

The circuit of the multi-port based on Nolen matrix was fabricated on a Rogers RT/duroid 6002 Laminates substrate. It has a dielectric permittivity of 2.94 with substrate thickness of 10 mil. The dimensions of the fabricated circuit are 62 mm (in length), 35 mm (in width), and 0.254mm (in height). The prototype of the fabricated multi-port based on Nolen matrix circuit is shown in figure 4.1. All the ports are numbered as illustrated in the last chapter. Port 1 and 6 are the access for the RF and LO signal respectively. Ports from 2 to 5 are considered as the output ports and they will be connected to the power detectors. The unused two ports (7 and 8) should be

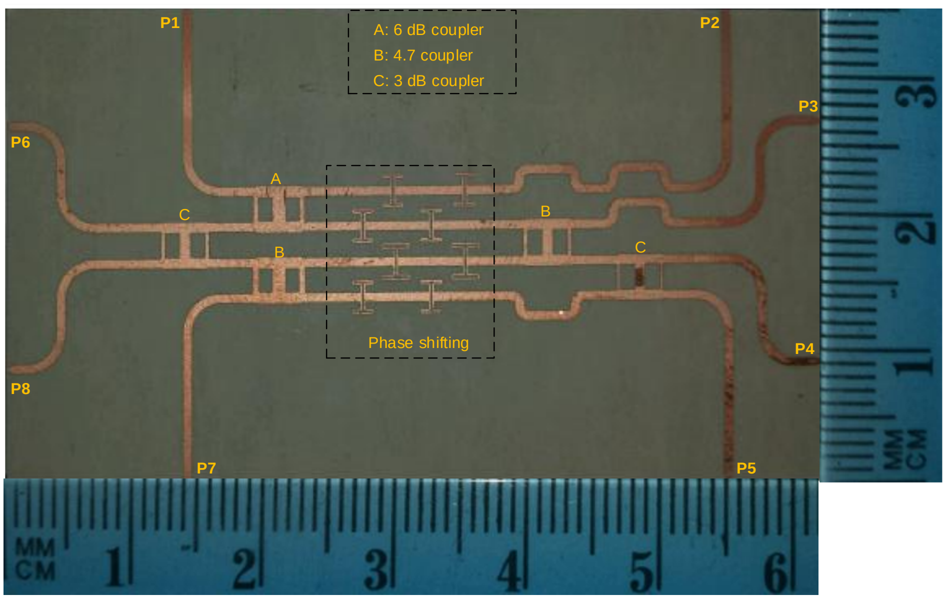

Figure 4.1 Photograph of the fabricated circuit.

connected to loads. To characterize the performance of Nolen matrix, S-parameter should be measured to calculate the important characterizations such as the input isolation S61, the input matching at the ports, the transmitted power from the RF and LO ports to the output ports, and the phase difference between transmitted signals. The calibration used is VNA is the standard SOLT.

4.2 Experimental results

The simulated and measured return losses at input ports (port 1 (RF input) and port 6 (LO input)) are illustrated in figure 4.2 (a) and (b) with simulated counterparts. At the central operating frequency, 28 GHz within (27 – 32 GHz) band all values are better than 20dB. Giving the best results within the frequencies (27.5 – 29.8 GHz) band for values of under -27dB. In addition, the measured values are better than 12 dB at the highest frequency allowed for 23.5 – 33.5 GHz band communications.

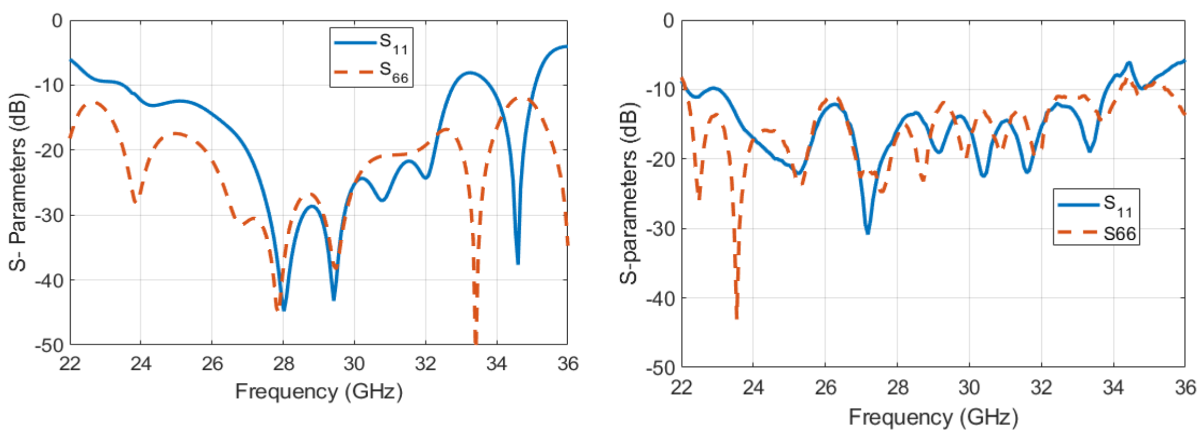

a) b)

Figure 4.2 Input matching): a) Simulated, b) Measured.

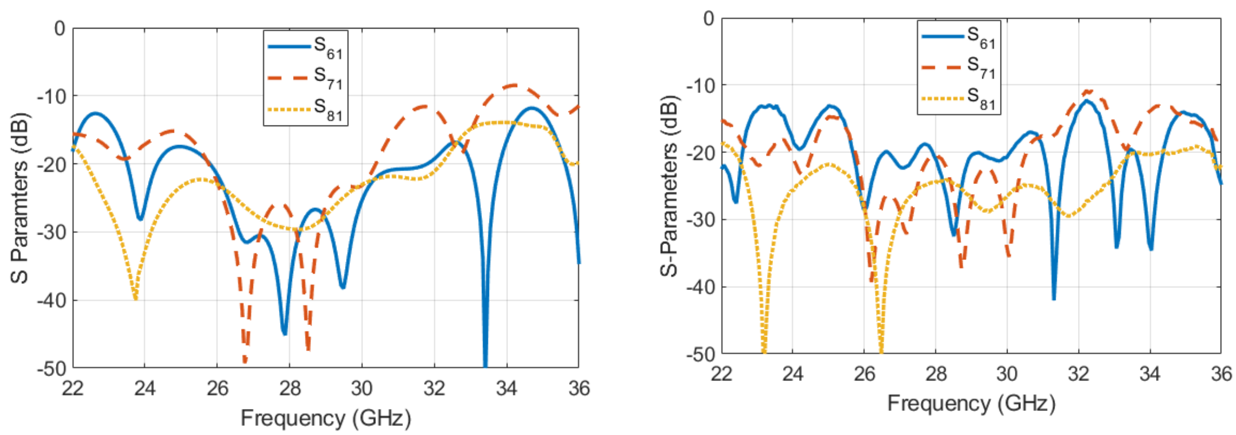

a) b)

Figure 4.3 Inputs isolation S parameter: a) Simulated, b) Measured.

Figure 4.3 shows the simulated and measured isolation between the input ports (S_{61}), and the isolation between the input port 1 and the two unused ports (P_7 & P_8) according to the port numbering specified in Figures 4.1. From Figure 4.3 (a), the obtained isolation values (from simulation) are excellent since all are better than 20 dB for the entire frequencies (26 – 30.4 GHz) band. While the isolation values for the measured results are roughly 20 dB in the same frequency band hence both results having an agreement as it was expected.

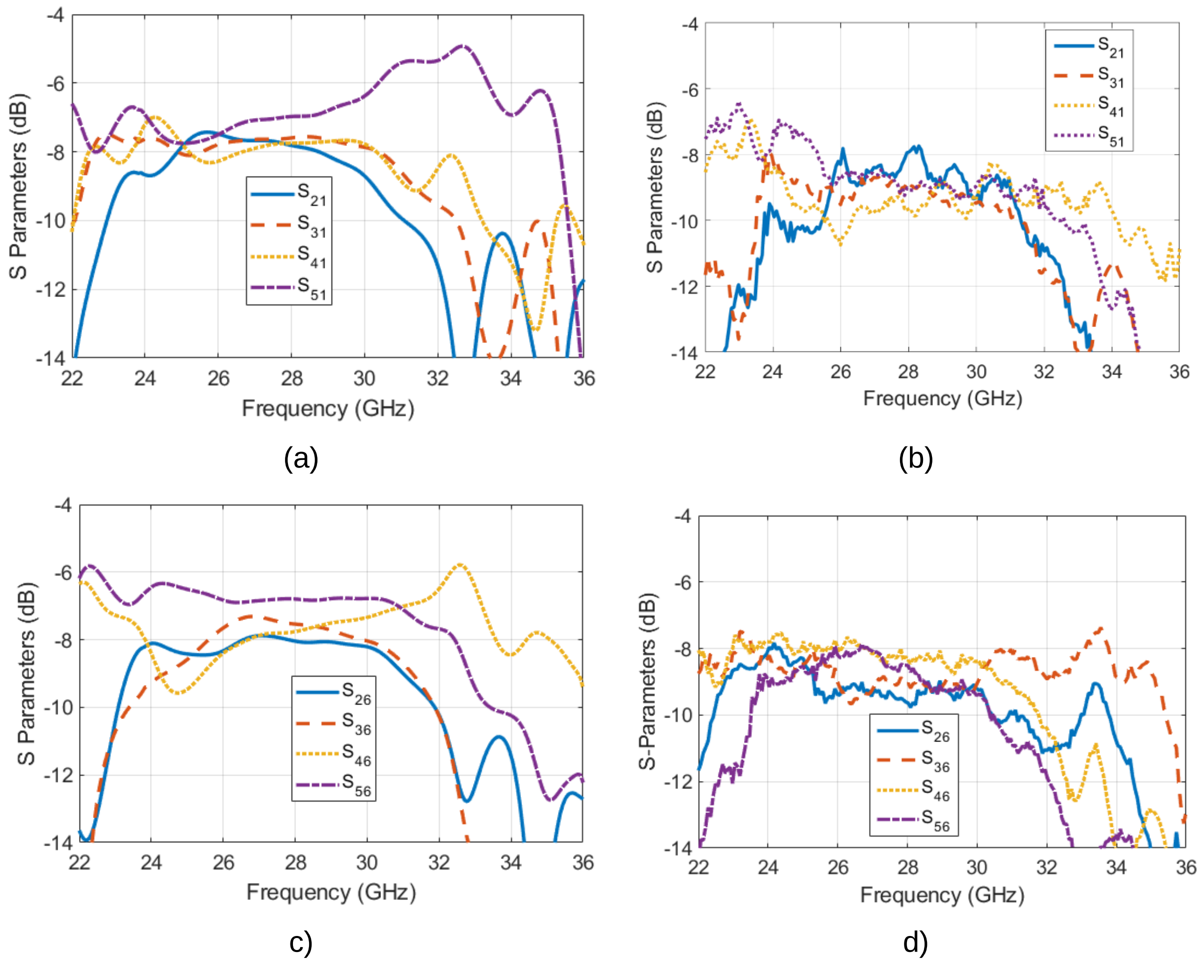

Figure 4.4 Transmission Coefficient (Amplitude): a) Simulated port 1, b) Measured Port1, c) Simulated Port 2, d) Measured port 2.

Figure 4.4 shows the power splitting between the RF/LO ports and the four adjacent output ports S_{2X}, S_{3X}, S_{4X}, and S_{5X} (Where $_X$: could be 1 for port 1 or 6 for port 6). As compared to the theoretical value of -6 dB, very good results are obtained over the band. The results show less than 1.5 dB of supplemental insertion loss (which is acceptable at this band). The metallic and dielectrics losses are considered in this simulation. The unbalanced magnitude is close to ±1 dB from 24 to 30 GHz. In the measurements, good results have been obtained over the considered frequency band with additional loss of 1 dB and unbalanced magnitude of ±1 dB.

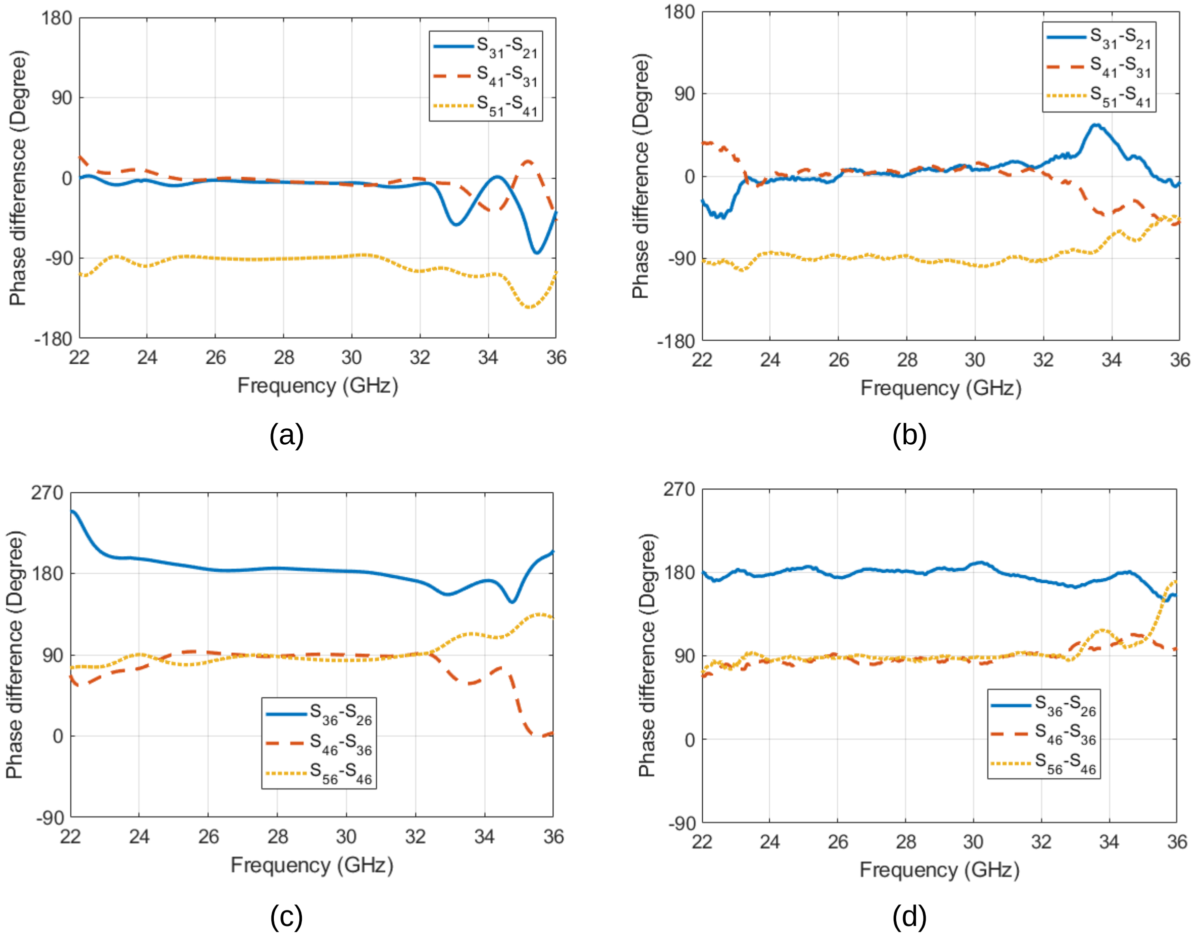

Figure 4.5 Transmission Coefficient (phase): a) Simulated port 1, b) Measured Port2, c) Simulated Port 2, d) Measured port 2.

Figure 4.5 shows the phase difference between each two adjacent ports transmission S-parameters. The measured phase difference between the two outputs is close to the quadratic reference of 90° (and multiple of 90°), as expected. The phase difference of 0^0, 0^0 and -90^0 (when port1 is considered at input) are reached unlike the ideal one proposed in Figure 2.10. The phase difference of 180^0, 90^0 and 90^0 respectively (when port6 is considered at input) unlike the ideal one proposed Figure 2.10. These permutations do not affect the performance of the multi-port as a demodulator. The idea in six-port based demodulator is to have four different combinations of the LO and RF signal. The used couplers are -90^0 instead of $+90^0$ used in the block design.

A phase from -10^0 to -2^0, -8^0 to -1^0, and -90^0 to -86^0 are reached at the output port when port 1 is fed from 26 to 30 GHz. A phase from 181^0 to 184^0, 88^0 to 93^0, and 81^0 to 89^0 are reached at the output port when port 6 is fed. In the measurements, the same performances were achieved, with almost identical values, to simulation results values in the 26 - 30 GHz bandwidth. The error is less than 10 degree for all the ports.

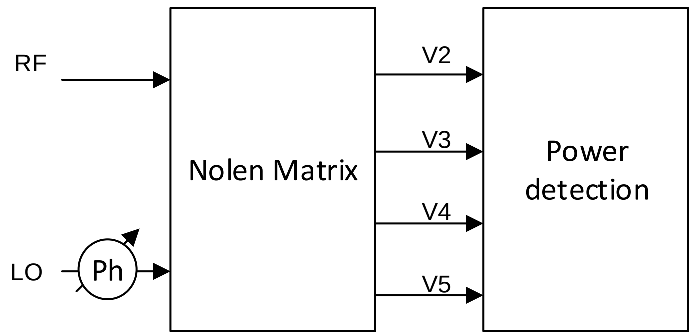

Figure 4.6 Block diagram displaying the multi-port output voltages.

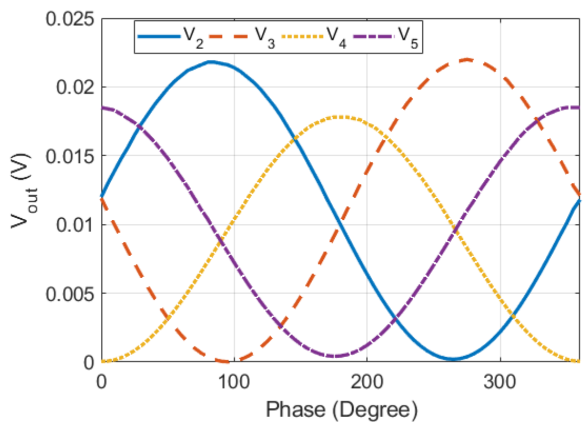

Figure 4.7 Nolen Matrix as phase discriminator.

To resume the measured performances of the Nolen matrix and their effects on the multi-port demodulator, the Nolen matrix is tested as phase discriminator considering the measured S-parameters. The Nolen matrix was fed by the RF and LO signals with same frequency without any modulation and the Lo phase is changed from 0 to 360 degree. These signals went through the combination to proceed to four outputs V2, V3, V4, and V5 as illustrated in Figure 4.6.

The simulated four output voltages are shown in Figure 4.7 (simulated with ADS). It is noticeable that every two signals are opposite to each other (V2 vs. V3 and V4 vs. V5), and all the signals are centered to 0° with almost 90° shifting one to the another. Therefore, I/Q signals could be achieved using this technique.

4.3 Constellation

To test the Nolen matrix based demodulator set of Modultation are simulated considering the measured Nolen matrix S-paramters. The modulation types were applied to the circuit are BPSK, QPSK, and 8PSK in both cases ideal and realistic. The demodulated signal constellations are shown in Figure 4.8. From the figure, it is noticeable that the ideal case there was no distortion appeared on the constellation (on the left column), which is that how it should be since it is the ideal. On the other hand, the entire constellation figures (on the right column) are having distortion (in both phase and amplitude) this happen because of white noise that was added in the transmission path, which is the real case. Furthermore, the noise is represented by the cloud around the I/Q signals.

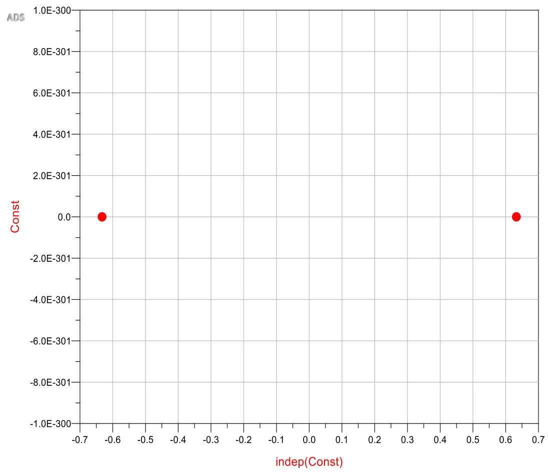

BPSK (ideal case)

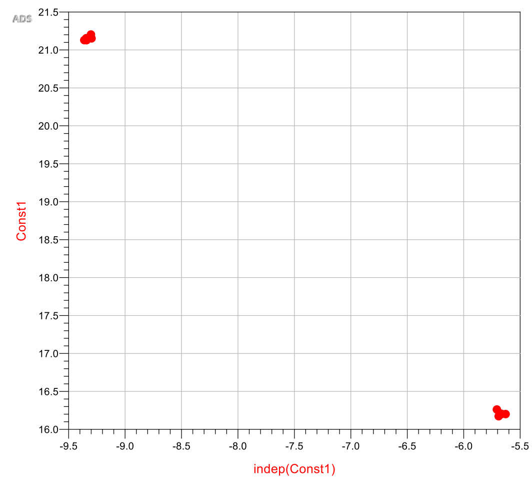

BPSK (realistic case)

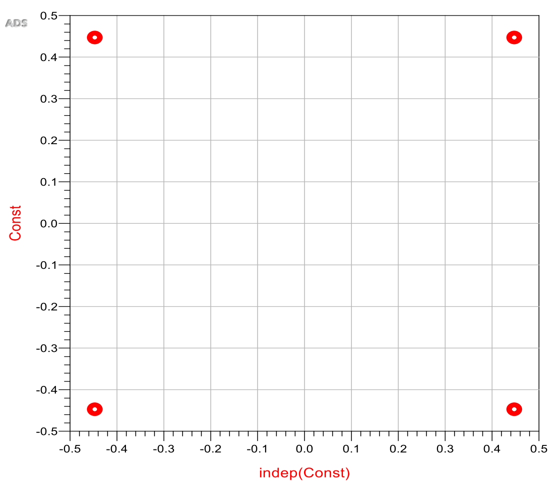

QPSK (ideal case)

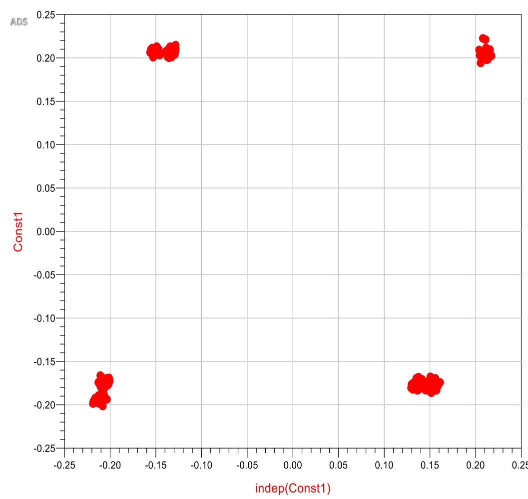

QPSK (realistic case)

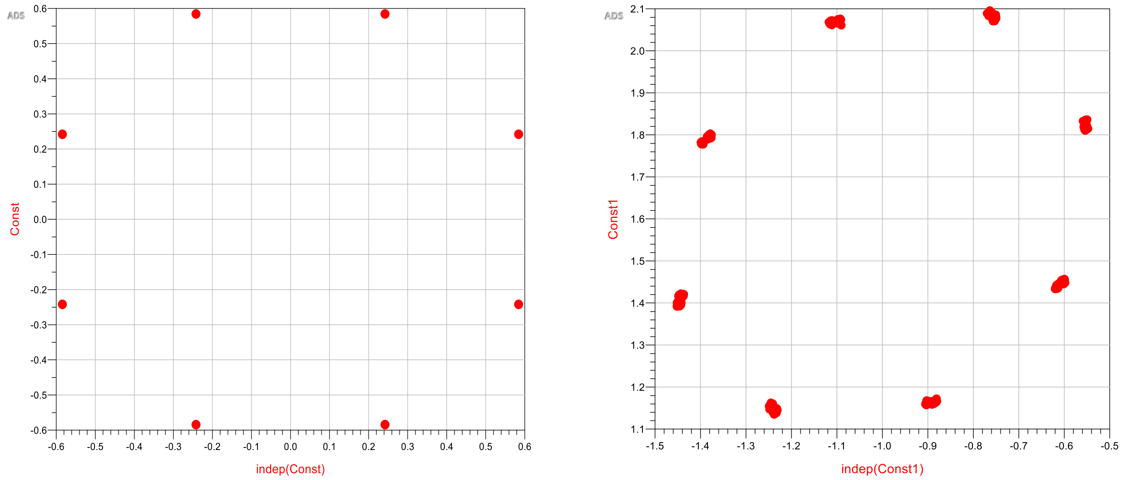

8PSK (ideal case) **8PSK (realistic case)**

Figure 4.8 Simulated constellations of the demodulated signal considering ideal and measured S-parameters of the proposed Nolen matrix (BPSK, QPSK, and 8PSK). 40 MHz of data rate is considered with 150 m of distance between the transmitter and receiver with free space channel.

The overall performance study of the multi-port based on Nolen matrix is showing a very reliable operation at the frequency 28 GHz and within 26 – 31 GHz frequency band generally. Also, the quadrature signals obtained at multi-port outputs for the minimum values of voltages put forward to be a good member in 5G technique.

CHAPTER FIVE: Contributions and Future Work

Today the mm Wave communication technology in the 28 GHz frequency band is growing, and it is expected to play a core role in the next generation technology communication system.

A wideband planar multi-port based on Nolen matrix has been designed and demonstrated to operate over 26 - 31.5 GHz band. The wideband performance of the multi-port junction attributed to the wideband design of its components. Notably, the double T-shape phase shifter is designed based on the principle of bent line phase shifter to reduce the used foot print. The introduced double T-shape phase shifter shows good performances over the desired bandwidth. This chapter resumes the main contributions and the ideas related to the multi-port for the future work.

5.1 Contributions

The use of the multi-port based on Nolen matrix as reflectometer is proposed, discussed, designed, and fabricated for validation. Moreover, this study has been made to show that the proposed multi-port based on Nolen matrix can be a member of the millimeter wave next generation communication systems. Furthermore, this design is assuring the desired adaptation in the multi-port by the separation of the inputs and outputs.

A sub-design was simulated, fabricated, validated taking into the account the space limitation in the proposed design. The double T-shape phase shifter is adequate well to the restricted spacing of the multi-port based on Nolen matrix. The new design of the double T-shape phase shifter showed an excellent performance over the desired bandwidth. At the beginning of this work, theoretical approaches of the six-port discriminator were reviewed and discussed. The used basic circuits at millimeter frequencies, including the branch line hybrid coupler H-90 °, double T-shape phase shifter, as the multi-port reflectometer was designed and validated using ADS (schematic and momentum). The circuit designed is broadband with comparable results to the standard six-port. In this context, the proposed multi-port based on Nolen matrix will be the core of the proposed millimeter system especially when it is related to the next generation system.

- Nolen based multi-port performance

The measured results since the S-parameters have shown that the proposed model of multi-port is operating well at 28 GHz. A good matching for all ports; results are better than -20 dB. The isolation between RF and LO ports (1 and 6, respectively) is at least 20 dB. The magnitudes of transmission coefficients S_{21} to S_{51} and S_{26} to S_{56} are close to -8 dB and close to -7.5 dB respectively. The phases of transmission coefficients match the theoretical values.

- The S-parameters were injected on demodulator to build realistic ADS simulation. The output voltage versus the phase show excellent performance in term of phase differences between the output voltages and acceptable in term of unbalance power. Therefore, I/Q demodulated output signals are obtained by this structure for different modulation schemes.

- Double T-shape phase shifter

We also conducted a study on the phase shifter and developed a miniaturized double T-shape phase shifter (about 50 % of footprint). The results of simulation of this phase shifter, have demonstrated high that constant phase difference can be achieved.

At the end of this work, we completed the final prototype of the 28 GHz mm Wave frequency multi-port based on Nolen matrix. The obtained results confirm the design approach of multi-port and enable high-performance, integrated for future high-speed wireless communication receivers.

5.2 Future work

Measurement setup with adequate modulator (signal generator/modulator) via coaxial cable and/or antenna for modulation are going to be integrated. A power detector to be designed simulated and validated to build up the whole receiving system. The performance of the Nolen matrix as receiver should be quantified with BER for different type of modulation.

The future work is going to be around building up the transceiver system by designing the modulator using the same Nolen technique. However, a very essential point remains to improve, which is the repeatability of current manufacturing processes to allow better results, in terms of the circuit integration and prototypes manufactured. Specifically, the parts that concern the integration of active components, such as including the detectors and the amplifiers built in within the circuit. After building transceiver system, using this transceiver system based on Nolen matrix technique (Modulator and demodulator mode), it is important to study the combination these techniques with beamforming technology by designing or rebuilt the whole system with considering the compatibility with beamforming technique.

CHAPTER SIX : Résumé

6.1 INTRODUCTION

Ce chapitre présente une introduction aux systèmes de la cinquième génération (5G) et leurs fréquences de fonctionnement. En outre, il fournit une vue d'ensemble de l'architecture des modules de réception et les démodulateurs à ondes millimétriques (mm Wave).

6.1.1 Technologie 5G

Le principal progrès à venir dans les normes de télécommunication mobile est la technologie 5G [1] [2] [3]. L'avancée ne sera pas seulement une simple extension de la quatrième génération (4G) mais va générer des changements fondamentaux. Le tableau 6.1 résume les principales spécifications relatives au 4^{e} et 5^{e} génération actuelle et à venir.

Tableau 6-1 Les technologies actuelles et futures technologies 5G.

	Actuel	**5G**
Technologie	Réseaux Multi- standard Cat-M1/NB-IoT Fonctions optimisées du nuage La virtualisation des fonctions réseaux	Gigabit LTE (TDD, FDD, LAA) Massive MIMO Configuration des tranches de réseau et d'y associer des fonctions de routage et de calcul destinées au contrôle des données.
Enhanced Mobile Broadband	Screens everywhere	New tools
Automotive	On demand Information	Real-time information vehicle to vehicle
Manufacturing	Process automation	Flow management and remote supervision
Energy and utilities	Metering and smart grid	Resource management and automation
Healthcare	Connected doctors and patients	Monitoring and medication e-care

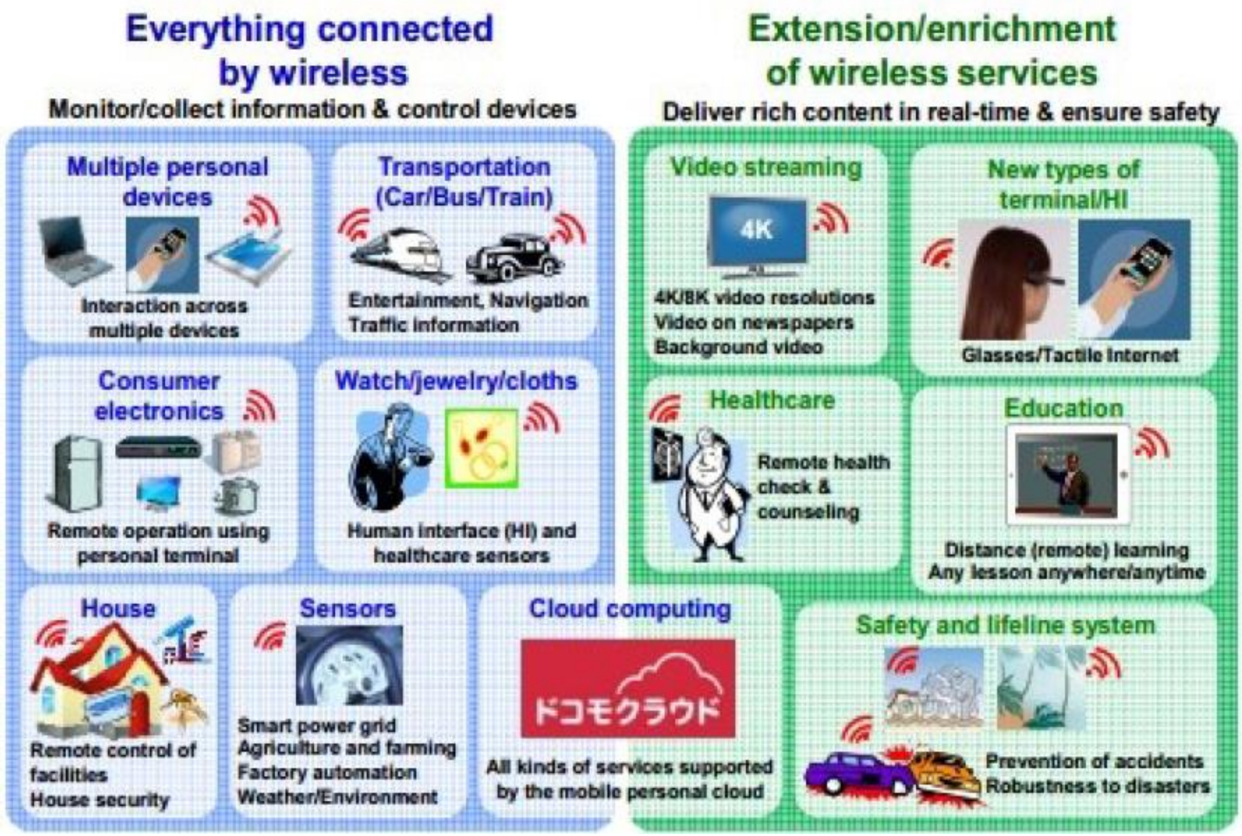

Figure 6.1 Tendances des services 5G [6].

Applications 5G

La Figure 6.1 décrit l'augmentation de la demande en transfert de données par rapport à ce qui est déjà utilisé, comme pour les maisons intelligentes, le transport intelligent, etc. Ainsi que l'extension des services sans fil pour les soins de santé, l'éducation à distance et de nombreux autres exemples mentionnés dans le même graphique.

6.1.2 Disponibilité du spectre 5G

Selon la consultation publiée en juin 2017 par Innovation, Sciences et Développement économique Canada (ISDE), la grande demande en connexions sans fil sollicite un nouveau spectre, des services et des technologies. Cette consultation a pour objectif de libérer un spectre en ondes millimétriques (mm Wave) dans les bandes de fréquences 28 GHz, 37-40 GHz et 64-71 GHz.

À l'échelle mondiale, d'autres pays cherchent à élaborer et à adopter rapidement les normes de la 5G. En particulier, l'allocation des fréquences plus élevées. Les États-Unis, en accord avec la commission fédérale des communications (FCC), soutiennent le développement des réseaux sans fil 5G et l'établissent de nouvelles règles pour faciliter les innovations [4] [5]. Les États-Unis ont de nouvelles règles qui permettent d'utiliser une bande autour de 28 GHz (27.5-28.35 GHz), une bande à 37 GHz (37-38,6 GHz) et une bande à 38 GHz (38.6-40 GHz); cependant, la bande de fréquences 64-71 GHz a des fréquences sans licence. La FCC a adopté ce qu'on a appelé le « service d'utilisation flexible des micro-ondes supérieures » (UMFUS). L'UMFUS est un spectre pour les bandes de fréquences 28 GHz, 37.6-38.6 GHz et 39 GHz nécessitant une licence [3]. En outre, l'Union internationale des télécommunications (UIT) étudie une gamme de onze bandes de fréquences comprises entre 24 et 86 GHz qui devraient être utilisées à l'avenir par les services mobiles à large bande. L'UIT ne se concentre pas sur l'étude de la bande 28 GHz, les États-Unis, le Japon et la Corée du Sud souhaitent poursuivre l'autorisation locale d'opérations mobiles dans cette bande de fréquence. Actuellement, au Canada, ISED continue de fournir aux innovateurs un accès à court terme permettant l'essai d'équipement [3].

La recherche universitaire et le prototypage industriel ont concentré leurs efforts sur la bande 28 GHz pour le développement de technologies de services mobiles. Cela pourrait être compréhensible avec une bande passante de 850 MHz pour permettre la mobilité dans les bandes millimétriques.

La technologie 5G couvre différentes bandes de fréquences, dans ce travail, la conception est portée sur la bande mm Wave autour de la fréquence de 28 GHz.

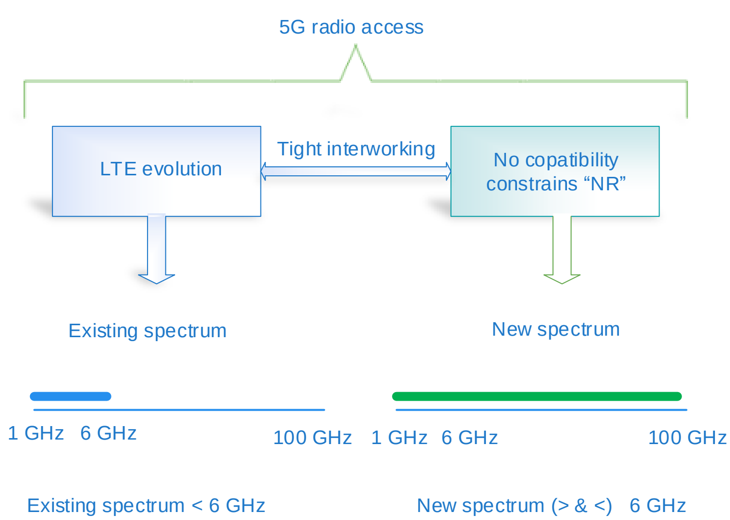

Figure 6.2 Vision de l'accès radio pour 2020 et les années précédentes: L'accès radio 5G contient une nouvelle technologie d'accès radio (NR) et une évolution LTE qui n'est pas inversée et qui fonctionne de 1 GHz à 100 GHz [7].

6.1.3 Sélection de fréquence

Au Canada, ISED a permis aux innovateurs d'expérimenter les nouveaux équipements, tels que les équipements de détection, la transmission vidéo utilisant des fréquences non conventionnelles et les systèmes mobiles dans les bandes de fréquences millimétriques. De plus, ISED autorise des études flexibles sur les bandes de fréquences des 28 GHz et 37-40 GHz, qui sont compatibles avec les développements en cours de la technologie 5G [4].

6.1.4 Architectures des systèmes de réception

La Figure 6.3 illustre l'architecture la plus utilisée généralement au niveau de la réception. Le signal détecté par l'antenne ne contient pas seulement l'informations, il est souvent associé au bruit et à d'autres signaux inutiles. L'amplificateur à faible bruit (LNA) et le filtre passe-bande à l'entrée du récepteur sont utilisés afin de réduire le niveau de bruit [8] [9]. Tous les récepteurs sont construits autour des mêmes éléments essentiels pour la récupération du signal utile avec un degré de complexité différent [9].

La partie RF d'un récepteur a pour rôle de transposer la fréquence du signal reçu à une fréquence centrale, inférieure à celle reçue. Le signal reçu est démodulé et traité afin qu'il soit transmis à la destination finale. Il existe deux catégories principales de récepteurs, les récepteurs homodynes dont le passage des fréquences RF aux fréquences basses se fait directement. Le second type est le récepteur hétérodyne dont le passage des fréquences RF vers les basses fréquences se fait en plusieurs étapes.

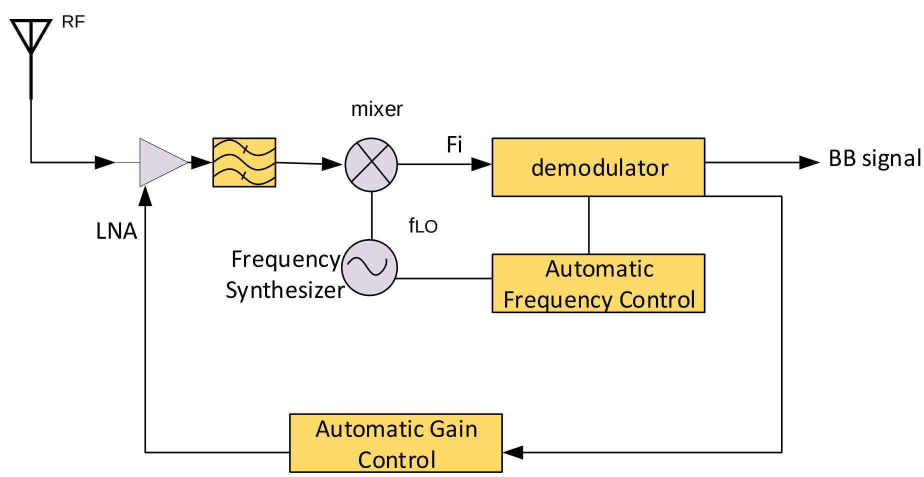

Figure 6.3 Architecture du système de réception.

Récepteur direct (démodulateur)

Le schéma de principe du démodulateur à six ports est illustré à la Figure 6.4. Où, le démodulateur à six ports est décrit par trois principaux blocs. Il s'agit du corrélateur à six ports, un détecteur de puissance et la récupération en bande de base.

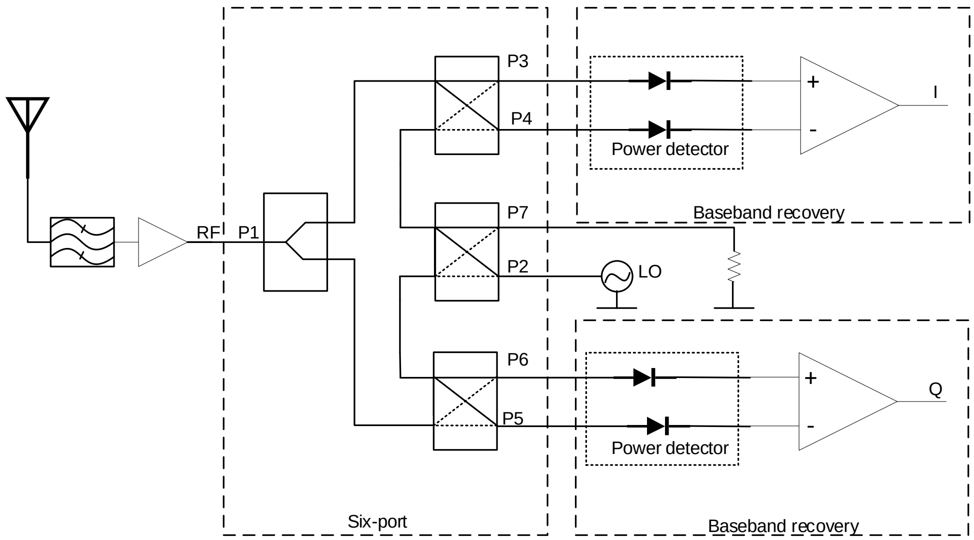

Figure 6.4 Schéma de principe d'un démodulateur six ports.

Corrélateur multi-ports

À cet étage, un signal d'oscillateur local (LO) est combiné au signal RF modulé. Comme le montre le schéma synoptique du six ports, les signaux RF (après modulation) et LO sont combinés avec un certain déphasage. Ce déphasage est déterminé par les paramètres S du corrélateur à six ports [8].

Détection de puissance

Dans la plupart des démodulateurs à six ports, on utilise un détecteur de puissance à base de diode Schottky. La non-linéarité de la diode Schottky est assurée dans une plage de fréquences bien définie. Dans un détecteur de puissance idéal, la fonction de transfert de la région quadratique décrite dans l'équation ci-dessous, et elle modélise le courant du détecteur de puissance en fonction de la tension [8].

$I_{PD}(v) = kv^2$

Où k est une constante.

Récupération en bande de base

Chaque deux sorties des diodes sont connectées à un amplificateur différentiel en bande de base. La sortie de chaque amplificateur sera la différence entre ses entrées (les sorties des diodes), ces signaux récupérés forment les deux composantes I et Q.

6.1.5 Démodulateurs à ondes millimétriques

De nos jours, des études et des mesures démontrent clairement que la 5G en bande millimétrique pourrait être choix robuste pour les futurs systèmes 5G [4] [5]. Le tableau 6.2 présente les paramètres de performance pour différents types de récepteur millimétrique, ainsi qu'une comparaison entre les différentes techniques. Cette comparaison montre que le récepteur multiport a plusieurs avantages spécialement pour la démodulation de signaux à faible puissance.

Tableau 6-2 COMPARAISON DES PERFORMANCES DES TECHNIQUES HETERODYNE, HOMODYNE ET MULTIPORT (EN CE QUI CONCERNE LES ARCHITECTURES DE RÉCEPTEUR À BASE DE DIODES) [10].

Performance Indicator/Parameter	Heterodyne Scheme	Homodyne Scheme	Multiport Scheme
Dynamic range	Excellent	Good	Average
DC power	high	average	Very low
LO requirement (power and f-stability)	Average	High	Low
Signal sensitivity	Excellent	Good	Good
Harmonic control	Difficult	Average	Easy
IP3	Average	Good	Excellent
Port-to-port isolation	Difficult-to-achieve	Average	Easy-to-achieve
Conversion loss	Good	Good	Excellent
Noise figure	Excellent	Good	Average
Structure complexity	High	Low	Average
Wideband/multiband flexibility*	Average	Good	Excellent

6.2 CHAPITRE DEUX : Conception de la matrice de Nolen

Dans ce chapitre, une analyse de la matrice de Nolen sous différents aspects est présentée, en expliquant la corrélation qui existe entre cette matrice et les six ports.

6.2.1 Formation de faisceaux

Les réseaux de formation de faisceaux (BFN) sont des dispositifs ingénieux comprenant des circuits formés de coupleurs directionnels et de déphaseurs fixes. Il existe plusieurs techniques de formation de faisceaux capables de fournir des faisceaux fixes : les matrices de Butler, Blass et Nolen, ou lentille (Rotman et Bootlace).

Dans cette section, nous allons décrire en bref les matrices BFN en expliquant le principe de fonctionnement

Matrice de Butler

La matrice de Butler (Figure 6.5) est un système parallèle qui est composée de jonctions qui connectent les ports d'entrée aux ports de sortie par des lignes de transmission de longueur égale. Ainsi, théoriquement, un signal d'entrée est divisé à plusieurs reprises sans perte vers les ports de sortie. La conception de grandes matrices est assez facile car les déphaseurs peuvent être placés symétriquement par rapport à la ligne de phase et le diagramme d'une matrice de Butler est identique à celui d'une FFT (Fast Fourier Transform).

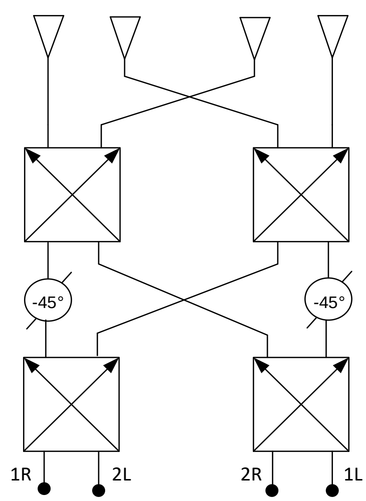

Figure 6.5 Une topologie standard de la matrice 4X 4 Butler.

Matrice de Blass

La matrice de Blass (Figure 6.6) est largement utilisée malgré sa complexité et son coût élevé en raison des coupleurs directionnels particuliers à réaliser à chaque croisement. La matrice de Blass peut être conçue avec un nombre quelconque d'éléments. Cependant, cette matrice est problématique à cause des charges terminales [22].

Matrice de Nolen

La matrice de Nolen (Figure 6.7) peut être considérée comme un cas particulier de la matrice de Blass. Où, N éléments d'une antenne sont couplés à M ports de faisceau. Ainsi, la matrice de Nolen peut alimenter un nombre d'antennes (M) différent du nombre d'orientations de faisceaux (N). Cette matrice est constituée de deux types de composants (coupleur et déphaseur) et ne montre pas de croisement [22]. Chaque nœud de la matrice est constitué d'un coupleur directionnel de paramètre θ_{ij} et d'un déphaseur de paramètre φ_{ij}. Où, l'algorithme de Mosca [MOSCA et al. (2002)] est utilisé pour calculer ces paramètres à partir de N et M et de la direction des faisceaux [24].

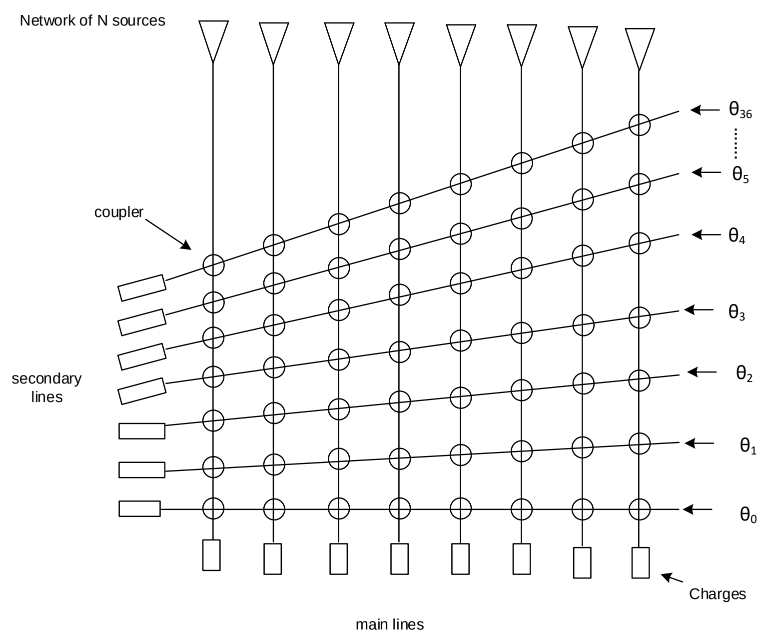

Figure 6.6 Topologie de la matrice de Blass.

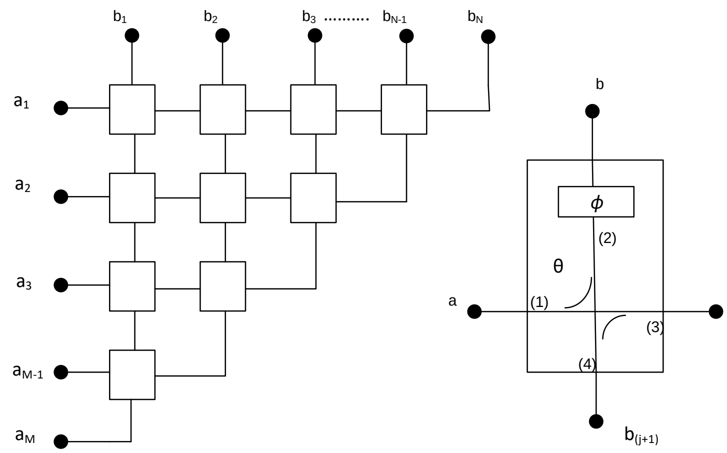

Figure 6.7 La forme générale de la matrice de Nolen.

6.2.2 Matrice de Nolen comme démodulateur

La matrice Nolen est plus adaptée pour construire une structure équivalente aux six ports avec deux entrées et quatre sorties. Contrairement à la matrice de Bulter, qui donne 4 par 4 (puisque deux ports sont inutiles dans ce cas) et à la matrice de Blass (une efficacité réduite en raison des pertes décrites précédemment dans la section Matrice de Blass).

Tableau 6-3 Paramètres de la matrice de Nolen 2X4 conservée.

	1	2	3	4
1	0.500 0^0	0.500 0^0	0.707 0^0	1.000 0^0
2	0.577 0^0	0.500 180^0	1.000 0^0	

Les paramètres théoriques des coupleurs directionnels et des déphaseurs obtenus pour la matrice décrite ci-dessus sont rapportés dans le tableau 6.3. Ces valeurs indiquent que trois coupleurs directionnels et différents déphaseurs sont nécessaires pour construire cette matrice.

La Figure 6.8 présente un schéma de simulation ADS pour la conversion directe à six ports en utilisant les composants idéaux.

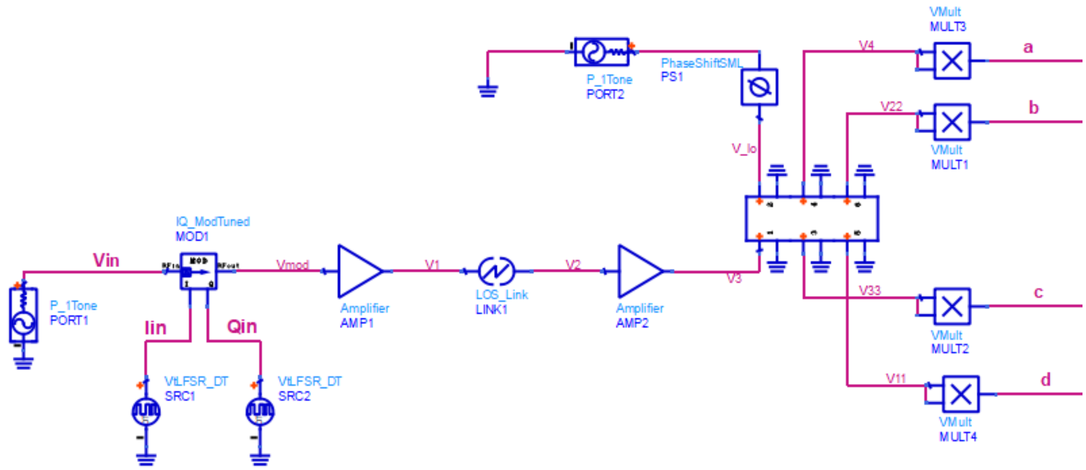

Figure 6.8 La simulation ADS de la conversion directe multiport avant l'application de la matrice Nolen.

6.2.3 *Démodulateur à six ports*

La chaîne de démodulation est mise en œuvre par le logiciel ADS d'Agilent. Le schéma général est présenté à la Figure 6.8. Le signal d'entrée modulé en QPSK passe dans un bloc contenant les paramètres de dispersion idéaux du six-port. Aux sorties du multiport, les détecteurs de puissance sont placés en utilisant le composant idéal. L'informations I/Q de la QPSK est démodulées avec un amplificateur différentiel pour la récupération en bande de base (voir Figure 6.9). Cet ensemble permet d'effectuer la soustraction des signaux et d'éliminer la composante continue indésirable.

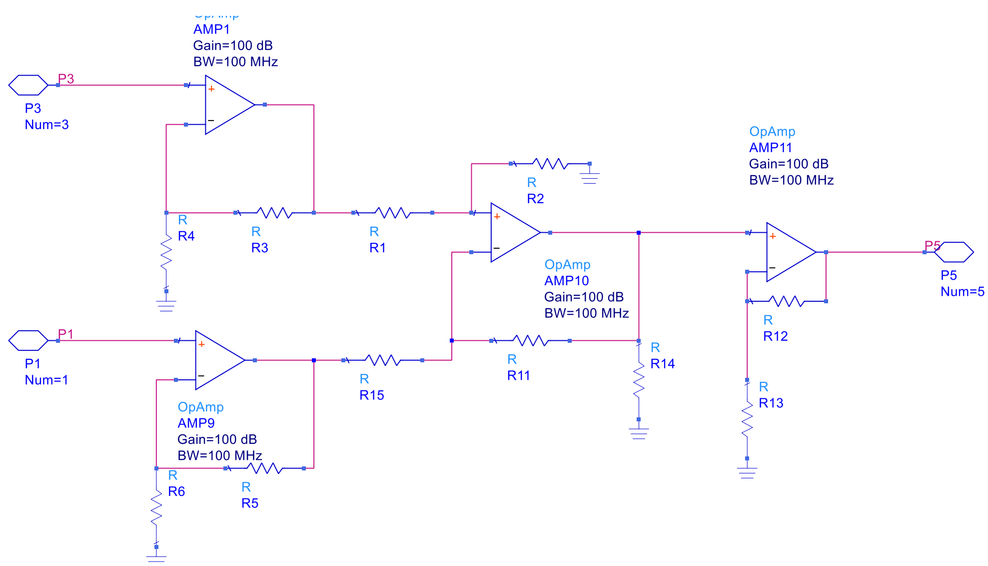

Figure 6.9 Circuit de soustraction et d'amplification utilisant des amplificateurs opérationnels.

La Figure 6.10 illustre les signaux d'entrée et de sortie dans la plage de 0 à 1 µs. Sur la même figure, il est clair que les signaux de sortie I_{out}/Q_{out} contiennent les mêmes informations que les signaux d'entrée I_{in}/Q_{in} respectivement. Il est à noter que le multi-port apporte peu de distorsion dans les signaux récupérés. Une légère variation d'amplitude de la tension peut être remarquée.

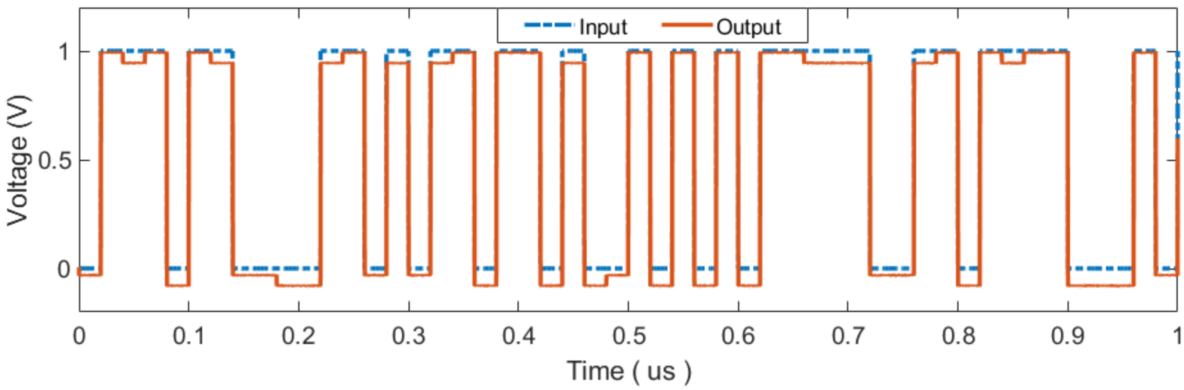

(a)

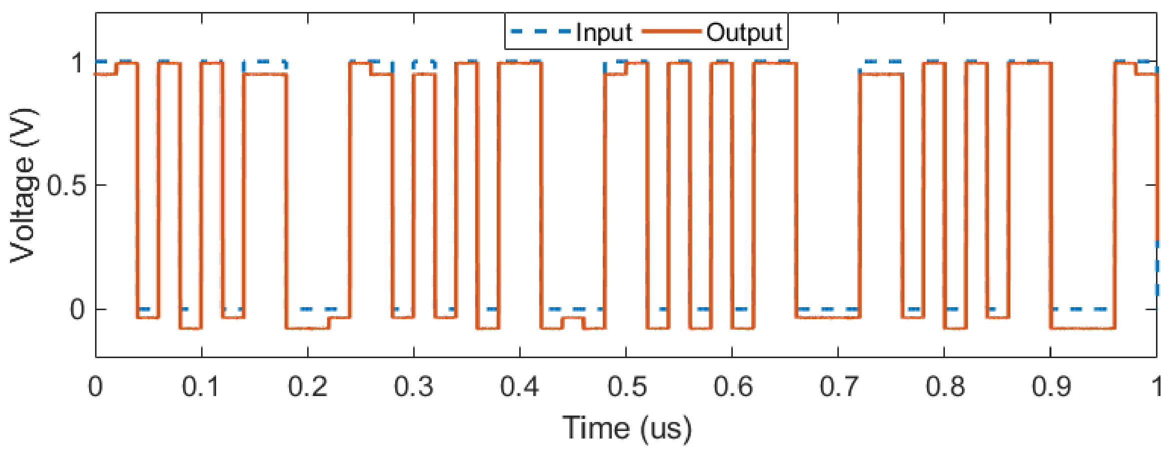

(b)

Figure 6.10 Signaux d'entrée et de sortie (a) I_{input} et I_{output} et (b) Q_{input} et Q_{output}

6.2.4 *Conception de la matrice Nolen (utilisant des composants idéaux)*

La matrice Nolen est construite avec des composants idéaux, comme le montre la Figure 6.11.

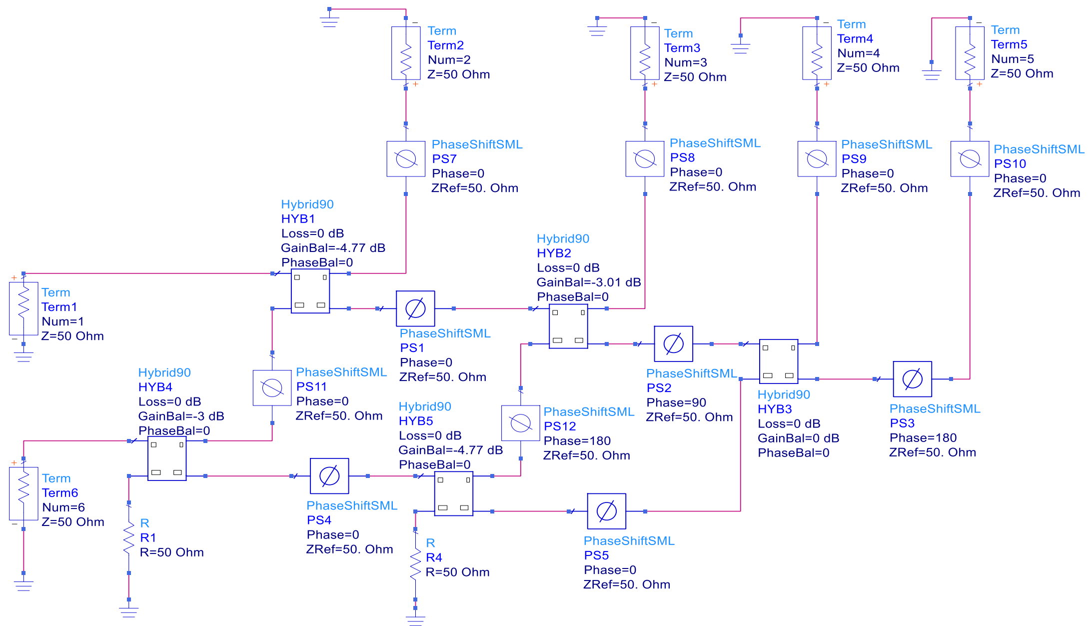

Figure 6.11 La matrice Nolen sous ADS (cas idéal)

La Figure 6.12 montre les résultats de la matrice de Nolen avec des composants idéaux. Où, cette figure illustre les différences de phase relatives simulées entre les ports de sortie adjacents pour le port 1 et les ports de sortie adjacents pour le port 6.

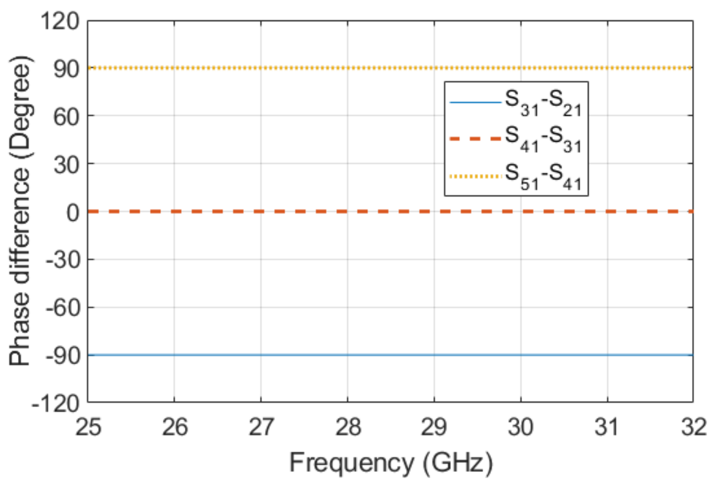

(a)

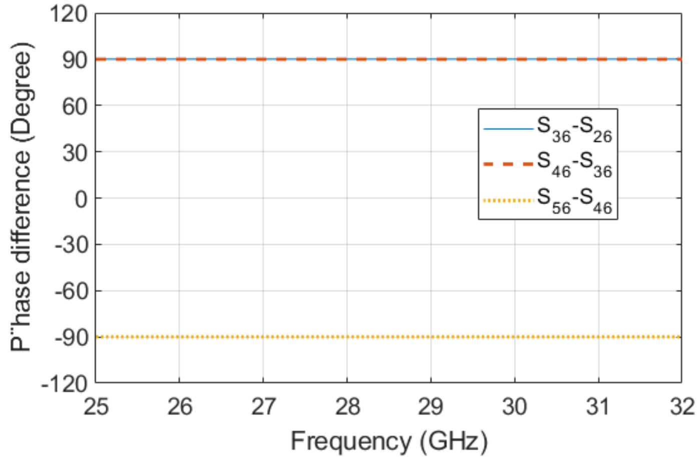

(b)

Figure 6.12 Différences de phase relatives simulées entre : (a) les ports de sortie adjacents pour le port 1 et (b) les ports de sortie adjacents pour le port 6.

6.2.5 *Six ports basés sur la matrice Nolen avec des composants idéaux*

Dans la Figure 6.13, un diagramme de la simulation ADS montrant le récepteur à conversion directe basé sur une matrice de Nolen avec des composants idéaux.

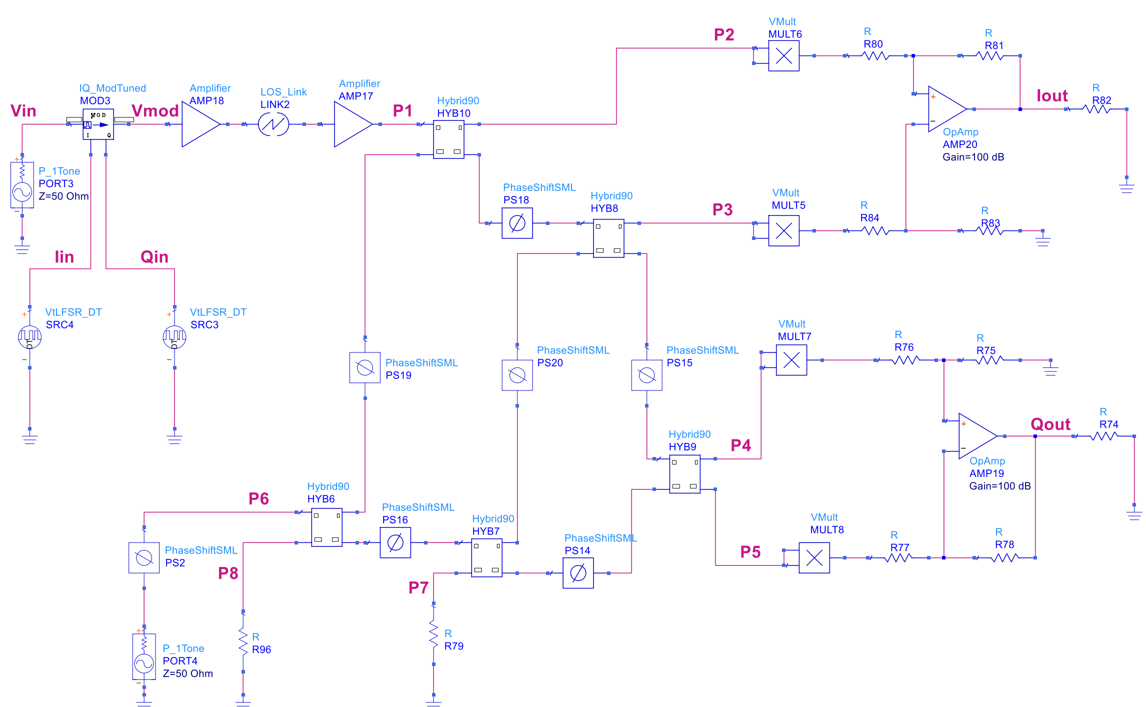

Figure 6.13 Six ports basés sur la matrice Nolen utilisant des composants idéaux.

La Figure 6.14 présente les signaux d'entrée et de sortie dans la plage de 0 à 1 µs. De la même figure, il est clair que les signaux de la modulation QPSK d'entrée I_{input}/Q_{input} sont en phase avec les signaux de sortie I_{out}/Q_{out} respectivement. Il est à noter que le multi-port apporte peu de distorsion dans les signaux récupérés. Une légère variation de l'amplitude de la tension peut être remarquée.

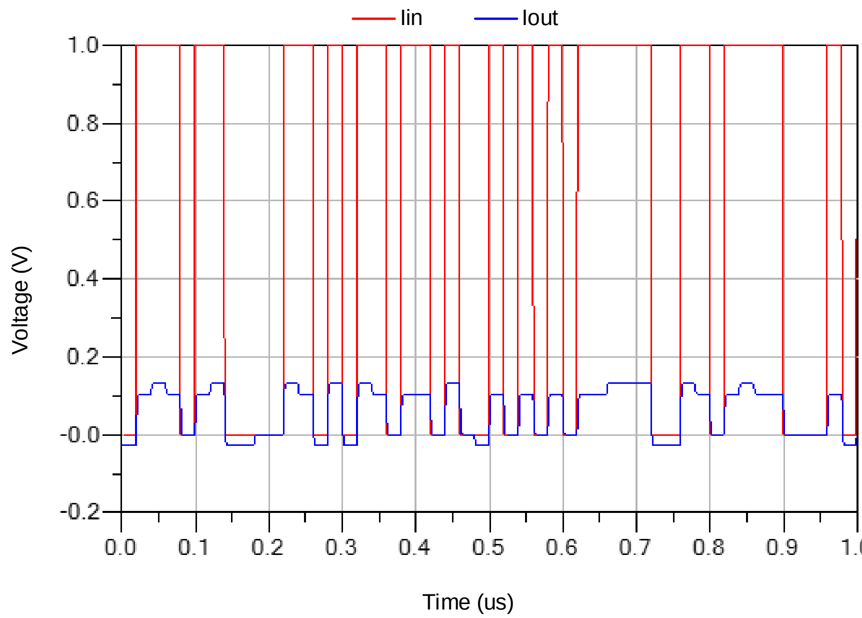

(a)

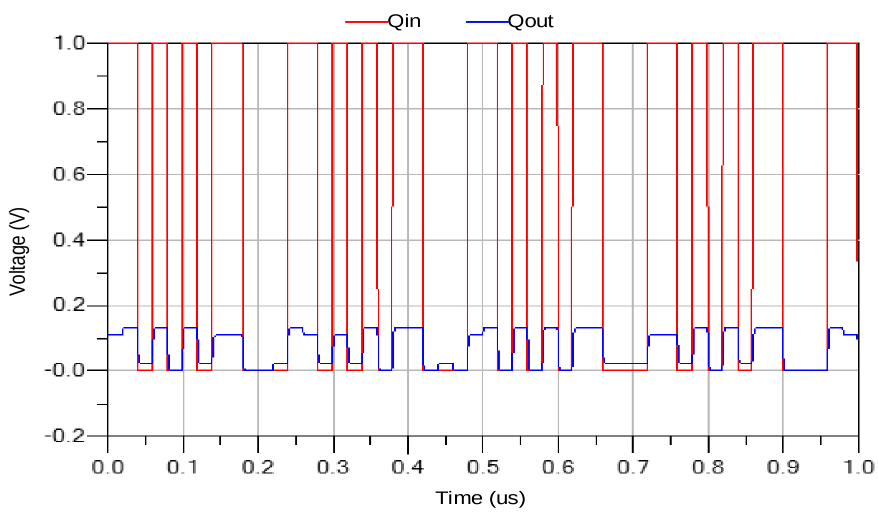

(b)

Figure 6.14 Signaux d'entrée et de sortie (a) I_{input}/I_{output} en volt en fonction du temps et (b) Q_{input}/Q_{output} en volt versus temps.

6.3 CHAPITRE TROIS : Design de la matrice de Nolen

6.3.1 Coupleur directionnel

Les coupleurs hybrides (ou Branch line) sont des dispositifs passifs largement utilisés dans les circuits et systèmes hyperfréquences et RF. Simplement, ces dispositifs couplent une partie de la puissance du signal dans la ligne de transmission au le port, ce qui permet à ce signal d'être utilisé dans un circuit différent.

Le coupleur à interaction localisée à quatre lignes de transmission est le type le plus simple de coupleur en quadrature, car le circuit est entièrement planaire. La Figure 6.15 montre un coupleur à interaction localisée à une section idéale dans lequel chaque ligne de transmission a un quart d'onde de longueur. Ces coupleurs sont très faciles à concevoir et suffisants pour certaines applications en raison de leurs performances idéales à la fréquence centrale souhaitée.

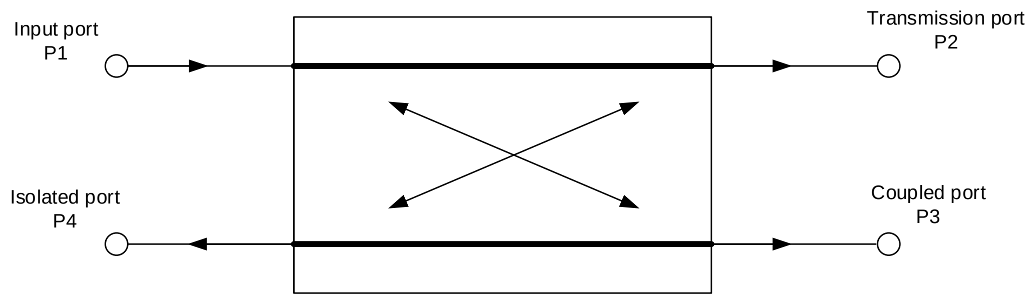

Figure 6.15 Coupleurs hybrides 3 dB à une seule section à 90 °.

6.3.2 Coupleur à interaction localisée à 7 lignes de transmission (deux sections)

Le coupleur hybride 90° présente un déphasage de 90° entre le port couplé et le port direct. Le coupleur 90° est le plus utilisé dans la conception des matrices de Butler [25]. Les paramètres S du coupleur symétrique sont donnés par [26]:

$$[\boldsymbol{S}] = \begin{vmatrix} 0 & \alpha & j\beta & 0 \\ \alpha & 0 & 0 & j\beta \\ j\beta & 0 & 0 & \alpha \\ 0 & j\beta & \alpha & 0 \end{vmatrix}$$

Où: $\alpha = \boldsymbol{S}_{12} = \boldsymbol{S}_{34}$, $\boldsymbol{S}_{13} = \beta e^{j\theta}$ and $\boldsymbol{S}_{24} = \beta e^{j\varphi}$

La configuration du coupleur hybride à section double sélectionné est illustrée à la Figure 6.16. Cette structure proposée dans [27], offre de bonnes performances en termes de bande passante et d'isolation. Le coupleur a été optimisé en modifiant principalement Z_2 et Z_3. La distribution d'impédance définit le rapport de couplage. L'utilisation de deux cellules augmente la bande passante. Les lignes des sections utilisées pour définir le coupleur constituent des lignes quart d'onde. Le déphasage de 90° est dû à la différence de longueur quart d'onde (λ/4) entre les ports de sortie. La largeur de la ligne est de 0.645 mm, ce qui correspond à une impédance de 50 ohms. Les trois coupleurs hybrides (3dB, 4.7dB et 6 dB) ont suivi la même procédure de conception.

Coupleur hybride (3dB, 90°)

La taille totale du coupleur est de (7.278 × 3.268 mm2) et le substrat utilisé est (Rogers_RT_Duroid6002) avec une permittivité de 2.93 et une épaisseur de 0.254 mm. Le coupleur a été conçu pour couvrir une large bande [25-32 GHz]. Et comme le montre les simulations présentées dans la Figure 6.16 b), le coupleur montre une excellente division, une adaptation et une isolation supérieur à 23 dB sur toute la bande.

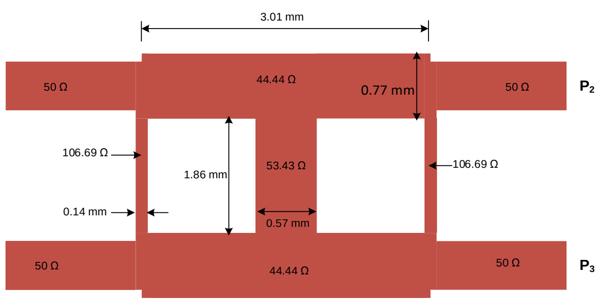

a)

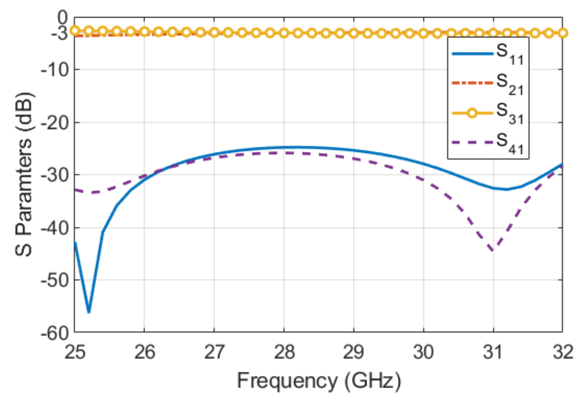

b)

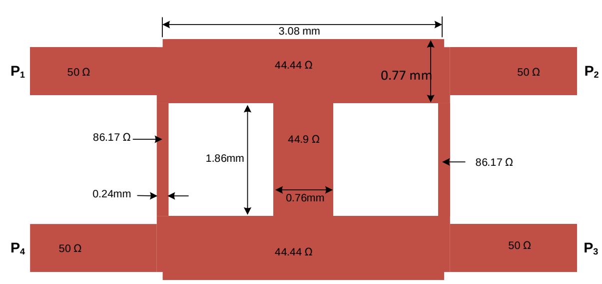

c)

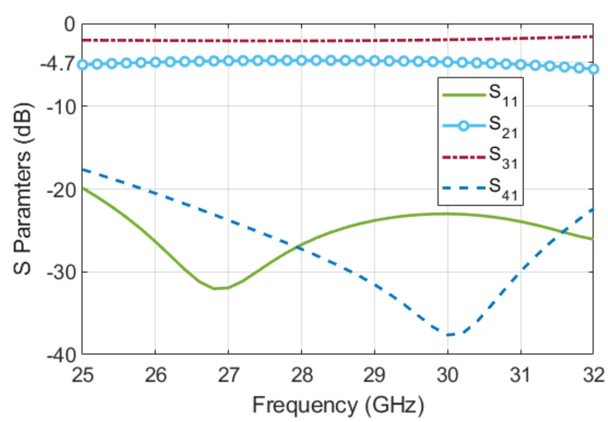

d)

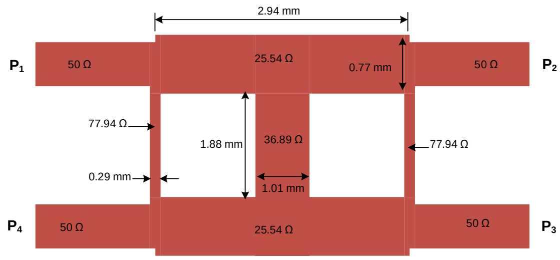

e)

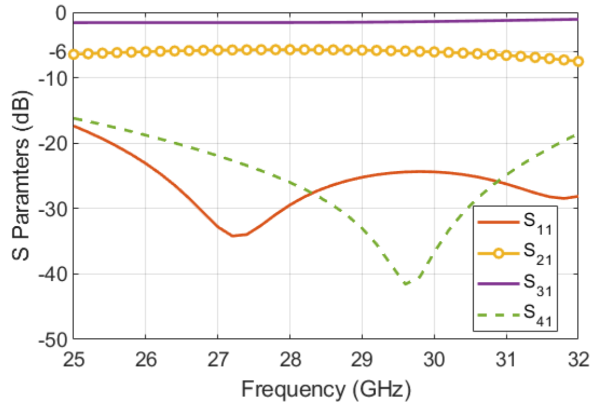

f)

Figure 6.16 Présentation du coupleur hybride montrant les détails relatifs aux dimensions en (mm) et à l'impédance en (Ohm) et résultats du paramètre S simulés : a) et b) coupleur 3 dB ; c) et d) coupleur 4.7 dB ; e) et f) coupleur 6 dB.

Coupleur hybride (4,7 dB, 90°) : La taille totale du coupleur est de 6,696 × 3,5093 mm2. La Figure 6.16 c) donne plus de détails sur les dimensions en mm ainsi que sur l'impédance des différentes sections du coupleur de 4.7 dB conçu. La Figure 6.16 d) trace les paramètres S simulés (amplitude). Les résultats montrent une isolation et adaptation de 24 dB pour une bande de 25.8 à 32 GHz avec une bonne stabilité du couplage autour 4.7dB.

Coupleur hybride (6 dB, 90°) : la taille globale du coupleur est (6,74926 × 3,438 mm2). La structure du coupleur hybride, illustrée à a la Figure 6.16 e), fournit plus de détails sur les dimensions en mm ainsi que sur l'impédance du coupleur de 6 dB conçu. La Figure 6.16 d) montre les paramètres S simulés. Une adaptation et une isolation plus que 24 dB sont observées pour les fréquences comprises entre 26.5 GHz et 32 GHz. De plus, le coefficient de transmission est de 6 dB au port 2 (S_{21}) et d'environ 2 dB pour port 3 (S_{31}).

6.3.3 Déphaseur

La technique proposée utilise la forme en T, qui est différente des conceptions conventionnelles. Étant donné que cette méthode vise principalement à réduire la taille, elle peut être utile pour de nombreuses applications lorsque la limitation de la surface est un problème, en particulier lorsque vous travaillez dans des bandes d'ondes en mm où les circuits sont très petits.

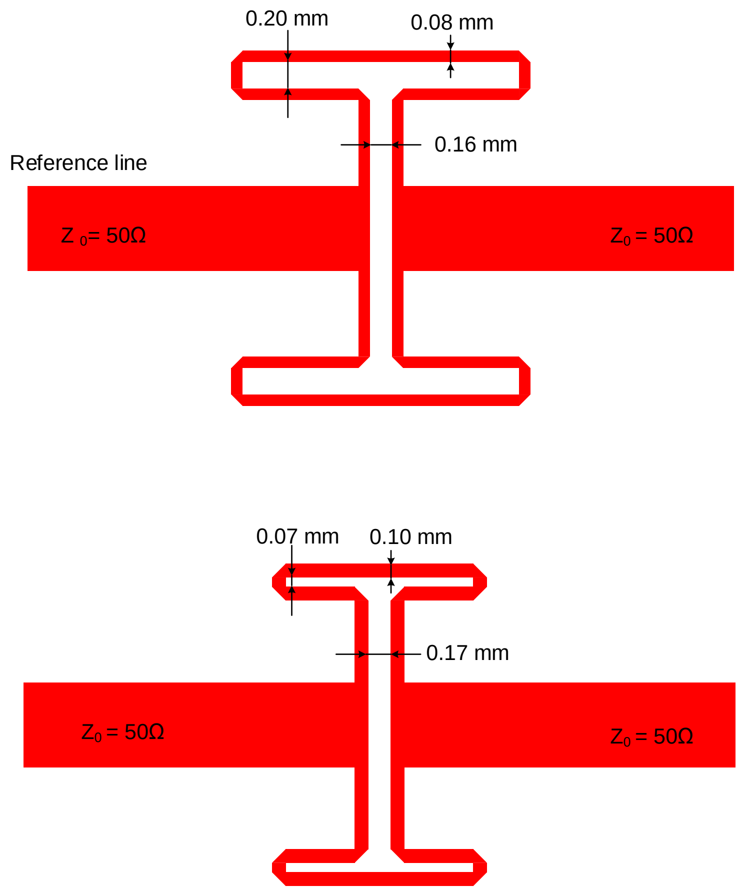

Figure 6.17 La disposition du déphaseur proposé en double forme de T à 90 ° en tenant compte de la symétrie de chaque élément.

Il est à noter que les formes T supérieure et inférieure sont symétriques pour chaque élément du déphaseur (voir Figure 6.17). Les dimensions de l'élément de phase de forme T du haut correspondent à la largeur des lignes couplées optimisées à 0.08 mm pour l'ensemble de l'élément. Pour l'élément inférieur, la largeur des lignes couplées est de 0.10 mm pour l'ensemble de l'élément et les gaps des lignes couplées à 0.07 mm dans le plan horizontal et à 0.17 mm dans le plan vertical (en considérant la symétrie de chaque élément).

Les Figures 6.18 montrent un bon niveau de déphasage (90° ± 2°) autour de la fréquence souhaitée (28 GHz). Ces résultats significatifs sont observés sur une bande passante (7,75 GHz) de 26,25 GHz à 34 GHz. De plus, les résultats en termes de coefficient de réflexion sont acceptables (S11≈ -13 dB) pour toute la largeur de bande.

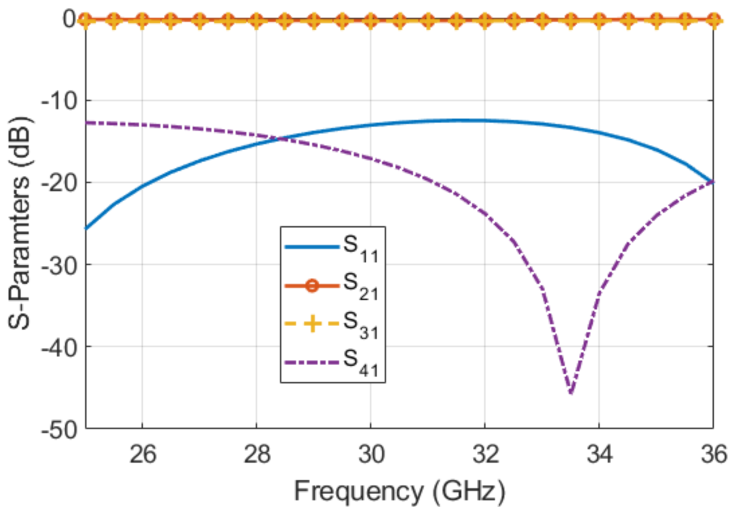

(a)

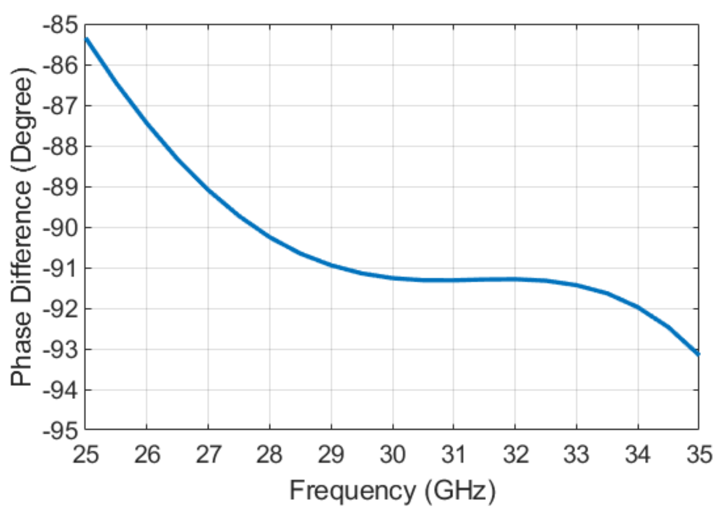

(b)

Figure 6.18 Résultats simulés du déphaseur 90^0 à double phase proposé. (a) Réponse en amplitude. (b) Réponse en phase.

6.3.4 Matrice Nolen conçue à l'aide de l'ADS

La matrice Nolen basée sur une topologie de réseau conventionnelle est conçue à une fréquence centrale de 28 GHz avec une bande passante d'au moins 3 GHz. Une étape d'optimisation a été effectuée. Comme prévu en théorie, un délai supplémentaire à cause des coupleurs peut être augmenté la dispersion. La solution proposée est une matrice de Nolen où les différents chemins doivent être autant que possible égaux pour augmenter la bande passante. Une architecture presque parallèle est utilisée dans cette matrice. La compensation du retard généré par les coupleurs assurera le comportement à large bande. Les performances de cette matrice sont comparables à celles de la matrice de Butler, avec la possibilité de concevoir des matrices avec n'importe quelle combinaison *NxM*.

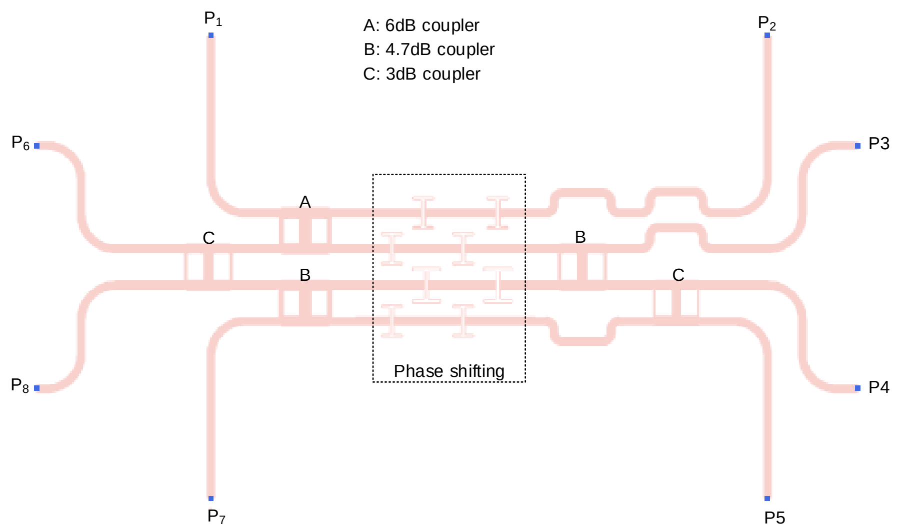

Figure 6.19 Présentation du démodulateur basé sur la matrice Nolen.

La Figure 6.19 montre la disposition simulée de Momentum (ADS). Des lignes de transmission égales sont ajoutées à la conception initiale pour différencier l'accès à l'entrée ainsi que la sortie pour faciliter la caractérisation.

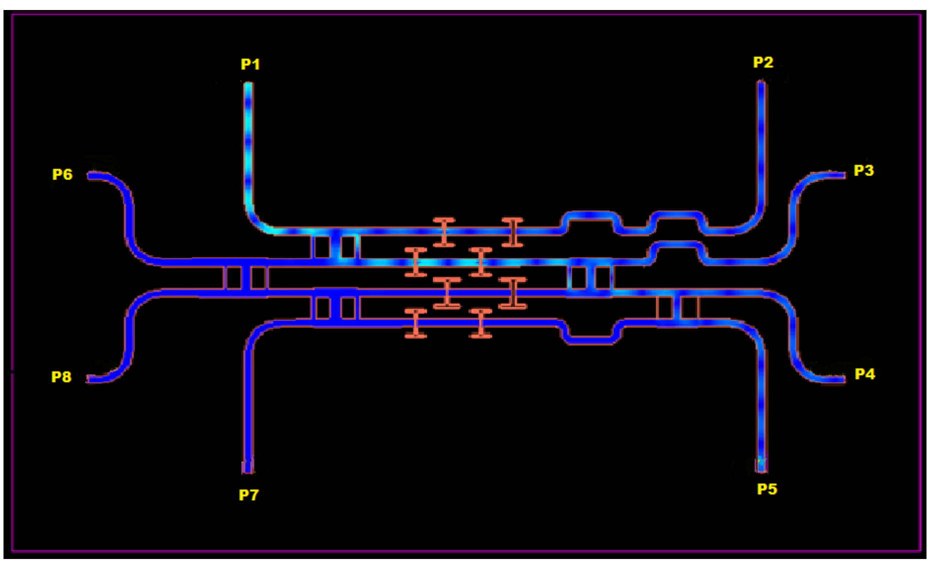

(a)

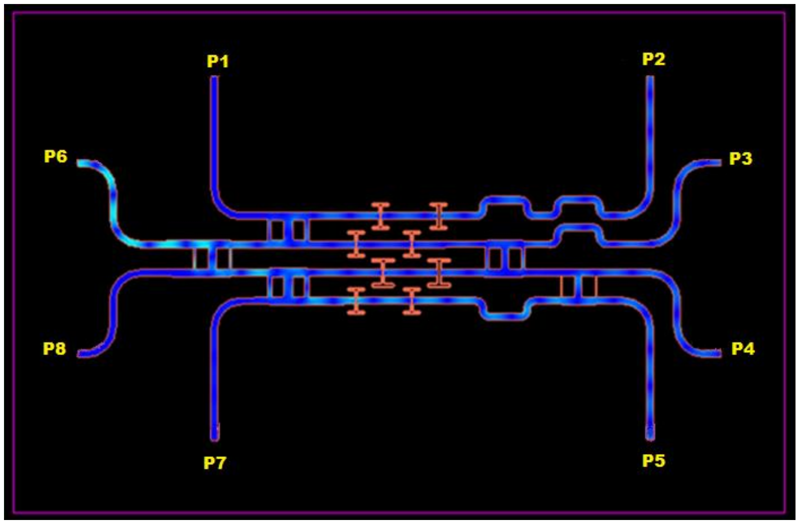

(b)

Figure 6.20 La distribution du champ électrique (a) lorsque le port 1 est excité (b) lorsque le port 6 est excité

La Figure 6.20 montre la répartition de l'énergie et l'isolation lorsque l'excitation est appliquée aux deux ports d'entrée P1 et P6 à la fois. D'abord, lorsque le port 1 (P1) est excité pour montrer la répartition de l'énergie dans les quatre ports de sortie (P2, P3, P4 et P5), l'autre port d'entrée P6 étant isolé et les deux ports inutilisés P7 et P8 l'étant également. La dernière étape a été répétée pour l’autre port d’entrée P6 afin de montrer la répartition de l’énergie dans les quatre ports de sortie (P2, P3, P4 et P5), l’autre port d’entrée P1 étant isolé et les deux ports inutilisés P7 et P8 étant isolés. Une bonne isolation peut être remarquée et une distribution normale comme prévu lors de l'application de cette technique.

6.4 Validation expérimentale

6.4.1 Circuit fabriqué

Un circuit multiport basé sur la matrice de Nolen a été fabriqué sur un substrat de laminés Rogers RT/duroid 6002. Il a une permittivité diélectrique de 2,94 avec une épaisseur de substrat de 10 mil. Les dimensions du circuit fabriqué sont 62 mm (en longueur), 35 mm (en largeur) et 0,254 mm (en hauteur). Le prototype du multiport fabriqué à partir de la matrice de Nolen est présenté à la Figure 6.21.

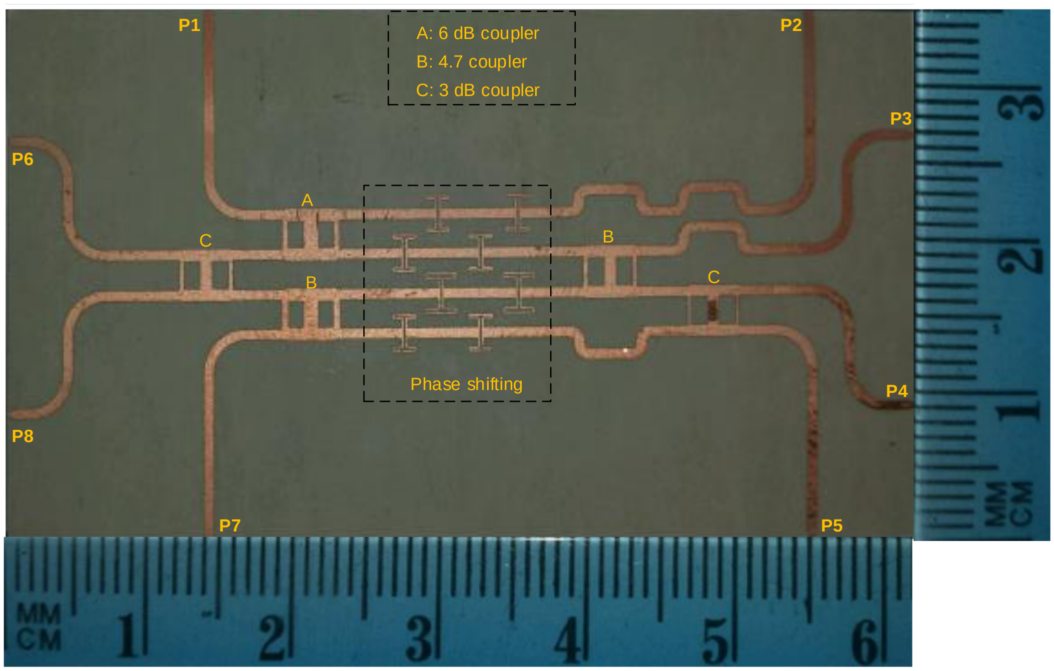

Figure 6.21 Photographie du circuit fabriqué.

6.4.2 *Résultats*

Les ports 1 et 6 sont les accès pour les signaux RF et LO respectivement. Les ports 2 à 5 sont les ports de sortie qui seront connectés aux détecteurs de puissance. Les deux ports inutilisés (7 et 8) doivent être connectés à des charges. La mesure des paramètres S est importante pour caractériser les performances du dispositif tel que l'isolation des ports RF-LO (S_{65}), l'adaptation aux ports d'entrée, la puissance transmise des ports RF et LO aux ports de sortie ainsi que la différence de phase entre les signaux transmis.

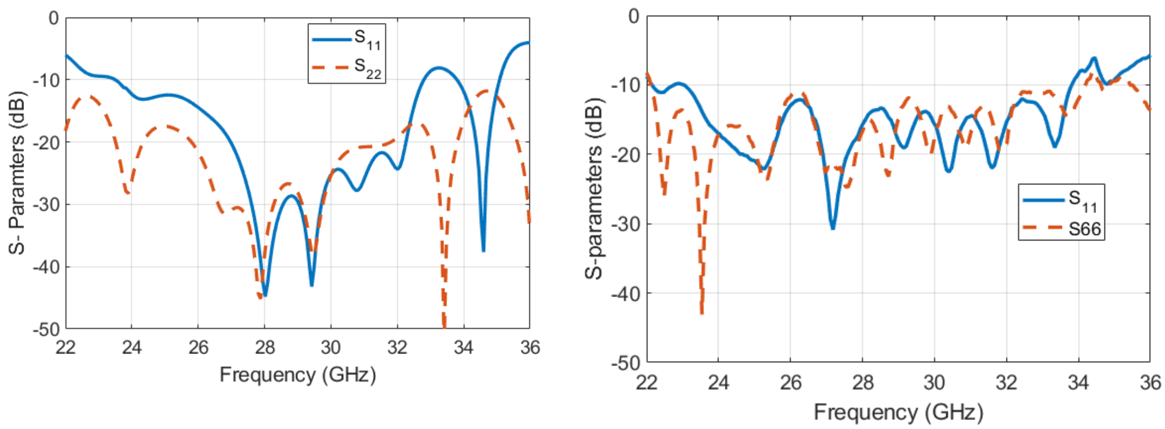

a) b)

Figure 6.22 Adaptation des entrées: a) simulée, b) mesurée

Les pertes de retour simulées et mesurées aux ports d’entrée (port 1 : entrée RF et port 6 : entrée LO) sont illustrées à la Figure 6.22 (a et b). Dans la bande (27 - 32 GHz), toutes les valeurs sont meilleures que 20 dB. Ces résultats atteignent 27 dB dans la bande de fréquences (27.5 – 29.8 GHz). Les valeurs mesurées sont supérieures à 10 dB sur toute la bande de fréquence souhaitée.

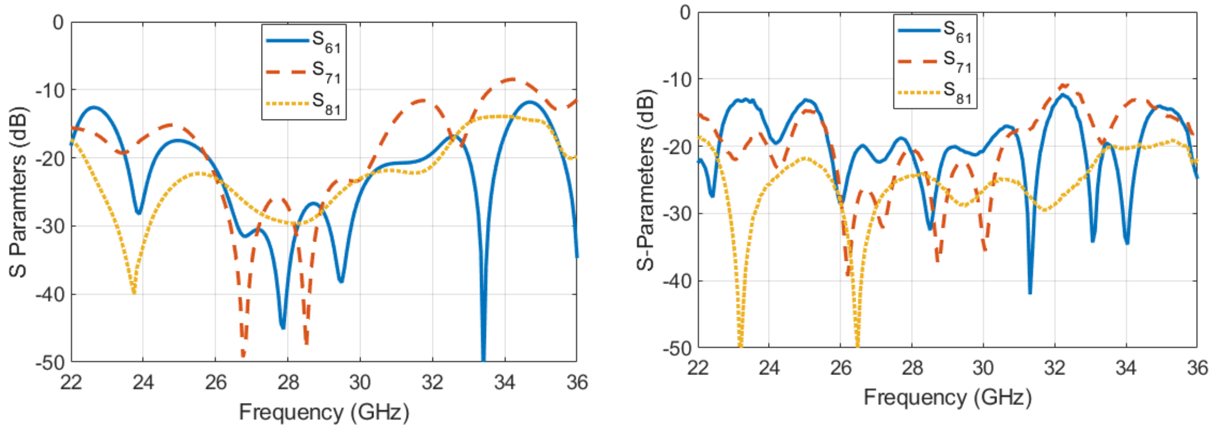

a) b)

Figure 6.23 Paramètre S d’isolation des entrées: a) simulée, b) mesurée

La Figure 6.23 montre l'isolation mesurée et simulée entre les ports d'entrée (S_{61}) ainsi que l'isolation entre le port d'entrée 1 et les deux ports inutilisés (P7 & P8), conformément à la numérotation des ports spécifiée. D'après la figure précédente, il est clair que toutes les valeurs d'isolation sont excellentes, sont supérieures à 20 dB pour sur toute la bande de fréquences (26 - 30,4 GHz). Alors que les valeurs d'isolation pour les deux ports d'entrée (S_{61}) sont de 20 dB de 26 GHz à 31,5 GHz. Les résultats mesuré et simulé sont en bon accord.

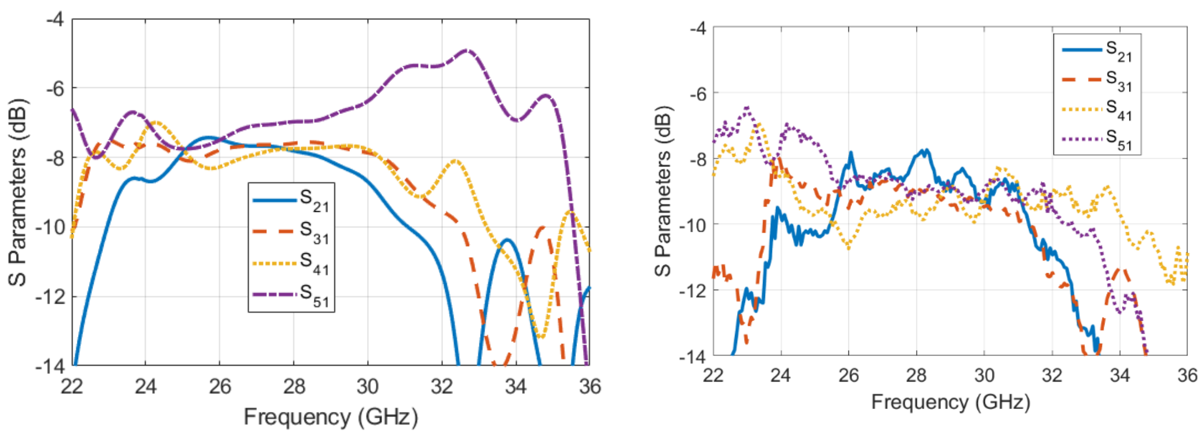

a) b)

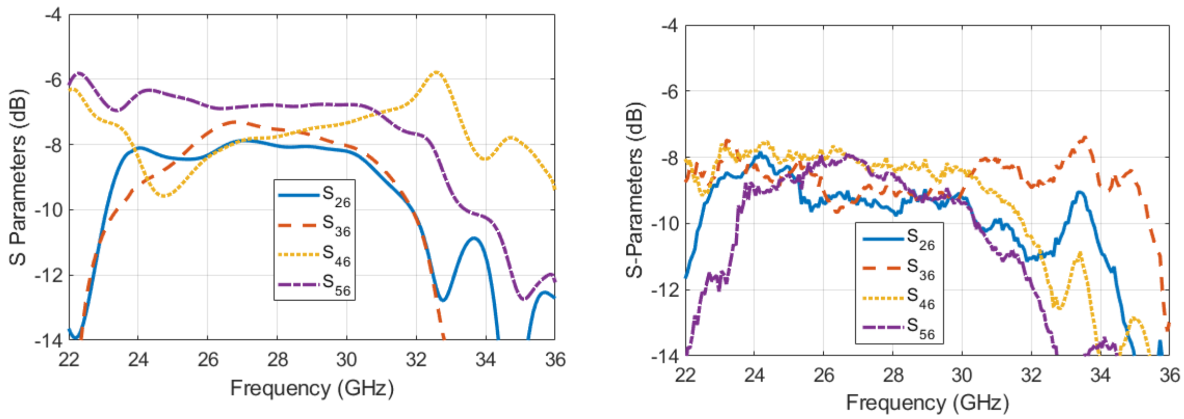

c) d)

Figure 6.24 Coefficient de transmission (amplitude): a) Port 1 simulé, b) Port 1 mesuré, c) Port 2 simulé, d) Port 2 mesuré.

La Figure 6.24 montre la répartition de puissance entre le port LO/RF et les quatre ports de sortie adjacents, S_{2X}, S_{3X}, S_{4X} et S_{5X} (où X : 1 pour le port 1 ou 6 pour le port 6). Par rapport à la valeur théorique de -6 dB, de très bons résultats sont obtenus sur la bande. Les résultats montrent moins de 1.5 dB d'affaiblissement d'insertion supplémentaire. Les pertes métalliques et diélectriques sont prises en compte dans cette simulation. Le déséquilibre d'amplitude est proche de ± 1 dB, de 24 à 30 GHz. De résultats comparables ont été obtenus sur la bande de fréquence considérée avec une dégradation probablement causé pas les connecteurs.

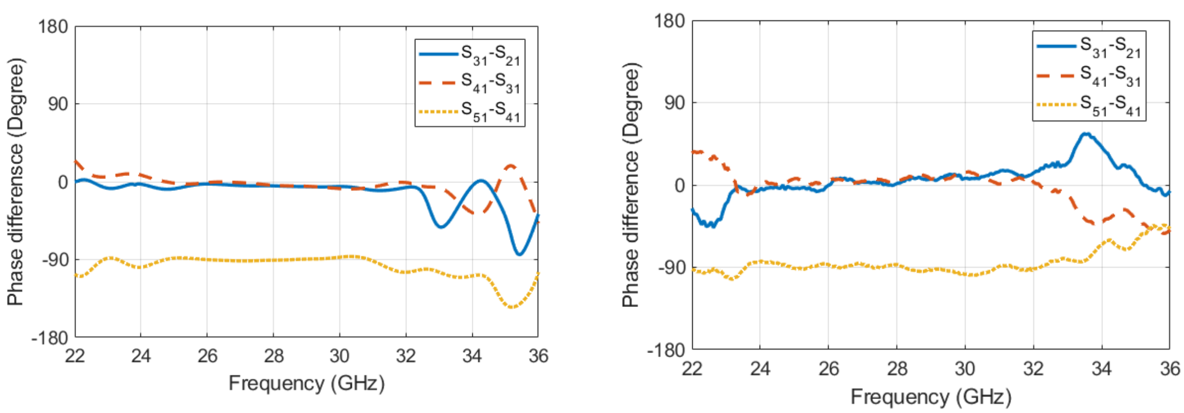

a) b)

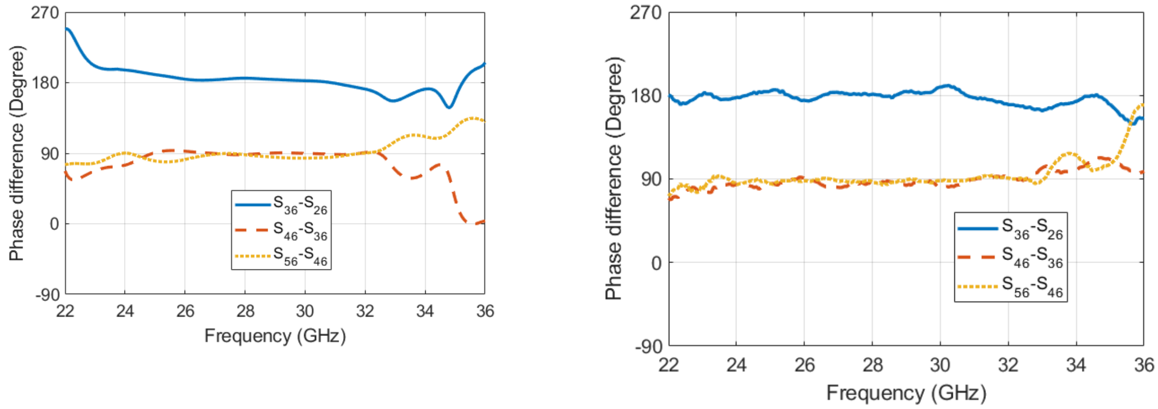

c) d)

Figure 6.25 Coefficient de transmission (phase): a) Port 1 simulé, b) Port 1 mesuré, c) Port 2 simulé, d) Port 2 mesuré.

La Figure 6.25 montre la différence de phase entre les coefficients de transmission pour les deux ports adjacents. On peut constater que la différence de phase simulée/mesurée entre chaque deux ports de sorties est proche de la référence quadratique de 90°. L'erreur de déphasage observée est inférieure à ± 2° jusqu'à 28 GHz. Les différences de phase de 0°, 0° et -90° (lorsque port 1 est considéré comme entrée) sont observés contrairement à la solution idéale proposée à la Figure 2.10. La différence de phase de 180°, 90° et 90° respectivement (lorsque port 6 est considéré comme entrée) contrairement à l’idéal proposé Figure 2.10. Ces permutations n'affectent pas les performances du multiport en tant que démodulateur. L’idée d’un démodulateur à multiport est d’avoir quatre combinaisons différentes du signal LO et RF. Les coupleurs utilisés sont -90° au lieu de +90° utilisés dans la conception du bloc.

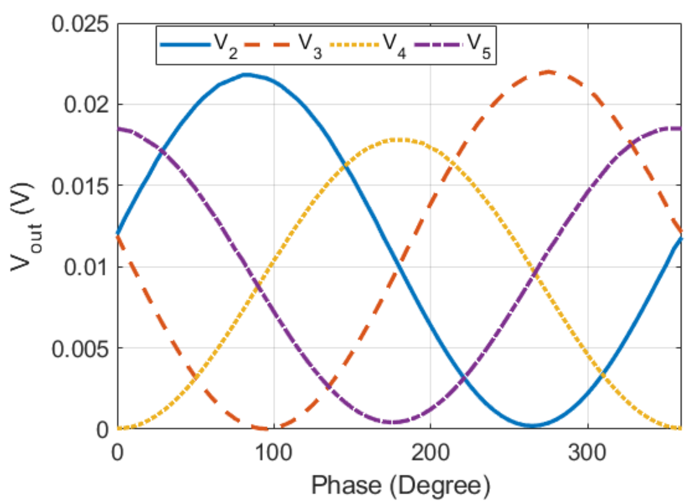

Figure 6.26 Matrice de Nolen mesurée comme discriminateur de phase.

Une phase comprise entre -10° et -2°, -8° et -1° et -90° et -86° est atteinte au port de sortie lorsque le port 1 est alimenté entre 26 et 30 GHz. Une phase entre 181° et 184°, 88° et 93° et 81° et 89° est observée au port de sortie lorsque le port 6 est alimenté.

Les résultats de mesure ont été incorporés dans la simulation de démodulateur sur ADS. La technique multiport est basée sur la discrimination de phase. Dans cette simulation les signaux RF et LO sont à la même fréquence et seule la phase du LO est modifiée sur 360°. Les voltages de sortie sont observés. Figure 6.26 montre que les deux signaux sont opposés (V_2 contre V_3 et V_4 contre V_5) et que tous les signaux sont centrés à 0 avec presque 90° de décalage l'un par rapport à l'autre. En outre. Par conséquent, les signaux I/Q pourraient être obtenus en utilisant cette technique.

6.4.3 Constellation

Les constellations de signaux démodulés sont illustrées à la Figure 6.27. Les modulations PBSK, QPSK et 8PSK sont considérées dans un cas idéal et **réaliste** (les paramètres S mesurés sont considérés). Les nuages sont très centrés monteront d’excellent démodulation. La rotation observée pour les signaux BPSK est causé par le délai du trajet. Ce délai peut être compensé, cette correction apportée aux deux autres modulations montre que le bruit de phase et amplitude propre au démodulateur à base de Nolen est très faible.

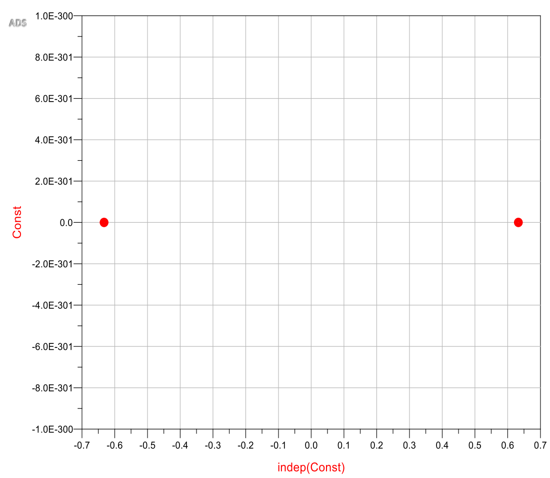

BPSK (cas idéal)

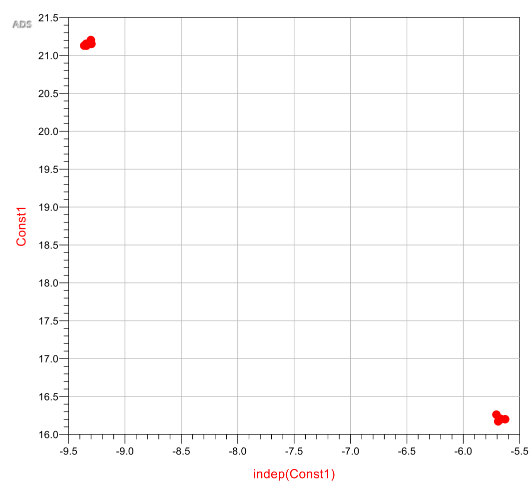

BPSK (cas réaliste)

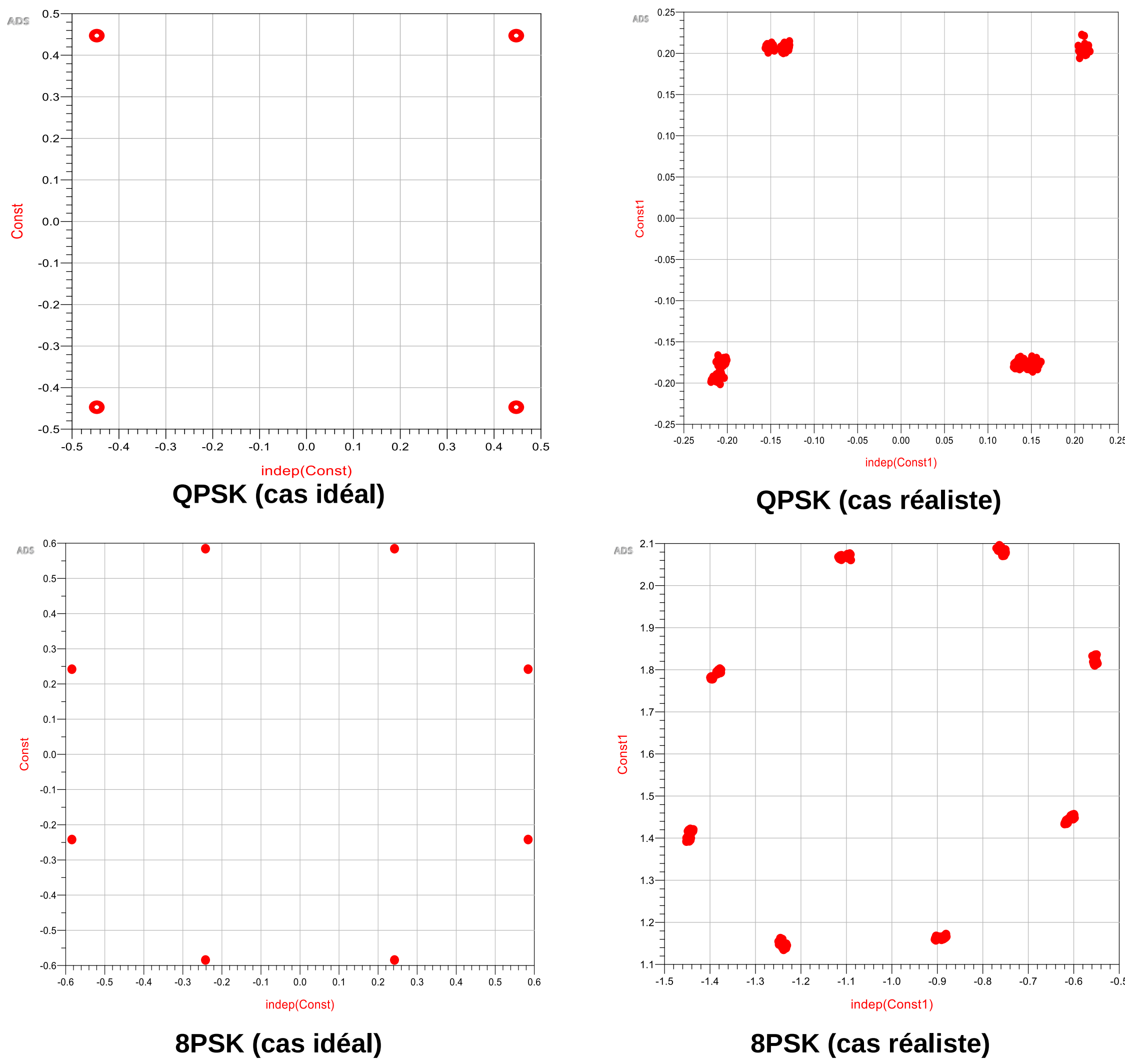

Figure 6.27 Constellations simulées du signal démodulé en considérant les paramètres S idéaux et mesurés de la matrice de Nolen proposée (BPSK, QPSK et 8PSK). Un débit de données de 40 MHz est considéré avec une distance de 150 m entre l'émetteur et le récepteur avec canal à espace libre.

6.4.4 Contributions et travaux futurs

Le travail présenté dans ce mémoire porte sur la conception et la caractérisation expérimentale de systèmes multiports basés sur la technologie de matrice Nolen (démodulateur) pour la future génération des systèmes de télécommunication sans fil (5G). Pour la première fois une matrice de formation de faisceau est utilisée comme un multiport réflectomètre pour la démodulation.

Les résultats des paramètres S mesurés ont montré que le modèle multiport proposé fonctionnait bien à 28 GHz. Une bonne adaptation pour tous les ports avec des résultats meilleurs que 20 dB. L'isolation entre les ports RF et LO (respectivement 1 et 6) est d'au moins 20 dB. Les magnitudes des coefficients de transmission S_{21} à S_{51} et S_{26} à S_{56} sont respectivement proches de -8 dB et de -7.5 dB. Les phases des coefficients de transmission correspondent aux valeurs théoriques. Ces performances ont été intégré à une simulation du multiport comme discriminateur de phase et par la suite testé avec plusieurs types de modulations. Les résultats obtenus confirment l'approche de conception du multiport pour les futurs récepteurs de communication sans fil haut débit.

Travaux futurs

Aujourd'hui, la technologie de communication mm Wave dans la bande de fréquence 28 GHz est en pleine croissance et devrait jouer un rôle central dans le système de communication à technologie de prochaine génération. Travailler dans ce cadre serait donc un pas en avant vers les exigences de la 5G.

La réalisation d’une plateforme de mesure avec démodulateur (générateur de signal/modulateur) via un câble coaxial et/ou une antenne pour la modulation est impérative pour étudier les performances du système. Pour cela, un détecteur de puissance doit être conçu, simulé et validé pour constituer le système de réception. La réalisation de système émetteur-récepteur est envisagée.

References

[1] J. Nightingale, P. Salva-Garcia, J. M. A. Calero and Q. Wang, "5G-QoE: QoE Modelling for Ultra-HD Video Streaming in 5G Networks," in IEEE Transactions on Broadcasting, vol. 64, no. 2, pp. 621-634, June 2018.

[2] K. L. A. Yau, J. Qadir, C. Wu, M. A. Imran and M. H. Ling, "Cognition-Inspired 5G Cellular Networks: A Review and the Road Ahead," in IEEE Access, vol. 6, pp. 35072-35090, 2018.

[3] T. Kawanishi, A. Kanno and H. S. C. Freire, "Wired and Wireless Links to Bridge Networks: Seamlessly Connecting Radio and Optical Technologies for 5G Networks," in IEEE Microwave Magazine, vol. 19, no. 3, pp. 102-111, May 2018.

[4] J. Mundy, "What Is Massive MIMO Technology?" 5G. Co. uk - UK's Premier 5G Resource, 2018, 5g.co.uk/guides/what-is-massive-mimo-technology/.

[5] Innovation, Science and Economic Development Canada, "Consultation on Releasing Millimetre Wave Spectrum to Support 5G," Ottawa; 2017. 31 p.

[6] Federal Communications Commission, "Report and Order and Further Notice of Proposed Rulemaking," Retrieved from https://www.fcc.gov/news-events/events/2016/03/spectrum-frontiers-workshop. 2016.

[7] International Telecommunication Union, "Overview of ITU-T activities on 5G/IMT-2020," Retrieved from https://www.itu.int/en/ITU-T/Workshops-and-Seminars/201707/Pages/default.aspx. 2017

[8] A. A. Zaidi et al, "Waveform and Numerology to Support 5G Services and Requirements," in IEEE Communications Magazine, vol. 54, no. 11, pp. 90-98, November 2016.

[9] J. Östh, "Study of Six-Port Modulators and Demodulators for High-Speed Data Communications" Master's Thesis, Linköping University, 2012.

[10] C. Hannachi, "Conception De Nouveaux Composants En Technologie Hybride Pour Les Communications A Haut Débit En Bande Millimétrique," Mémoire ou thèse présentée pour l'obtention du grade de Philosophiae doctor (PhD.), Université du Québec Institut National de la Recherche Scientifique Centre Énergie Matériaux Télécommunications, 2017.

[11] S. B. Cohn and N. P. Weinhouse, “An Automatic Microwave Phase Measurement System,” Microwave J., vol. 7, no. 2, pp. 49–56, Feb. 1964.

[12] G. F. Engen, “The Six-Port Reflectometer: An Alternative Network Analyzer,” IEEE Trans. Microwave Theory Tech., vol. MTT-25, no. 12, p. 1075-1080, Dec. 1977.

[13] C. A. Hoer, “A Network Analyzer Incorporating Two Six-Port Reflectometers,” IEEE Trans. Microwave Theory Tech., vol. MTT-25, no. 12, p. 1070-1074, Dec. 1977.

[14] H.M. Cronson and L. Susman, “A Dual Six-Port Automatic Network Analyzer,” IEEE Trans. Microwave Theory and Tech., vol. MTT-29, no. 4, pp. 372-378, Avr. 1981

[15] S. 0. Tatu, E. Moldovan, Ke Wu and R. G. Bosisio, "A New Direct Millimeter Wave Six-Port Receiver, " Microwave Symposium Digest, 2001 IEEE MTT-S International, Vol. 3, pp. 1809-1812, May 2001.

[16] O. Kramer, "Design and Realization of A Network Composite Receiver of Vertical Multilayer Yagi Antennas and Microwave Components" Master's Thesis, Ecole Polytechnique De Montréal, 2010.

[17] K. Wu, "Multiport Interferometer Techniques for Innovative Transceiver Applications," 2010 IEEE Radio and Wireless Symposium (RWS), New Orleans, LA, 2010, pp. 531-534.

[18] S. O. Tatu and T. A. Denidni, "New Millimeter-Wave Six-Port Heterodyne Receiver Architecture," 2006 IEEE MTT-S International Microwave Symposium Digest, San Francisco, CA, 2006, pp. 1999-2002.

[19] S. O. Tatu and T. A. Denidni, "Analysis Of A New Multiband Multiport Circuit For Phase Detection Applications," in IEEE Microwave and Wireless Components Letters, vol. 15, no. 6, pp. 389-391, June 2005.

[20] S. O. Tatu and T. A. Denidni, " Multiband Multiport Direct Conversion Receiver: Design, Implementation, And Demodulation Results" in IEEE Microwave and Optical Technology Letters, vol. 48, No. 4, April 2006.

[21] J.G. Fonseca, “Discussion On Reciprocity, Unitary Matrix, And Lossless Multiple Beam Forming Networks,” International Journal of Antennas and Propagation (2015).

[22] C. Roeloffzen et al., "Enhanced Coverage Though Optical Beamforming In Fiber Wireless Networks," 2017 19th International Conference on Transparent Optical Networks (ICTON), Girona, 2017, pp. 1-4.

[23] T. Djerafi, " Etude Et Réalisation De Matrices A Commutation De Faisceaux En Technologie Guide D'ondes Integré Au Substrat" PhD. thesis, École Polytechnique De Montréal, .2011., Ecole Polytechnique De Montréal, 2011.

[24] S. Zheng, W. S. Chan, S. H. Leung, and Q. Xue, "Broad Band Butler Matrix With Flat Coupling, " Electron. Lett., vol. 43, no. 10, pp. 576–577, May 2007.

[25] J. BLASS, "Blass Matrix for Shaped Beam Conformal Antenna," Conference on aerospace antennas, IEE, London, UK.1971, pp. 280.

[26] J. BLASS, "Multi-Directional Antenna – New Approach Top Stacked Beams,". ire international convention record, PT. 1,1960, PP. 48-50.

[27] S. Mosca, F. Bilotti, A. Toscano and L. Vegni, "A Novel Design Method For Blass Matrix Beam-Forming Networks," in IEEE Transactions on Antennas and Propagation, vol. 50, no. 2, pp. 225-232, Feb. 2002.

[28] D. M. Pozar, "Microwave Engineering 2nd Edition," New York: John Wiley & Sons,Inc. 716p, 1998.

[29] S. Zheng, W. S. Chan, S.H. Leung and Q. Xue, "Broadband Butler Matrix With Flat Coupling," Electronics Letters 10 th May 2007 Vol.43 No.10.

[30] B. M. Schiffman, "A New Class of Broad-Band Microwave 90-Degree Phase Shifters," IEEE Transactions on Microwave Theory and Techniques, vol. 6, no. 4, pp. 232-237, Apr. 1958.

[31] A.P., Gorbachev, V.S., Churkin, and A.A., Vasilenko, "The Modified Schiffman Phase Shifter", 2010 10th International Scientific-Technical Conference on Actual Problems of Electronic Instrument Engineering, 22-24 Sept 2010, pp.124-126.

[32] Y.-X. Guo, Z.-Y. Zhang, and L. C. Ong, "Improved Wide-Band Schiffman Phase Shifter," IEEE Transactions on Microwave Theory and Techniques, vol. 54, no. 3, pp. 1196-1200, Mar. 2006.

[33] J.L.R. Quirarte, and J.P., Starski, “Novel Schiffman Phase Shifters”, IEEE Transactions on Microwave Theory and Techniques, Jan 1993, pp.9-14